2013

Small-Scale Fracture Toughness Studies of Grain Boundary Embrittlement in Cu-Bi Alloys

Mark Joseph McLean
Lehigh University

SMALL-SCALE FRACTURE TOUGHNESS STUDIES OF GRAIN BOUNDARY EMBRITTLEMENT IN CU-BI ALLOYS

by

Mark J. McLean

Presented to the Graduate and Research Committee

of Lehigh University

in Candidacy for the Degree of

Doctor of Philosophy

in

Materials Science and Engineering

Lehigh University

September 2013

Approved and recommended for acceptance as a dissertation in partial fulfillment of the requirements for the degree of Doctor of Philosophy.

_____

Date

_____

Dissertation Director

_____

Accepted Date

Committee Members:

_____

Prof. Richard P. Vinci, Committee Chair

_____

Prof. Masashi Watanabe, Committee Member

_____

Prof. Herman F. Nied, Committee Member

_____

Prof. Anand Jagota, Committee Member

ACKNOWLEDGEMENTS

First and foremost, I would like to thank Dr. Rick Vinci for not only giving me the opportunity to work for him as a grad student, but also for everything he did to help me as an advisor and a mentor during that time. None of my accomplishments (past, present, and future) would be possible without your contributions to my education. Next, I would like to thank the staff at Lehigh for all the help they have provided me over the years. This includes Dave Ackland, Bill Mushock, and Rob Keyse for their help with the microscopy facilities at Lehigh, which are among the best in the country thanks to their efforts. This project often required the microscopes to be utilized in ways that had never been done here before, and these guys were helpful with every step along the way. Furthermore, I would like to thank Anne Marie Lobely, Janie Carlin, Sue Stetler, and Katrina Kraft for the unsung support they provide the department. I would also like to thank my fellow grad students for their help, advice, and friendship over the years. This list includes: my fellow groupmates (Jeff, Wanjun, Kittisun, Pat), the basketball players (Ken, Qian, Weihao, JJ), the climbers (Dan, JC, Lauren), the fantasy football leaguers (Jeff, Brett, Kylan), and everyone else I typically interacted with on a daily basis. I also need to thank my family for their support throughout my decade of college. This also includes my fiancée Amanda Beebe, without whom none of this matters anyway. I am very much looking forward to starting the next stage of my life with her. Finally, I must acknowledge that the financial support for this project came from NSF grant DMR-0804528. Without this support, none of the work presented here would have been possible, nor would I have received my stipend over the past 4 years.

TABLE OF CONTENTS

ABSTRACT **1**

1. INTRODUCTION **2**

2. BACKGROUND **4**

2.1 Grain boundary segregation in Cu-Bi alloys **4**

2.1.1 Thermodynamics of equilibrium grain boundary segregation *4*

2.1.2 Cu-Bi as a model system for studying grain boundary segregation *6*

2.1.3 Methods for quantitative measurement of boundary solute concentration *6*

2.1.4 Observed trends in segregation of Bi to Cu grain boundaries *10*

2.2 Bi-induced grain boundary embrittlement in Cu **12**

2.2.1 Experiments on polycrystalline Cu *12*

2.2.2 Experiments on Cu bicrystals *14*

2.2.3 Small-scale mechanical testing of Cu-Bi *17*

2.2.4 Proposed mechanisms of embrittlement *19*

2.3 Small-scale fracture toughness testing **21**

2.3.1 Micro-cantilever bend testing *22*

2.3.2 Notched micro-tensile testing *24*

2.3.3 Effect of specimen size on fracture toughness *25*

3. EXPERIMENTAL PROCEDURE **28**

3.1 Bulk polycrystalline Cu specimen preparation **28**

3.1.1 Creation of Cu-Bi alloy *28*

3.1.2 Metallographic preparation and SEM analysis *29*

3.1.3 Ion channeling imaging *31*

3.2 Bulk bicrystal specimen preparation **32**

3.2.1 Bi-doping of bicrystals *32*

3.2.2 Metallographic preparation and SEM analysis *33*

3.3 Notched micro-tensile specimen fabrication **33**

3.3.1 Ion-beam imaging of boundary and initial FIB milling *34*

3.3.2 Extraction of specimen from bulk and defining thickness and width of test specimen *35*

3.3.3 Attaching specimens to test device and final fabrication steps *36*

3.4 Un-notched single crystal specimen fabrication **37**

3.5 *In-situ* micro-tensile testing **37**

3.4.1 PI-85 nanoindenter and PTP devices *38*

3.4.2 Pre-test setup *39*

3.4.3 Testing Procedure *39*

3.4.4 Determination of stress and strain *40*

4. RESULTS AND DISCUSSION **41**

4.1 EBSD analysis of bicrystals **41**

4.2 SENT testing of 13˚ boundary **41**

4.2.1 Discussion of test results *42*

4.2.2 SEM imaging of fracture morphology *43*

4.2.3 Calculation of fracture toughness *44*

4.2.4 Further discussion of results and impacts on future tests *44*

4.3 DENT testing of 6° boundary 46

4.3.1 Discussion of test results 46

4.3.2 SEM imaging of fracture morphology 47

4.3.3 Calculation of fracture toughness 49

4.3.4 Comparison with 13° boundary results 50

4.4 DENT testing of 33° boundary 51

4.4.1 Discussion of test results 51

4.4.2 SEM imaging of fracture morphology 52

4.4.3 Calculation of fracture toughness 52

4.5 Further discussion of testing results and comparison with literature 53

4.5.1 Effect of misorientation angle on embrittlement 53

4.5.2 Comparison with Cu-Bi studies using notched micro-cantilever testing 54

4.5.3 Validity of toughness values 56

4.6 Microtensile testing of un-notched single crystal specimen 58

4.7 Finite element modeling 60

4.7.1 Modeling of single-crystal bowtie specimen 61

4.7.2 Modeling of DENT bicrystal specimens 63

5. CONCLUSIONS 71

6. SUGGESTIONS FOR FUTURE WORK 73

7. REFERENCES 76

VITA 159

LIST OF TABLES

Table 1. Fracture toughness values calculated from SENT tests on 13˚ boundary. 80

Table 3. Fracture toughness values calculated from DENT tests on 6˚ boundary..... 80

Table 5. Fracture toughness values calculated from DENT tests on 33˚ boundary..... 80

Table 6. Hardening law constants used in single-crystal plasticity FEM code. Values were determined by fitting to results of single-crystal microtensile test. 80

LIST OF FIGURES

Fig. 1. Grain boundary enrichment ratio vs. atomic solid solubility for a variety of binary alloy systems[5]..... 81

Fig. 2. AES spectra collected from Cu specimens containing different amounts of Bi[7].. 82

Fig. 3. Bright-field TEM image of a grain boundary in Cu showing diffraction contrast between the grains[17]..... 83

Fig. 4. Quantitative EDS map depicting the concentration of Bi at a Cu grain boundary [17]. 84

Fig. 5. Ratio of Bi to Cu counts in EDS spectra taken along a line perpendicular to a grain boundary located at x=0[17]..... 85

Fig. 6. Atomic resolution STEM images of a (a) pure and (b) Bi-doped symmetric 36.8° <001> tilt boundary[19]. Bright spots visible in (b) but not in (a) represent Bi atoms segregated to the boundary in a periodic arrangement. 86

Fig. 7**.** EELS spectra taken in bulk Cu and near a Bi-doped boundary showing a difference in the electronic structure of atoms near the boundary [19]..... 87

Fig. 8. Grain boundary Bi concentration (*cj*) vs. bulk Bi concentration (*cv*) for <001> tilt boundary (misorientation angle unknown)[9]..... 88

Fig. 9. Distribution of Bi boundary coverage for a large number of boundaries in polycrystalline Cu. Results shown are from both AES and AEM (labeled as STEM-XEDS)[12]..... 89

Fig. 10. Grain boundary Bi concentration as a function of misorientation angle for <100> tilt boundaries[9]..... 90

Fig. 11. Fracture stress as a function of intergranular Bi concentration for a 20.05° [110] tilt bicrystal determined by post-fracture AES[10]..... 91

Fig. 12. Fracture stress as a function of misorientation angle and annealing time for pure and Bi-doped [001] tilt bicrystals[31]..... 92

Fig. 13. SEM image of a FIB-machined notched micro-cantilever in amorphous Ni-P alloy[40]..... 93

Fig. 14. Schematic diagram of FIB-machined notched micro-cantilever with pentagonal cross-section[42]..... 94

Fig. 15. Load-displacement curves from micro-cantilever tests on individual grain boundaries in Bi-doped Cu[35]. Purple curve (GB1) shows brittle fracture caused by grain boundary embrittlement and green curve (GB2) shows classic ductile behavior due to a lack of Bi segregated to boundary..... 95

Fig. 16. Stress-strain curves generated from notched microtensile tests on (A) Au and (B) Al films[43]. Both curves show signs of plastic deformation prior to catastrophic failure..... 96

Fig. 17. Schematic plot of fracture toughness as a function of inverse specimen thickness[44]. Thicknesses greater than t_2 qualify as plane strain conditions. Thicknesses near t_1 are considered to be plane stress. Note that for specimens smaller than this the toughness begins to decrease again and will trend towards zero for very small specimens..... 97

Fig. 18. Fracture toughness as a function of specimen thickness in various Cu foils[45].... 98

Fig. 19. Bi-encrusted polycrystalline Cu rod encapsulated in evacuated glass tube for heat treating. 99

Fig. 20. EBSD map of polycrystalline Cu-Bi rod showing large grains and annealing twins. 100

Fig. 21. (a) SEM image of a group of triple points surrounding a small grain in polycrystalline Cu-Bi. Also shown are EDS maps of same area showing location of (b) Cu and (c) Bi. 101

Fig. 22. FIB image of specimen during fabrication from polycrystalline Cu-Bi rod. Ion-channeling contrast shows location of boundary on the surface as well as on the specimen itself. Note the large inclination angle of the boundary beneath the surface. 102

Fig. 23. FIB image of bicrystal sample showing extremely straight boundary as well as location of protective Pt layer deposited on surface. 103

Fig. 24. FIB image of bicrystal specimen during fabrication. Note the almost negligible inclination of the boundary beneath the surface of the sample. 104

Fig. 25. FIB image showing the location of two specimens in close proximity to each other. This was done in order to reduce FIB milling time as well as ensure that variations in boundary character from one specimen to the next were minimal. ... 105

Fig. 26. FIB image showing locations of several removed specimens from a single boundary. 106

Fig. 27. FIB image showing extraction of a specimen from the bulk using a sharp W plucker needle. 107

Fig. 28. FIB image of specimen mounted onto Cu grid following extraction from bulk. 108

Fig. 29. FIB image showing specimen following thinning steps. Specimen is ~1.0 μm thick at this point. 109

Fig. 30. FIB image of specimen after defining width of specimen to be ~6 μm with the long axis perfectly perpendicular to boundary seen in center of specimen. 110

Fig. 31. FIB image showing placement of test specimen on PTP device using W plucker needle again. Once in place, specimen will be Pt-tacked down and cut free from needle. 111

Fig. 32. FIB image of specimen after being Pt-tacked in place on PTP device..... 112

Fig. 33. SENT test specimen after notching at the boundary (on top edge). Contrast seen in left grain is due to excess Pt deposited on surface of specimen. 113

Fig. 34. DENT test specimen after notching at boundary and deposition of Pt-markers for DIC strain measurement. 114

Fig. 35. Un-notched single crystal microtensile specimen after attaching to PTP device and deposition of Pt-markers. 115

Fig. 36. Low magnification SEM image of PTP device with specimen attached and nanoindenter tip just out of contact with loading pad. 116

Fig. 37. Load schedule used in fracture tests. Note the built-in periodic holds so that high quality SEM images could be taken for DIC. 117

Fig. 38. EBSD map of bicrystal sample showing extremely straight boundary and no annealing twins. 118

Fig. 39. Pole figure created from EBSD map of 6˚ boundary showing one common axis (twist axis) and a difference of 6˚ between center spots. 119

Fig. 40. Pole figure generated from EBSD map of 13˚ boundary showing one common axis (<001> twist) and 13˚ misorientation angle between other axes. 120

Fig. 41. Pole figure generated from 33˚ boundary showing one common axis (twist axis) and 33˚ misorientation between other axes. 121

Fig. 42. Load-displacement curves generated from SENT testing of 13˚ boundary. In these tests, displacement was measured by the indenter transducer. 122

Fig. 43. Stress-strain curves generated from SENT testing of 13˚ boundary. Elastic slopes are neither consistent nor accurate, illustrating the need for direct strain measurement using DIC. 123

Fig. 44. Post-mortem SEM image of pure 13˚ SENT specimen showing transgranular fracture and evidence of significant plasticity. 124

Fig. 45. Post-mortem SEM image of doped 13˚ specimen showing some evidence of plasticity and a nearly intergranular failure. 125

Fig. 47. Stress-strain curves generated from DENT testing of 6˚ boundary showing significant plasticity prior to failure in both specimen types. 126

Fig. 48. Elastic region of stress-strain curve from 6˚ pure specimen showing a modulus of 44 GPa. This value is lower than the <100> modulus of Cu (66.7 GPa) due to the reduced cross-sectional area in between the notches. 127

Fig. 49. Elastic region of stress-strain curve from 6˚ doped specimen showing a modulus of 64.8 GPa. This value is larger than that measured for the 6˚ pure specimen, but is still within an acceptable range of the anticipated value. 128

Fig. 50. Post-mortem SEM image of a 6˚ pure specimen showing a transgranular, shear-like failure. 129

Fig. 51. Post-mortem SEM image of a doped 6˚ specimen showing a similar fracture morphology to the pure specimen in Fig. 50. 130

Fig. 52. SEM image acquired during testing of 6˚ pure specimen. Image represents the last data point on the stress-strain curve. Note that there are no slip steps present on the surface of the specimen yet, but some crack opening has occurred. 131

Fig. 54. Stress-strain curve generated from DENT testing of 33˚ boundary showing a lower fracture stress as well as lower fracture strain for doped specimens. 132

Fig. 55. Post-mortem SEM image of 33˚ pure DENT specimen showing transgranular, shear-like failure similar to that seen in 6˚ specimens. 133

Fig. 56. Post-mortem SEM image of 33˚ doped DENT specimen showing clear intergranular fracture as well as significantly less evidence of plasticity, consistent with the stress-strain curve shown in Fig. 54. 134

Fig. 55. Determination of validity of fracture toughness value for 33˚ doped specimen based on ASTM E399 specification[49]. 135

Fig. 58. Grain boundary energy as a function of misorientation angle for <001> tilt boundaries[31]. 136

Fig. 59. Grain boundary energy as a function of misorientation angle for <001> twist boundaries[48]. 137

Fig. 60. End-on SEM image of microcantilever specimens used by Amrstrong *et al.*[35]. 138

Fig. 59. Stress-strain curve generated from single-crystal bowtie micro-tensile specimen. 139

Fig. 60. Linear fit to elastic portion of curve in Fig. 59 showing a modulus of 72.2 GPa, which is in fairly good agreement with the expected <100> modulus of Cu (66.7 GPa). 140

Fig. 61. Elastic modulus of Cu vs. misorientation from <100> direction. The fact the modulus stays fairly constant over this range means that slight misalignment of actual test specimens relative to the boundary is tolerable. 141

Fig. 62. Post-mortem SEM image of single-crystal specimen showing similar shear-like appearance to pure bicrystal specimens. 142

Fig. 63. FEM model of single-crystal bowtie specimen showing both geometry of part and mesh. 143

Fig. 64. Uniaxial stress from FEM simulation of single-crystal bowtie specimen showing uniform stress in most of gauge section, with a slight stress concentration at the transition point. 144

Fig. 65. Uniaxial displacement of single-crystal bowtie specimen showing 0 displacement at center of specimen (defined as fixed in model). Also shown is the node used for calculation of strain (identified by red dot on bottom edge of part). 145

Fig. 66. Stress-strain curve showing good fit between FEM simulation and experimental data from single-crystal bowtie specimen. Simulation uses hardening parameters listed in Table 6. 146

Fig. 67. Elastic portions of stress-strain curves generated from FEM simulations of single-crystal specimen using different nodes for strain calculation. Blue curve used the point described before at the end of the gauge section. The red curve used a node that was ~1 μm past the end of the gauge section. The very similar slopes of these curves suggests that the exact location of the Pt markers on the actual test specimens is not crucial. 147

Fig. 68. FEM model of bicrystal DENT specimen utilizing quarter-symmetry (mirror planes in width and thickness dimensions). Note that the mesh is significantly finer in the vicinity of the notch. 148

Fig. 69. 2-D image of bicrystal DENT FEM model showing finer mesh near notch. 149

Fig. 70. Zoomed in view of mesh near the notch of bicrystal DENT FEM model..... 150

Fig. 71. Contour map of uniaxial stress for 6˚ bicrystal specimen. Note the very slight asymmetry in stress distribution across the boundary due to misorientation. 151

Fig. 72. Contour map of uniaxial stress for 33˚ bicrystal specimen. Note the much more pronounced asymmetry in stress distribution across the boundary due to larger misorientation angle. 152

Fig. 73. Uniaxial displacement contour map for 6˚ bicrystal showing zero displacement at bottom surface (fixed). 153

Fig. 74. Stress-strain curves generated from FEM modeling of DENT bicrystals. Note that the curves for both misorientation angles are identical and perfectly overlap. Also shown is the experimental data from a 6˚ pure specimen. 154

Fig. 75. Elastic portion of FEM curves shown in Fig. 74. Note that both curves are identical and have a slope of ~59 GPa. 155

Fig. 76. Plastic zone (shown in red) for 6˚ FEM model prior to elastic limit of stress-strain curve. Image shows that the plastic zone is very symmetric with respect to the boundary, as is expected for a low angle boundary. 156

Fig. 77. Plastic zone (shown in red) for 33˚ FEM model prior to elastic limit of stress-strain curve. Image shows that the plastic zone is asymmetric with respect to the boundary, as is expected for a high angle boundary. 157

Fig. 78. Plastic zone in 33˚ FEM model at elastic limit of stress-strain curve. This image represents the first simulation step where the plastic zone encompassed the entire specimen width. 158

ABSTRACT

Grain boundary embrittlement in the Cu-Bi alloy system was investigated using small-scale fracture toughness tests that were based on commonly used bulk-scale tests. Tests were conducted on pure and Bi-doped <001> twist Cu bicrystals with misorientation angles of 6, 13, and 33˚ in order to determine the effect of misorientation angle on the degree of embrittlement. The results of these tests showed that the 6˚ grain boundary was nearly immune to embrittlement, showing little to no differences in fracture toughness values and failure mechanisms between the pure and doped specimens. However, the 33˚ boundary exhibited a significant amount of embrittlement, with a nearly 40% decrease in fracture toughness in the doped specimens compared to the pure and a distinct shift in the failure mechanism from transgranular shear to intergranular fracture. The 13˚ boundary exhibited an intermediate amount of embrittlement with a measurable drop in toughness, but not a clear shift in the failure mechanism. These results are consistent with previously published results from tests on bulk-scale bicrystals.

Furthermore, a single-crystal plasticity model was incorporated into a commercial finite element software package (ABAQUS) in order to investigate the development of the plastic zone in front of the notches created in the test specimen. It was found that the size of this zone was likely constrained by the specimen dimensions, which had a significant impact on the measured fracture toughness values.

1. INTRODUCTION

Grain boundary embrittlement (GBE) is an important area of research due to its impact on processing of a wide range of alloy systems. The work presented here will focus on the embrittlement of Cu by Bi, a naturally occurring impurity in Cu ores that must be removed prior to rolling into sheets or drawing into wires. However, there are a number of other technologically important examples of GBE that have been studied as well, including (but not limited to) the temper embrittlement of steels, Ni-S, and Al-Ga. While this work will focus on only one alloy system, the conclusions drawn from it will likely have importance to a much larger number of systems.

The embrittlement of Cu by Bi segregated to grain boundaries has been an area of scientific research for well over 100 years, but the fundamental mechanism behind the embrittlement is still not understood. Several different mechanisms have been proposed, but thus far, none have been universally accepted. Overall, there are three branches of research related to this embrittlement that have been investigated: (1) mechanical testing of multiple or individual boundaries, (2) chemical analysis of an individual boundary, and (3) modeling and/or direct observation of the atomic structure of individual boundaries. However, the primary reason that the underlying mechanism is still up for debate is that no study has yet to combine all three of these branches.

A significant amount of work has been done solely on the segregation of Bi to Cu grain boundaries, but these studies do not include (and in some cases, completely ignore) the implications of impurity segregation to grain boundaries on the mechanical properties of the material. On the other end of the spectrum, a number of studies have been

conducted to specifically measure the mechanical properties of embrittled boundaries. Many of these studies even include some level of chemical analysis of the boundary, but none have attempted to relate the observed embrittlement to the atomic structure of the boundary. In order to properly prove what mechanism is responsible for the embrittlement, all three of these branches must be utilized in one comprehensive study that systematically addresses and rules out proposed mechanisms until only one is left standing. The work presented in this document is focused on the mechanical testing of individual grain boundaries, and represents one-third of this type of comprehensive study that is intended, upon completion, to shine new light on an area of research that has perplexed scientists for over a century. The other components of this study, namely chemical analysis and atomic-resolution imaging of the same grain boundaries, are currently being investigated by another student at Lehigh.

2. BACKGROUND

2.1 Grain boundary segregation in Cu-Bi alloys

It has been known for nearly 200 years that a small amount of Bi can cause a significant reduction in strength and ductility of pure Cu. Much of this early work was summarized by Bannister and Doyle[1]. Voce and Hallowes[2] later suggested that a thin film of elemental Bi was responsible for the embrittlement based on the extremely low solubility of Bi in bulk Cu. While the technology needed to prove this theory did not exist at the time, it would ultimately be proven to be correct. Therefore, in order to fully understand the embrittlement of Cu by Bi, it is necessary to understand the boundary segregation that lies at its root. The following sections will discuss the thermodynamic driving forces responsible for boundary segregation, as well as commonly used experimental techniques for measuring the concentration of segregant atoms contained in grain boundaries.

2.1.1 Thermodynamics of equilibrium grain boundary segregation

There are two different classes of grain boundary segregation than can occur. The first of these is known as non-equilibrium segregation and is typically found in cast metals and is developed during solidification. This type of segregation is deemed "non-equilibrium" because the solute concentration gradients can be irreversibly eliminated by an appropriate heat treatment. While this phenomenon has very important practical implications for manufacturing processes, it is less interesting in terms of fundamental

science because it can be easily eliminated. The other class of segregation is known as equilibrium segregation and is caused by thermodynamic forces that cannot be avoided.

Most thermodynamic models of boundary segregation are derived from gas-adsorption theories. McLean[3] developed the first of these models and derived the following relation:

$$\frac{X_B}{X_{B_0} - X_B} = \frac{X_C}{1 - X_C} \exp\left(\frac{E_1}{RT}\right) \tag{1}$$

where X_B is the solute concentration at the boundary, X_{B_0} is the saturation concentration at the boundary (equivalent to a close-packed monolayer), X_C is the bulk solute concentration in the alloy, E_1 is the grain boundary adsorption energy, R is the universal gas constant, and T is temperature. This equation correctly predicts that the boundary concentration increases with both increasing bulk concentration as well as decreasing temperature. However, this model cannot be applied to systems that exhibit more than a monolayer of boundary segregation. Brunauer *et al.*[4] developed a more rigorous model, known as the BET theory, which could handle multilayer segregation. However, when applied to a system that exhibits monolayer or less segregation, the theory simplifies into the following form:

$$\frac{X_B}{X_{B_0} - X_B} = \frac{X_C}{X_{C_0}} \exp\left(\frac{E}{RT}\right) \tag{2}$$

where X_{C_0} is the bulk solute solubility limit. This equation looks similar to the McLean theory and also predicts that segregation will increase with increasing bulk solute concentration. However, by including the bulk solubility limit, a practical upper bound has been placed on the boundary concentration.

2.1.2 Cu-Bi as a model system for studying grain boundary segregation

Using the simplified BET theory, Seah and Hondros[5] defined a quantity β, known as the grain boundary enrichment ratio, as follows:

$$\beta = \frac{X_B}{X_{B_0}} \frac{1}{X_C} \tag{3}$$

Assuming that X_{B0} is a constant, β is simply the ratio of the boundary concentration to the bulk concentration. Therefore, β defines the severity of boundary segregation for a given alloy system and should be inversely proportional to the bulk solubility limit according to Eq. 2. Fig. 1 shows β plotted versus $1/X_{C0}$ for a variety of binary alloy systems known to exhibit boundary segregation. According to this plot, Cu-Bi has the highest β value of any binary alloy system, making it the ideal model system for studying boundary segregation.

2.1.3 Methods for quantitative measurement of boundary solute concentration

In general, there are a number of different experimental techniques that can be used to measure the composition of a material. However, only a few of these techniques are applicable to the study of grain boundary segregation. In order for this to be possible, a technique must have extremely high spatial resolution, as the volume of a grain boundary is small. In addition, the technique must be able to detect a very small concentration of segregant atoms, as the number of solute atoms can be as few as a monolayer or less. Therefore, only two techniques have typically been used to measure Bi concentrations at Cu grain boundaries: Auger electron spectroscopy (AES)[6–12] and analytical electron microscopy (AEM)[12–19].

AES uses a low energy electron beam (typically 3 keV or less, but can be higher) to ionize atoms on the surface of a sample. During this process, Auger electrons escape from the surface with an energy level characteristic to the atomic number of the atom they originated in. Therefore, by capturing these electrons and measuring their energies, both the type and concentration of elemental species present in the sample can be determined. Fig. 2 shows several AES spectra collected from Cu grain boundaries containing a varying amount of Bi[7]. In all spectra, it is clear that the predominant species is Cu due to its significantly larger peak at ~50 eV. The spectrum labeled "I" contains the highest concentration of Bi, evidenced by the largest peak at ~100 eV (characteristic of Bi). It can further be concluded that spectrum "II" has an intermediate amount of Bi and "III" is essentially pure Cu. The primary benefit of AES is that it has an extremely high spatial resolution, both in the lateral direction (less than 10 nm) and in depth (only a few atomic layers). This high resolution comes from a combination of a small electron probe size and the limited escape depth of low-energy Auger electrons (on the order of 100 eV). However, because AES is essentially a surface measurement, it is very sensitive to the quality of the surface to be analyzed. Any contamination or oxide layer on the surface will have a significant negative impact on the results. Therefore, in order to study boundary segregation using AES, test specimens, which can be bi- or polycrystalline, must be fractured just prior to analysis in the high-vacuum microscope chamber. While this inherently offers the ability to combine mechanical test results with chemical analysis of the fractured boundary (or boundaries in polycrystals), it also creates some limitations. The first of these limitations is obvious: AES can only be performed on boundaries that

have already been broken. For polycrystalline samples, this means that only those boundaries that the crack propagated along can be analyzed. In general, these boundaries will tend to be the most embrittled boundaries, as they offer the least resistance to fracture. Therefore, it is impossible to use AES to study those boundaries that exhibit less than the maximum amount of embrittlement. For bicrystalline samples, this means that the fracture must be nearly perfectly intergranular. If the crack wanders more than a few atomic layers away from the boundary, as was observed by Wang[20], then AES will be useless as the boundary will not lie in the analysis volume.

AEM is a relatively newer technique that combines scanning transmission electron microscopy (STEM) with X-ray energy dispersive spectroscopy (EDS) and/or electron energy loss spectroscopy (EELS). Similarly to AES, AEM is based on the ionization of atoms in the specimen by an incident electron beam. However, there are two fundamental differences between the techniques. First, the typical accelerating voltage used to generate the electron probe in AEM is between 100-300 keV (1-3 keV for AES). Second, AEM uses an x-ray detector to measure x-rays that are emitted from the sample during the ionization process rather than measuring Auger electrons in AES. These x-rays have characteristic energies associated with the element they originated from, but are typically much higher than those of Auger electrons. An EELS detector may also be used to gather information regarding the chemistry of the specimen from the amount of energy lost by the transmitted electrons.

Some of the seminal work using AEM to measure Bi concentrations in Cu grain boundaries was conducted at Lehigh in the 1980s and 1990s[13–18]. Figs. 3-5 show the

results of an AEM study by Keast and Williams[17] where Bi was observed to be segregated to a Cu grain boundary. Fig. 3 shows a bright-field transmission electron microscope (TEM) image of a grain boundary in Cu illustrating diffraction contrast between the two grains. Fig. 4 shows a quantitative EDS map showing the location and concentration of Bi atoms. As expected, the Bi atoms are confined to the boundary, with any signal outside of the boundary due entirely to noise. Fig. 5 shows a plot of the Bi/Cu peak intensity ratio in the EDS spectra used to generate the map in Fig. 4. Spectra were integrated over a width of 5 pixels, which corresponds to a spacing of the data points shown of 1.3 nm. Looking at these results, it is clear that AEM is a powerful tool for studying grain boundary segregation. However, while it offers some advantages over AES, primarily that specimens do not need to be carefully broken prior to analysis, it is not without its limitations and challenges. Perhaps the most important of these is that the specimen thickness must be accurately known in order for proper quantification to be possible, which is not a trivial matter considering that thickness often varies with position due to the wedge-shaped nature of most TEM specimens.

More recently, improvements in microscopes have improved the spatial resolution of AEM down to the atomic level (as low as ~0.4 nm in some cases)[21]. Using this modern technology, Duscher *et al.*[19] acquired atomic-resolution STEM images of a Cu grain boundary in both pure and Bi-doped conditions, shown in Fig. 6. These images show the local atomic structure of the boundary and where Bi atoms, which appear as the brighter spots in (b), will preferentially sit in the boundary. EELS spectra taken from the boundary region were compared to those taken from the bulk in an effort to determine whether the

Bi atoms changed the electronic structure of Cu atoms near the grain boundary. These spectra, shown in Fig. 7, suggest that there is a difference in the density of states (DOS) near a Bi-doped boundary versus bulk Cu. It is concluded that this change in bonding nature near the boundary is ultimately responsible for boundary embrittlement, which will be discussed in more detail in a later section.

2.1.4 Observed trends in segregation of Bi to Cu grain boundaries

A significant amount of work has been conducted using both of the techniques discussed in the previous section to measure the Bi segregation to numerous different types of Cu grain boundaries. Throughout all of this work, a few trends have emerged. First, the concentration of Bi contained in a particular boundary is a function of the overall Bi concentration, as predicted by the thermodynamic models discussed earlier. However, in reality this relationship is not as simple as predicted. As shown in Fig. 8, Fraczkiewicz and Biscondi[9] showed that the intergranular concentration of Bi increased with increasing bulk Bi content, but only up to ~200 μg/g (~0.02 wt. %). Above this value, precipitation of a secondary Bi-rich phase was observed, resulting in a decrease in the intergranular concentration.

Another trend that has emerged is that the segregation behavior is extremely dependent on the nature of the boundary being studied. Atomistic modeling has been used to determine that the segregation behavior different boundaries will vary due to the differences in local atomic structure[22,23]. This conclusion has been experimentally validated by multiple studies[7,8,12–14,17] that show a distribution in the boundary concentration in a polycrystalline sample, as shown in Fig. 9[12]. There are two important

conclusions that can be drawn from this plot. The first is that AES cannot measure a boundary coverage of less than ~0.3 monolayers. This is because boundaries with that level of segregation tend not to be brittle enough to fracture, meaning that they are not available for analysis with AES, as previously discussed. Therefore, using only AES to measure boundary concentrations will artificially increase the average segregation level as a significant fraction of boundaries exhibit segregation below this level. The second is that there is a very wide distribution in the segregation behavior, with some boundaries showing no Bi concentration and others showing more than 2 monolayers worth of boundary coverage. This is important to keep in mind when comparing the results from multiple experiments, as it is unlikely that the boundaries studied in different works are identical. Different conclusions about the segregation (and resulting embrittlement) can be drawn from different experiments, depending on the nature of the specific boundaries studied in each. Furthermore, the change in electronic structure of Cu atoms located near a Bi-doped boundary seen by Duscher[19] is not universally observed by others. In fact, several studies[15,24] report seeing this change in some boundaries but not in others.

While the misorientation angle or CSL designation of a random grain boundary in a polycrystalline sample does not correlate directly with the Bi concentration, Fraczkiewicz and Biscondi[9] showed that for a given boundary type (<100> tilt), the misorientation angle is related to the intergranular Bi concentration, shown in Fig. 10. In this plot, it is clear that low angle boundaries will contain significantly less Bi than high angle boundaries. The difference is great enough that low angle boundaries typically do not exhibit brittle intergranular fracture at all (marked as "DF" for ductile fracture),

making them unavailable for study by AES. Unfortunately, the cause of the minima at ~45° is not explained and appears contradictory to the generally accepted theories on segregation. However, despite this shortcoming, this work suggests that for a given boundary type, a critical misorientation angle exists such that below that angle there is little to no Bi segregation. This is a critical conclusion to keep in mind when reading the rest of this document, as it is one of the fundamental bases for the work conducted.

2.2 Bi-induced grain boundary embrittlement in Cu

While grain boundary segregation may be a very interesting topic from a scientific viewpoint, the reason it is so important for real-world applications is that it can be extremely detrimental to the mechanical properties of materials. In the case of Cu, a very small amount of Bi can severely limit its ductility, making it too brittle to be drawn into wires (one of the most common uses of Cu). Dating back to the mid 1800s, a significant volume of work has been conducted to measure the properties of Bi-doped Cu and to determine the fundamental mechanism responsible for the observed embrittlement. The following sections will review and discuss these works as well as the most commonly suggested embrittlement mechanisms.

2.2.1 Experiments on polycrystalline Cu

Much of the early work involving the mechanical testing of Cu-Bi alloys dealt with trying to determine the maximum allowable Bi concentration that did not result in embrittlement[1]. However, it quickly became clear that this value was extremely low, on the order of 0.002 wt.%. While this was an important discovery, a more in-depth investigation into the properties of Cu-Bi alloys was needed in order to determine the

mechanism responsible for this embrittlement. In 1947, Voce and Hallowes[2] published such a study, and proposed that the embrittlement was due to an elemental Bi film at the Cu grain boundaries. They drew this conclusion from a large number of mechanical tests conducted on a number of different alloy compositions, as well as chemical analysis that determined the solubility of Bi in bulk Cu. Joshi and Stein[6] were the first to combine mechanical testing with AES in an effort to directly observe the relationship between embrittlement and segregation. They concluded that the Bi caused a reduction in both the grain boundary and surface energies of Cu. Thus, the energy required to create new surfaces through fracture was lessened, leading to a reduction in fracture strength.

Hondros and McLean[25] took this concept further and suggested that this reduction in cohesive strength caused local stresses at grain boundaries to be relieved by cracking rather than plastic deformation. Crack nucleation at boundaries was caused by the increased ratio of tensile stress to shear stress where slip bands in adjacent grains converged. This creates a local stress concentration that is typically relieved by plastic deformation, as the energy required to create new surfaces (fracture) is typically much higher than that for dislocation nucleation. However, it was determined that this energy in Cu-Bi alloys was ~50 % of the value for pure Cu. Therefore, it is energetically favorable to nucleate (and then propagate) a crack, rather than dissipate the energy through plasticity.

2.2.2 Experiments on Cu bicrystals

While the conclusions mentioned above are undebatably true, the fact that they were based on experiments conducted on polycrystalline samples inherently biases the results towards the most embrittled boundaries (similar to that in AES studies). In order to truly understand the mechanism behind Cu-Bi embrittlement, the behavior of a variety of individual grain boundaries needed to be investigated. Thus, a general shift towards bicrystal specimens took place in the mid-to-late 1980s.

Russel and Winter[26] tested two different types of symmetric [001] tilt boundaries and showed a dramatic difference in the fracture behavior between them. While the difference in misorientation angle between the two boundaries was not all that large (55˚ vs. 69˚), the orientations were chosen such that one grain boundary coincided with a low index crystallographic plane (and a low CSL designation, Σ5) while the other did not. The Σ5 boundary exhibited a fracture strength approximately seven times larger than the non-special boundary. The authors speculate that the Bi concentrations in each boundary might be extremely different, leading to the difference in fracture strength, but this was not tested. This work appears to be contradictory to most of the segregation studies (and some embrittlement studies to be discussed in the following paragraphs), as no direct correlation between CSL designation and segregation behavior has been observed. Furthermore, the work of Fraczkiewicz and Biscondi[9] depicted in Fig. 10 appears to be in direct contradiction to the observed results. According to this plot, a <100> tilt boundary with a misorientation angle of 55˚ has a grain boundary Bi concentration significantly

larger than a 70° boundary, suggesting that the former would be more brittle than the later.

Wang[20] conducted a fatigue test on a bicrystal with a random, non-special grain boundary and showed that the crack propagated in a zig-zag manner in the vicinity of the boundary with significant faceting on the fracture surface. Based on the appearance of these facets, it was determined that the fracture mechanism was a combination of cleavage along {110} planes and plastic shear along {111} planes in the {110} direction. This competition between failure mechanisms is not entirely surprising given the random nature of the boundary studied. Final fracture of the specimen occurred when the stress intensity factor, K, reached a value of 2.6 MPa·m$^{1/2}$, corresponding to an energy release rate, G, of 54 J/m^2. This is an extremely low value for a metal specimen and is the first reported value of an experimentally measured fracture toughness value for a Bi-doped Cu grain boundary.

Li *et al.*[10] showed that the fracture behavior of a particular grain boundary was heavily dependent on the boundary concentration of Bi, as measured by post-mortem AES. This trend is shown in Fig. 11. This expected trend is accompanied by a shift in the fracture mechanism from transgranular shear for the pure boundary, to a mix between intergranular and shear for the intermediate doping levels, and eventually to a pure intergranular fracture with no appreciable plasticity for the highest doping levels. A similar trend was observed by Chikwembani and Weertman[27,28] in fatigue tests on doped bicrystals. This suggests that there is a critical boundary concentration level required to

shift the fracture mechanism from trans- to intergranular, a conclusion supported by the curve in Fig. 10.

Wang and Anderson[29] conducted fracture tests on symmetric [110] tilt boundaries with CSL designations of Σ11 (129.5˚ misorientation) and Σ9 (38.9˚) and a [100] Σ5 boundary (37˚). It was observed that the Σ11 boundary could not be embrittled, the Σ5 boundary was the most susceptible to embrittlement, and the Σ9 boundary fell in between, depending on Bi concentration and crack growth direction. This behavior was explained using the Rice-Thomson model[30], which predicts whether a cracked interface will behave in a ductile or brittle fashion. The critical ratio for this detemination is between the energy release rates for dislocation emission from the crack tip, G_{disl}, and for interfacial cleavage, G_{cleav}. Whichever of these values is lower for a given crack configuration will correspond to the more favorable deformation mode (i.e. if $G_{disl} < G_{cleav}$, then dislocation emission will be preferred). It was determined that G_{disl} can vary by several hundred percent among the boundaries studied due to changes in crystallography, primarily the relative orientations of the crack growth direction and potential slip systems in each grain. It was assumed that G_{disl} is unaffected by the presence of impurity atoms segregated to the boundary. G_{cleav} was calculated to vary by up to ~30% for the boundaries studied based on differences in surface energy between the different boundary planes (again, ignoring the effect of segregant atoms). It was predicted that Bi segregated to each of the grain boundaries could lower G_{cleav} by up to 36% by lowing the interfacial energy as described above. Using these values, it was possible to predict the fracture behavior of the bicrystals tested with fairly good agreement,

suggesting that the fracture behavior of a given bicrystal (pure or Bi-doped) can be predicted using this relatively simple energetic model.

In a more systematic study, Li and Zhang[31] investigated the effect of misorientation angle and Bi concentration on the fracture behavior of [001] tilt boundaries. Several important conclusions were drawn from the results of this study, which are shown in Fig. 12. First, the fracture stress for a given boundary type decreases with increased Bi concentration. This is not a new conclusion, but this study does a very good job of showing it for a number of different boundaries. Second, it appears that a critical misorientation angle exists at ~20˚, below which embrittlement is essentially nonexistent and the fracture will be transgranular and ductile. Above this angle it appears that the fracture stress and morphology will vary with Bi concentration up to a point, but there is a limit on how low the fracture stress will be. This conclusion is consistent with previously discussed studies of boundary segregation, both theoretical[4] and experimental[9]. Unfortunately, since no attempt was made to measure the Bi concentration at each of the grain boundaries studied (AES would have been ideally suited for this), any conclusions about the relationship between segregation and embrittlement are only speculative. However, despite this shortcoming, this work represents the most systematic study of boundary embrittlement to date, and acts as a model for the work that will be presented later in this document.

2.2.3 Small-scale mechanical testing of Cu-Bi

Over the last 25 years or so, small-scale testing has become a much more commonly used method for measuring the mechanical properties of materials. While

much of this work has been focused on measuring the elastic and plastic properties of materials[32,33], there has been some work done in the area of fracture toughness measurement. A more detailed discussion of the available techniques for conducting micro-scale fracture tests can be found in the next section of this chapter. For now, it is sufficient to say that small-scale testing offers some advantages over the bulk-scale tests that were used exclusively in the previously discussed works. The most important of these is that multiple tests can be conducted out of a specimen that would previously yield only one test. Although the preparation time for these tests can be much longer, it offers the potential for better statistics in the measurements than bulk-scale tests where only one result can be obtained.

Armstrong *et al.*[34,35] used a micro-cantilever based approach to measure the toughness of a wide range of individual grain boundaries in a bulk Bi-doped Cu poly-crystal. This approach eliminates the bias inherent to bulk tests on polycrystalline specimens as it allows all boundaries to be tested, not just the most brittle ones. They showed that the behavior of the boundaries tested was bi-modal: a boundary was either extremely brittle and showed no plasticity prior to fracture, or it was extremely ductile and could not be fractured at all. The authors claim that AEM revealed Bi on all brittle boundaries and none on all ductile ones. This bi-modal distribution is consistent with the AEM/AES work on segregation by Keast *et al.*[12]. Among those boundaries that did fracture, K_c ranged from 2.7-7.2 MPa·m$^{1/2}$, in good agreement with other reported values. However, no trend with misorientation angle, boundary plane, or CSL-designation was seen (again, in agreement with the segregation work by Keast *et al.*[12]). This is not entirely

surprising, given that the boundaries tested can be viewed as random boundaries (RBs). No two boundaries shared any common characteristic, so it is almost expected that no trend based on a single characteristic would emerge, as was seen in the work by Li and Zhang discussed previously[31]. Furthermore, since the boundaries that do not contain Bi deformed in a ductile fashion and no toughness value could be obtained, no quantification of the embrittlement could be measured. However, this work does show the usefulness of small-scale mechanical testing in this area, as a larger number of individual boundaries were tested in this one work than in many previously published studies combined.

2.2.4 Proposed mechanisms of embrittlement

It is without question that the embrittlement of Cu by Bi is caused by grain boundary segregation. However, as microscope technology improves and scientists are able to image materials on the atomic scale, the questions regarding boundary embrittlement have shrunk down to this scale as well: What effect do Bi atoms segregated to a grain boundary have on the Cu atoms located nearby that causes the boundary to weaken?

The simplest theory to understand is based on the difference in atomic size between Cu and Bi. This theory, supported by several[22,36,37], states that the presence of large Bi atoms in a grain boundary that does not have enough free volume to accommodate the impurity will distort the surrounding crystal lattice. The primary consequence of this distortion is that the Cu-Cu bonds that originally spanned the boundary are now stretched out and weakened, resulting in a significant reduction of the energy required for intergranular fracture, G_{cleav} (recall that Wang and Anderson[29]

predicted that Bi-segregation would cause up to a ~36 % decrease in G_{cleav}). Schweinfest *et al.*[36] used atomistic modeling to conclude that in a pure Cu boundary, G_{cleav} is much larger than G_{disl}, which gives rise to the ductile, transgranular failure that is always seen in pure Cu. However, placing Bi atoms in the boundary lowers G_{cleav} so that it is just slightly less than G_{disl} for the specific boundary studied. This has two important conclusions. First, it proves that a size effect alone can be responsible for embrittlement in the Cu-Bi system. The second (and perhaps more important) conclusion is that because G_{cleav} and G_{disl} have similar values for a specific boundary type after segregation, it is not unreasonable to assume that for other boundary characters (perhaps where G_{disl} is inherently lower based on the crystallographic orientation of the two grains), G_{cleav} will still be higher after segregation. This would explain why some boundaries appear to be resistant to embrittlement. However, the atomic-resolution STEM images shown in Fig. 6 do not show any evidence of bond stretching across the boundary. A pair of images like these two showing a change in the atomic positions of Cu atoms near the boundary would serve as definitive proof of a size effect, but no such images have been published to date.

If an atomic size effect is not solely responsible for the embrittlement, then it has been proposed that an electronic effect might be[15,16,18,19]. There are several variations of this concept that have been proposed, but the one with the most traction involves an increase in the electron density near the boundary due to the presence of Bi. This could be due to the electronegativity of Bi or due to orbital hybridization; but in either case, the extra electrons near the boundary fill otherwise unoccupied antibonding states in the Cu atoms. As expected, this would result in an overall weakening of the bonds across the

interface, leading to embrittlement. The evidence for such an effect would lie in the energy-loss near-edge structure (ELNES) from EELS spectra, as shown in Fig. 7. In this plot, a clear difference in the spectra taken from the grain boundary (labeled "gb") and the bulk can be seen, suggesting that the electronic structure near the boundary is different. This evidence would be conclusive proof that an electronic effect is responsible for embrittlement, except that it is not universally observed[15,24] and in fact could be due simply to the boundary itself (i.e. it would be present in a pure boundary)[38].

So, as stated at the beginning of this document, after nearly 200 years of research the fundamental mechanism responsible for the embrittlement of Cu by Bi is still a topic of heated debate. Ultimately, it boils down to the fact that no complete data set has been developed yet that includes experimental measurements of the segregation behavior, local atomic structure, and mechanical behavior of a systematic array of grain boundaries. This section of the document has provided an overview of the available techniques for measuring the first and second of these characteristics and the following section will describe techniques for measuring the last.

2.3 Small-scale fracture toughness testing

As previously discussed, small-scale testing offers the potential to many test specimens from the same amount of material that can be used for only one bulk-scale test. However, only two of the plethora of available small-scale fracture tests are truly applicable to measuring the toughness of a single grain boundary: micro-cantilever bend testing and micro-tensile testing. These techniques are similar in that they both require the use of a focused ion beam (FIB) for sample fabrication and that testing can be carried

out *in-situ* in a scanning electron microscope (SEM) if desired. However, they have some very important differences that can have significant implications for boundary fracture testing. The following sections will give an overview of each of these techniques, with an emphasis on the advantages and disadvantages of each for this particular application.

2.3.1 Micro-cantilever bend testing

Kraft *et al.*[39] were the first to use notched micro-cantilever beams to measure fracture toughness of brittle oxide films. However, because samples were batch-fabricated using standard lithographic patterning, it would be impossible to apply this original scheme to testing individual grain boundaries in a polycrystalline film or of pre-determined bicrystals. In order for this to be possible, a technique where the location of test specimens can be individually chosen must be used.

Ichikawa *et al*.[40] developed a procedure for creating small-scale cantilevers using FIB machining, shown in Fig. 13, which would later be used by Koyama *et al*. as well[41]. While this technique does allow for precise control over specimen location, it requires that at least one dimension of the cantilever, typically thickness, be predefined. While this not a problem for a thin film, it would be difficult to do so when starting with a bulk specimen, as is typically the case in Bi-doped Cu.

Di Maio and Roberts[42] developed a similar FIB-based technique for measuring the toughness of coatings using pentagonal cantilever beams, shown in Fig. 14. While the pentagonal cross-section does create a slightly more complex stress-state in the beam, it allows the thickness of the cantilever to be defined by FIB machining as well. This means that a cantilever could be fabricated anywhere on a polished surface from a bulk material,

ideal for measuring the toughness of individual boundaries. Armstrong *et al.*[34,35] used this specimen geometry to measure the toughness of Bi-doped boundaries in polycrystalline Cu, as previously discussed.

Clearly, the FIB-machined micro-cantilever specimen offers some advantages when it comes to studying grain boundary embrittlement. These include relatively easy fabrication steps, a simple testing procedure, and the proven ability to reproduce bulk-scale fracture toughness values of embrittled boundaries. However, as with any technique, it also has its drawbacks. A critical requirement for this technique is that the grain boundary must be perpendicular to the surface of the bulk sample so that it will be perpendicular to the length of the cantilever. This is crucial in order to avoid a mixed-mode loading condition, which would make interpreting any experimental results significantly more difficult. For bulk bicrystals, this is not an issue; however, it can be for polycrystals. Therefore, steps must be taken to ensure that the microstructure of the specimen consists of columnar grains with parallel boundaries. This can be accomplished by a variety of different deformation processes (Armstrong *et al.*[34,35] used swaging). However, it must be kept in mind that subjecting the material to a significant amount of cold working will likely change its mechanical properties, namely yield strength and ductility.

While the issue of boundary alignment can be dealt with, the micro-cantilever test does come with one limitation that cannot be overcome: it only works on brittle materials. Materials that have any appreciable ductility will not fracture, as was observed when non-embrittled Cu grain boundaries were tested using this method[35]. The difference

in behavior between brittle and ductile specimens is shown in Fig. 15. Clearly, the embrittled boundary behaved exactly as a brittle material is expected to, with purely linear elastic deformation up to the point of fracture. This type of load-displacement behavior is ideal for the calculation of K_c, as it clearly satisfies the conditions for linear elastic fracture mechanics (LEFM). However, when the boundary tested was not embrittled, the load-displacement curve has the classic appearance of a ductile material with an elastic regime, a well-defined yield point, and strain hardening after yielding. Unfortunately, for a cantilever specimen, this means that a crack never propagated from the notch tip and the beam simply bent like a plastic hinge. The fact that there was a slight load drop before the test was ended (the linear segment in the load-displacement curve represents unloading) is evidence of this hinge-like behavior. Because the beam did not fracture during the test, no fracture toughness value of any kind can be calculated. In the context of Cu-Bi grain boundary embrittlement, this means that un-doped boundaries can not be tested by this technique as it is clearly established that undoped boundaries exhibit ductile failure in bulk-scale tensile tests[10,31]. Therefore, it would impossible to determine any meaningful metric for quantifying the amount of embrittlement observed in a given boundary using micro-cantilever specimens.

2.3.2 Notched micro-tensile testing

If a quantification of the embrittling effect of Bi on Cu is to be measured, a technique that allows both brittle and ductile specimens to be successfully tested is required. The only loading method that can guarantee fracture, regardless of material properties, is pure tension. With that in mind, Hosokawa *et al.*[43] conducted single edge-

notched tension (SENT) tests to measure the fracture toughness of 200-300 nm thick Au and Al films. The stress-strain curves from these tests, shown in Fig. 16, depict clear evidence of plastic deformation in both specimen types prior to final fracture. While this large-scale plasticity likely violates the requirements of LEFM, suggesting that perhaps Kc is not the most appropriate fracture toughness quantity, the fact that any fracture toughness value can be calculated at all from a ductile specimen implies that notched micro-tensile testing may be the most suitable technique for studying grain boundary embrittlement in small-scale specimens. One very important thing that needs to be noted about the results of these tests is the magnitude of the calculated fracture toughnesses: 0.45 and 0.515 MPa·$m^{1/2}$ for Au and Al, respectively. These values are extremely low for metals (typically in the 10s of MPa·$m^{1/2}$ and up) and would suggest that the materials were extremely brittle. However, when combined with the stress-strain curves that still exhibit plasticity, it becomes clear that something else is responsible for the low toughness values.

2.3.3 Effect of specimen size on fracture toughness

The observation that specimen size influences the measurement of fracture toughness in ductile metals is well understood at the bulk scale. Fig. 17[44] shows the classic example of specimen thickness affecting toughness by changing the loading condition from plane strain to plane stress. This plot shows that for very thick specimens (to the left on the *1/t* x-axis), the fracture toughness is very low and corresponds to the plane-strain fracture toughness, K_{IC}. As the specimen thickness decreases (moving to the right), the toughness rises and eventually reaches a maximum value corresponding to the

plane stress toughness. By decreasing the specimen thickness, the degree of triaxiality of the stress state ahead of the crack tip decreases because a stress can not exist perpendicular to a free surface. This decrease in stress triaxiality decreases the applied uniaxial tensile stress required for plasticity, allowing a much larger plastic zone to develop ahead of the crack. This allows much more energy to be absorbed by the material through plasticity and, in turn, increases the fracture toughness. Typically, strict requirements the dimensions of fracture toughness specimens ensure that the plane-strain conditions are met so that a "worst-case scenario"-type toughness value is reported for a material.

However, the implications of this plot for small-scale testing come from the path of the curve after it reaches its maximum value at t_1. For thickness smaller than this, the fracture toughness begins to decrease again due to the volume of material available for plastic deformation decreasing as well. In other words, t_1 represents the thickness at which the size of the naturally developed plastic zone is equal to the thickness of the specimen, corresponding to the maximum possible amount of energy absorption. As the dimensions of the specimen decrease from there, the size of the plastic zone will be limited by those dimensions, thereby limiting the amount of energy that can be dissipated through plasticity. This equates to a measurable decrease in fracture toughness due solely to specimen geometry. Kang *et al.*[45] characterized this trend experimentally in Cu foils ranging from 20-1000 μm in thickness. The results of this study are depicted in Fig. 18. This plot shows that the fracture toughness—J_c in this case—has a maximum value at ~0.3 mm (30 μm) and decreases almost linearly towards zero with decreasing thickness.

Based on this plot, two very important conclusions can be drawn. First, that the stresses required to cause fracture in small-scale load-bearing members, such as in micro-electro-mechanical systems (MEMS), might be significantly lower than would be expected based on bulk toughness values simply due to the size scale of such devices. While this is certainly an important observation, it really has no effect on the use of small-scale testing to study grain boundary embrittlement. However, the second conclusion is that a direct comparison between toughness values measured from small-scale specimens and values measured from bulk-scale tests cannot be reasonably made for materials that exhibit any appreciable ductility. Hosokawa *et al.*[43] attributed their extremely low toughness values to changes in deformation mechanisms at small-scales such (i.e. dislocation starvation); however, it seems that the values could just as easily explained by this continuum-based plasticity argument as well. One thing to note is that the toughness values of Cu-Bi boundaries tested using the micro-cantilever approach by Armstrong *et al.*[34,35] did show good agreement with bulk values. This is likely due to the size of their specimens and the fact that the stress state in bending is non-uniform through the beam, reducing the size of the natural plastic zone. This topic will be discussed in significantly more detail in a later chapter as a basis for comparison to the results obtained in the experiments presented in this document.

3. EXPERIMENTAL PROCEDURE

This section will outline the steps that were taken to carry out the experiments conducted in this study from start to finish. The results of these experiments will be presented and discussed in the following chapters.

3.1 Bulk polycrystalline Cu specimen preparation

It was the original intention of this work to measure the toughness of random grain boundaries in polycrystalline Cu (as was done in[34,35]). However, during preliminary testing it became clear that this path was not as feasible as was originally hoped for. The following sections will describe the process of fabricating these specimens as well as the initial characterization techniques, the results of which made it clear that a departure from the original experimental plan was necessary.

3.1.1 Creation of Cu-Bi alloy

Before small-scale test specimens of individual Bi-doped grain boundaries could be fabricated, a bulk-scale, doped polycrystalline sample needed to be created. To do this, 3-4” sections of 1/4”-diameter high-purity (99.99%) oxygen-free high-conductivity (OFHC) Cu rods were submerged in molten Bi at just above its melting point (271 ˚C) for several hours. Because the rods were completely submerged in liquid Bi and the temperature was relatively low, appreciable oxidation of the Cu rod was not observed. After being removed from the Bi bath and allowed to air cool, the rods were fully encrusted in solid Bi. They were then individually encapsulated in evacuated quartz tubes as shown in Fig. 19 to prevent oxidation during subsequent heat treatments. The heat

treatment schedule used consisted of two parts: a 24-hour hold at 900˚C followed by a 24-hour hold at 500˚C. These temperatures were specifically chosen based on the temperature-dependent solubility of Bi in Cu determined by Voce and Hallowes[2]. The purpose of the first step was to create a saturated solid solution of Bi in Cu. The solubility of Bi in Cu increases rapidly between 600 and 800˚C, so by holding for an extended period of time above this range to allow for diffusion to occur, a significant amount of Bi was introduced into the rod. Upon lowering the temperature to 500˚C, the reduction in solubility provides a thermodynamic driving force that causes the Bi atoms to diffuse out of the Cu lattice to more energetically favorable sites, namely grain boundaries (and the surface to some extent). Following this second step, the glass tubes were submerged in cold water, causing the glass to break and quench the Cu rods, thereby preserving the segregated microstructure.

Unfortunately, it was observed that during this heat treatment schedule, the Cu rods appeared to partially melt (likely localized melting at GBs due to the presence of low melting point Bi) and flow such that the final rod shape conformed to that of the glass tube. Porosity was also seen on the surface of the rods, limiting the volume of useful material for further processing.

3.1.2 Metallographic preparation and SEM analysis

Following heat treatment, the Cu-Bi rods were sectioned using a low-speed diamond blade saw and mounted in either Bakelite, epoxy, or Al-filled conducting epoxy. (after several trial runs, it was determined that Bakelite provided the best results). The mounted specimens were then metallographically polished down to 1200 grit SiC

grinding paper followed by 24 hours of vibropolishing in 0.05 μm colloidal $Si0_2$. Initial observation using light optical microscopy (LOM) revealed little information regarding the microstructure of the rods, so SEM-based analysis techniques were necessary. Prior to this, specimens were lightly coated (<5 nm) with Ir so that the mount material did not create significant charging effects in the SEM.

Initial observation of the specimens using standard SEM imaging in a Hitachi 4300SE/N SEM revealed very little microstructural information either, as the polished surface was nearly featureless. However, the grain structure was easily revealed by electron backscattered diffraction (EBSD) analysis, as seen in Fig. 20. This representative image shows that the rods had a large grain size (several 100s of μm and up) as well as a number of annealing twins. Neither of these features is surprising given the heat treatment schedule that was used. The large grain size was ideal for this project, as the boundaries of large grains tend to be much flatter and straighter than those of small grains. However, the twin boundaries must be avoided during fabrication of mechanical test specimens, as it is well documented that Bi does not segregate to twin boundaries[14]. EDS was then used in an effort to determine if there was a detectable amount of Bi in the specimen and where it was located if it was there. Fig. 21 shows a series of images from this analysis. The image in (a) shows a backscattered electron (BSE) image of a group of triple point junctions surrounding a relatively small grain. Contrast in BSE images is due solely to differences in atomic number, so it was believed that the light areas contained large amounts of Bi. This was confirmed by the EDS maps shown in (b) and (c) showing the location of Cu and Bi in the specimen, respectively. As expected, the Cu grains

contain an undetectable amount of Bi and the second-phase Bi located at the triple points contains an undetectable amount of Cu. Unfortunately, from this image it is not possible to tell if any of the grain boundaries contain Bi.

3.1.3 Ion channeling imaging

Following the SEM-based analysis techniques described above, the sample was imaged using the ion beam on an FEI Strata DB 235. Using an ion beam (Ga^+) rather than an electron beam allows for much greater contrast to be seen between different grains due to the differences in relative orientation. Furthermore, the ion beam can be used to remove a selected area of material so that the 3-D microstructure can be imaged, as seen in Fig. 22. From this image, it is clear that despite the boundary's straight appearance on the surface of the sample, it is highly inclined beneath the surface. Multiple boundaries were examined from multiple Cu rods and this inclination was typical, regardless of grain size or boundary appearance on the surface. As discussed in the previous chapter, it is highly desirable for the boundary to run perpendicular to the eventual loading axis of a test specimen. While a small amount of boundary inclination beneath the surface could be tolerated and accounted for during later fabrication steps, the large inclination angles that were observed to be typical could not be tolerated. This was the primary reason for abandoning the plan to use polycrystalline Cu as the bulk material from which small-scale test specimens would be fabricated. Instead, it was decided to use prefabricated bicrystals with a defined misorientation because proper alignment of the grain boundary is nearly guaranteed.

3.2 Bulk bicrystal specimen preparation

Three different bicrystals were used in this work, all of which were [001] twist boundaries with different misorientation angles: 6, 13, and 33˚. Unfortunately, the origin of these bicrystals is unknown, as is the fabrication method used to create them. The following sections will describe the steps that were taken to dope sections of these bicrystals with Bi and then prepare and characterize bulk-scale samples containing the boundary.

3.2.1 Bi-doping of bicrystals

Due to the significantly smaller size of the prefabricated bicrystals compared to the polycrystalline Cu rods, a different procedure for introducing Bi into the samples needed to be developed. First, the bicrystals were sectioned using a low-speed saw into segments between 3 and 5 mm in length, with the boundary running down the middle. Half of these segments from each bicrystal were set aside and left pure, while the rest were doped with Bi. To perform this doping, a small pellet of Bi was placed on top of each bicrystal segment prior to being placed in an alumina boat. An alumina crucible was placed upside-down over the specimens as well in order to prevent any Bi vapor from escaping and contaminating the furnace tube. This entire assembly was then placed in the center of an alumina furnace tube, which was then evacuated and backfilled with Ar several times in order to ensure a very low oxygen partial pressure in the tube. After these cycles, the tube was filled with a positive pressure of Ar and then heated to 600˚C for 72 hours. This temperature was chosen because it is high enough for diffusion of the Bi into the specimen to occur, but low enough to prevent the localized boundary melting that was

observed in the polycrystalline rods. After 72 hours, the specimens were allowed to furnace cool so that segregation of Bi to the boundary could continue during the ramp down.

3.2.2 Metallographic preparation and SEM analysis

Following the doping procedure, one segment from each of the doped bicrystals as well as one of the corresponding pure bicrystals were mounted in Bakelite and metallographically prepared using the same procedure described above for the polycrystalline rods (including a light Ir coating). Following this prep work, EBSD was used to confirm the character of each grain boundary (misorientation angle, twist axis, etc.). EDS was not performed in the SEM because it was known from the polycrystalline specimens that no Bi signal could be detected from a grain boundary. In order to determine the Bi concentration at the boundary, a much higher resolution technique needed to be used, as will be discussed later.

3.3 Notched micro-tensile specimen fabrication

Following the initial characterization described above, FIB machining was used to fabricate notched micro-tensile specimens containing the boundary from each of the six bicrystals (3 misorientation angles, with pure and Bi-doped conditions for each). The following sections describe the procedure for fabricating these specimens, as well as the details of which type of test specimen was fabricated from each bicrystal.

3.3.1 Ion-beam imaging of boundary and initial FIB milling

Identical to the procedure used on the polycrystalline rods, the ion beam in the FIB was used to locate and image the grain boundary on the polished surface of the bicrystal. Once the location of the boundary was determined, the process of fabricating mechanical test specimens began by depositing a protective Pt layer ~50 μm long x 3.5 μm wide x 3 μm thick across and perpendicular to the boundary, similar to that shown in Fig. 23. Following this, an ion beam current of ~7 nA was used to mill out large rectangular areas ~50 μm long x 15 μm wide x 12 μm deep adjacent to both sides of this Pt strip. After this rough milling step, each vertical face of specimen was cleaned up using a beam current of ~1 nA, leaving a specimen that has nearly parallel sides and was typically ~2 μm thick. Fig. 24 shows an I-beam image of a specimen at this point in the process. In this image, it is clear that the grain boundary runs perpendicular to the top surface of the sample, as expected.

In order to minimize the chances of any composition variation between specimens taken from the same boundary (due to a pre-existing concentration gradient, for example), subsequent mechanical test specimens as well as (S)TEM specimens for chemical analysis were fabricated as close as possible to the previous specimen location. To do this, as well as reduce the amount of time needed on the FIB, the back-side of the large trenches were used as the front-side of the next specimen, as shown in Fig. 25. This I-beam image shows the placement of the Pt strip for the next specimen right on the back edge of the previous specimen's trench. This trend was continued for multiple specimens, as shown in Fig. 26.

3.3.2 Extraction of specimen from bulk; defining thickness and width of test specimen

While still attached to the bulk, a beam current of 500 pA was used to mill a "J-shaped" cut into of the vertical faces of the specimen. This cut was designed to completely free the specimen from the bulk except for one small tab, which was left intact. Next, a tungsten plucker needle was inserted and brought into contact with the free end of the specimen and Pt-tacked into place. The remaining connection with the bulk was then severed, leaving the specimen completely detached from the bulk and attached to the plucker needle, as shown in Fig. 27. The specimen was then attached to a Cu grid and the plucker needle was cut free, as shown in Fig. 28.

In order to define the thickness of the specimen, it was tilted so that the ion beam was pointing at the specimen from directly above. Starting at ~500 pA and decreasing down to ~100 pA, progressively smaller beam currents were used to thin the specimen from both sides until the desired thickness of ~1 μm was reached. However, if it appeared that further milling might cause irreparable damage to the specimen, slightly larger thicknesses (no greater than ~1.5 μm) were acceptable. Fig. 29 shows an image of a specimen after this thinning process. This type of image was taken for every specimen fabricated and was used to determine the individual thickness of each one.

Once the desired thickness had been reached, the entire grid was tilted 90˚ so that the face of the specimen was oriented normal to the ion beam. The specimen was also rotated to that the boundary was perfectly vertical. Then, an ion beam current of 300 pA was used to mill away material so that a rectangle with the desired width (~6 μm) was

left behind, as shown in Fig. 30. Again, this type of image was taken of every specimen and used to measure the actual width of each.

3.3.3 Attaching specimens to test device and final fabrication steps

After defining both the thickness and width of a test specimen, the plucker needle was once again attached to the specimen (on the free end) and the specimen was cut free from the Cu grid. The specimen was then carefully placed on the testing device, which will be described in more detail later. One in the proper location, as shown in Fig. 31, the free end of the specimen was Pt-tacked into place on the device. The plucker needle was then cut free from the other end and removed, allowing that side to be tacked down as well. Further Pt was deposited at a variety of rotation and tilt angles in order to ensure that the specimen was firmly attached to the test device, as shown in Fig. 32. Although not an important value for any calculations, the length of the test specimen is defined as the distance between the Pt-tacks on either end, and was typically ~15-20 μm.

Once the specimen was firmly tacked into place, the stage was tilted so that the device (and specimen) were perpendicular to the ion beam. Pt circles were then deposited on the surface of the sample using a low beam current (10 pA, to minimize damage) to act as markers for strain measurement using digital image correlation (DIC), which will be discussed later. Next, the specimens were notched at the grain boundary by a two-step milling process. First, a 10 pA beam current was used to mill a notch on the edge of the specimen at the boundary ~1 μm long. Next, a 1 pA current was used to extend the notch by ~0.5 μm, making the total notch length ~1.5 μm, ~25% of the specimen width. Fig. 33 shows an I-beam image taken of a specimen after this notch has been created (NOTE:

this image shows a specimen without Pt markers, as this technique had not been adopted when this image was taken). For double edge-notched tensile (DENT) specimens, this procedure was repeated on the other side of the boundary, creating a specimen like the one shown in Fig. 34. The specimen is now finished and ready to be tested; the testing procedure will be described in the following section.

3.4 Un-notched single crystal specimen fabrication

In order to verify that the testing technique was working properly, an un-notched single-crystal specimen with a known orientation (loading axis of <001>) was fabricated and tested using the same procedure used for the notched bicrystal specimens, as described below. From this test, a measurement of the yield strength of the material would be made as well, which would later be used as a material input in a finite element model (FEM). This single-crystal specimen was fabricated using a similar procedure as described above, with two major differences. The first, as mentioned already, is that it no notches were introduced. This was done so that no stress concentrators were present that would affect the results of the test. The second is that a slightly different geometry needed to be used in order to ensure that both yielding and eventual failure occurred in between the Pt markers on the specimen. Therefore, a bowtie-shaped specimen, shown in Fig. 35 was used rather than the simple rectangle used for the notched beams.

3.5 *In-situ* micro-tensile testing

All mechanical tests conducted in this work were performed *in-situ* in an SEM (either the FEI Strata DB235 FIB or an FEI XL30 ESEM; the FIB was preferred due to better image quality). Testing was performed using a Hysitron, Inc. PI-85

nanoindentation system in conjunction with their push-to-pull (PTP) devices (these are the "test devices" mentioned above). The following sections describe the equipment used as well as the steps taken to set up, conduct, and analyze the results of a test.

3.4.1 PI-85 nanoindenter and PTP devices

The PI-85 system consists of two primary components: the load cell/transducer and the stage motor stack. The first of these components controls the indenter tip itself and is used to not only drive the tip forward during a test, but also sense the load being applied against the tip. After proper calibration of the transducer, this allows for both indentation load and depth to be calculated simultaneously. The second of these components is the x-y-z positioning system that moves the sample around relative to the stationary tip. This allows for precise positioning of where the indenter tip will make contact with the sample, a necessary feature for the testing procedure used here. Unfortunately, having these motors in-line with the specimen does add some compliance to the overall system. However, through proper calibration this effect can be easily accounted for.

The PTP devices used in this work allow the compressive force applied by the indenter tip to be converted into a tensile load on the specimen. This device, shown in Fig. 36, is a fabricated from a silicon-on-insulator (SOI) wafer and consists of a moving platform connected to the rest of the wafer by 4 hinges. This image was taken just prior to the start of a test, so it shows a specimen attached as well as the indenter tip just out of contact with the device. During a test, the tip will advance until it makes contact with the semi-circular pad on the left edge of the device. Then, as the tip pushes against the

device, the movable platform (which contains the contact pad and curves around to connect to the right end of the specimen in this image) will move to the right while the fixed portion (everything else, including the "J-shaped" piece attached to the left end of the specimen) will not. This applies a tensile load to the specimen that is measured by the indenter's transducer. Because the hinges that connect these two platforms have some stiffness associated with them, they can be thought of as springs in parallel with the specimen, which means that a portion of the load applied by the indenter tip is applied to these hinges, rather than the specimen. Therefore, the stiffness of these hinges must be accounted for in order to accurately calculate the applied load on the sample alone. This stiffness can either be measured before the specimen is attached or after it has fractured.

3.4.2 Pre-test setup

Prior to conducting a test, the PTP device (with finished sample already attached) was adhered to an SEM stub with a vertical ledge using cyanoacrylate. This stub was then loaded into the indenter so that the PTP device was face up and the contact pad was facing the indenter tip. The assembly was then loaded into the SEM where, after pumping down, the electron beam was turned on allowing the tip and PTP device to be imaged. The x-y-z motors on the indenter were then used to position the device just out of contact with the indenter tip, as shown in Fig. 36.

3.4.3 Testing Procedure

All tests were conducted in load-control mode using the load function shown in Fig. 37 (or a very similar one). This plot shows that loading increments of 50 μN (later this was decreased to 25 μN) were separated by 25-second hold periods, during which a

high-quality SEM image of the specimen could be captured. This sequence was continued until the specimen fractured, at which point a much longer hold (~3-5 minutes) was built in to the load sequence so that a series of very high-quality images of the fracture morphology could be taken.

3.4.4 Determination of stress and strain

As previously mentioned, determining the tensile load on the specimen is relatively easy as it is simply the load measured by the indenter minus the component applied to the PTP device itself. The applied stress is simply this load divided by the gross (i.e. un-notched) cross-sectional area. However, accurately determining the extension (strain) of the specimen required the use of DIC. A software program called ImageCorr (provided by Dave Read and Nick Barbosa from NIST-Boulder) was used in this capacity to track the movement of the Pt markers deposited on the surface of the specimen. By measuring the change in distance between the markers on either side of the notch between each of the images taken during the test, the engineering strain could be calculated and paired up with the applied stress for each acquired image.

4. RESULTS AND DISCUSSION

4.1 EBSD analysis of bicrystals

In order to confirm the character of each of the bicrystals used in this work, EBSD analysis was performed. Fig. 38 shows an EBSD map of the 33˚ grain boundary. This image shows that the boundary is extremely straight, which is confirmed by ion-channeling images taken during FIB milling of test specimens. Figs. 39-41 show the pole figures generated from EBSD maps taken of the 6˚, 13˚, and 33˚ boundaries, respectively. These images prove that the two grains share one common crystallographic direction (near the <001>), which corresponds to the twist axis. The misorientation angle was calculated by measuring the angular difference between the other points on the pole figures. This analysis confirmed the misorientation of each of the bicrystals to be as expected.

4.2 SENT testing of 13˚ boundary

The first mechanical tests conducted were SENT tests on the pure and Bi-doped 13˚ boundaries. The results of these tests will be discussed in the following sections. It is important to keep in mind that these specimens did not have Pt markers on the surface, so DIC was not used for strain measurement. Instead, the displacement measured by the indenter's transducer was used, which is similar to using the crosshead displacement from a standard lab-scale tensile test. The impact of this on the results will be discussed as well.

4.2.1 Discussion of test results

Tests were conducted on two pure and two doped specimens and the resulting load-displacement and stress-strain curves are shown in Figs. 42 and 43, respectively. There are a couple of important features of these curves that need to be noted. First, all four curves have a distinct, non-linear segment at the beginning indicative of Hertzian contact loading. This makes sense as the indenter tip used was cono-spherical (radius of hemisphere on end ~1 μm). Furthermore, the slopes of the linear regions are dramatically different from one curve to another, ranging from ~5.5 to 23 GPa. These values are well below the Young's modulus of Cu in this orientation (E_{100} = 66.7 GPa[44]). The presence of the notch will lower the effective stiffness of the specimen, but not by enough to account for the discrepancy in these tests. Therefore, there must be an inaccuracy in either the load or displacement in order to explain these values. The load measurement is unlikely to be incorrect, as the specimen can be thought of as a spring in series with the load transducer, so the load measured by the transducer will be the same as the load applied to the specimen. It is more likely that the displacement measured by the transducer is not an accurate measurement of the actual extension of the specimen. In order for this measurement to be truly accurate, there must be zero displacement in any of the components of the system other than the specimen itself. There are two places where this unlikely to be the case: the contact point between the indenter tip and the PTP device, and the Pt tacks that hold the specimen in place on the device. As discussed previously, there is evidence that suggests that the contact between the indenter and PTP device can affect the measured load-displacement behavior. However, the fact that the curves are still

linear suggests that this is not a large effect in this case. The more likely source of additional compliance is the Pt tacking as the quality of FIB-assisted Pt deposition is known to be quite poor, containing as little as 25% Pt[46]. It is therefore not surprising that there would be a substantial amount of compliance in the Pt tacks, causing the displacement measured by the indenter's transducer to be larger than the actual extension of the specimen. Furthermore, variations in the Pt tack stiffness from specimen to specimen could be large, leading to the observed differences in the apparent stiffness values. The behavior of the Pt tacks served as justification for using DIC to measure extension and strain directly from the specimen in subsequent tests.

4.2.2 SEM imaging of fracture morphology

Figs. 44 and 45 show post-mortem SEM images of a pure and doped specimen from these tests. These images show a distinct difference in the fracture morphology between the two specimens. The most obvious difference between the two is the increased evidence of plasticity in the pure specimens. This evidence includes slip traces on the surface and the "necked" appearance of the un-notched ligament. The surface of the doped specimen has significantly fewer features on its surface, suggesting that less plasticity occurred prior to fracture. The stress-strain curves shown in Fig. 43 show that the pure specimens exhibited more strain to failure, but mostly due to the variation in slope discussed above. Furthermore, the fracture path on the doped specimen is straighter and much closer to following the grain boundary than on the pure specimen. This shift from transgranular towards intergranular fracture due to boundary embrittlement is consistent with bulk scale tests[29,31].

4.2.3 Calculation of fracture toughness

Finally, a fracture toughness (K_C) value was calculated for each test using the following equation[47]:

$$K_C = \sigma_f \sqrt{\pi a}\left(1.122 - 0.231\left(a/b\right) + 10.550\left(a/b\right)^2 - 21.710\left(a/b\right)^3 + 30.382\left(a/b\right)^4\right) \quad (4)$$

where σ_f is the gross section stress at fracture, a is the notch length and b is the specimen width. The calculated values, summarized in Table 1, show that there is a decrease in toughness of ~48% in the doped specimens compared to the pure specimens. This is consistent with the difference in the degree of plasticity seen in the post-mortem fracture images. It must be noted that because these values are averages of only two tests for each specimen type (pure/doped), the standard deviation can be quite large, as seen in the pure specimen value. However, despite this large error, the observed embrittlement in this boundary is likely real when combined with the fracture images and the stress-strain curves.

4.2.4 Further discussion of results and impacts on future tests

Clear evidence of grain boundary embrittlement was observed in the 13˚ grain boundary, supported by both the calculated fracture toughness as well as the fracture morphology seen in post-mortem SEM images. However, the degree of embrittlement was significantly larger than expected based on the results of Li and Zhang[31] shown in Fig. 12, which suggests that a boundary with a misorientation angle of 13˚ should show little to no embrittlement. However, it must be noted that Li and Zhang tested [001] tilt boundaries and the boundaries tested in this work are [001] twist. The biggest impact this

difference will have is on the orientation of active slip systems and their corresponding Schmid factors which, in turn, affect the energy required for dislocation emission from the crack tip, G_{disl}, as discussed in a previous chapter. This difference between twist and tilt grain boundaries may shift the transition angle at which embrittlement starts to occur. If this angle were lower in twist boundaries, it may be entirely reasonable to see embrittlement in a 13˚ boundary. In fact, because the fracture morphology in the doped specimens was not pure intergranular fracture, but rather a mix of inter- and transgranular, it may be possible that 13˚ falls somewhere in the transition region, which would further complicate things. With that in mind, it was decided not to conduct any more tests on the 13˚ boundary and to focus more on the 6˚ and 33˚ boundaries, since these represent the most extreme cases and offer the best chance to see a dramatic difference in the amount of embrittlement.

Furthermore, the SENT specimen geometry does not provide any constraint on the fracture path after the crack initiates at the notch tip. As expected, this means that the pure specimens, which have no driving force to fracture along the boundary, exhibited transgranular fracture. Based on the results from the 13˚ boundary, it was expected that the high angle (33˚) boundary would exhibit intergranular fracture when doped and transgranular when pure. Because one of the primary objectives of this work was to experimentally quantify embrittlement for a set of boundaries, it would be extremely advantageous for all specimens tested to fracture along the boundary so that the toughness values were all calculated for the same type of fracture. To that end, it was decided to use a DENT specimen geometry on all subsequent tests because the constraint

provided by the second notch increases the likelihood of intergranular fracture, even in samples that might not otherwise do so. The DENT geometry also eliminates the bending moment that is inherent to the SENT geometry, simplifying the analysis of test results.

4.3 DENT testing of 6˚ boundary

DENT tests were conducted on specimens containing the 6˚ boundary in both pure and Bi-doped conditions. These specimens were marked for DIC during fabrication, so all displacement and strain values reported were generated using this technique. The results of these tests will be reported and discussed in the following sections.

4.3.1 Discussion of test results

Fig. 46 shows a representative stress-strain curve generated from these DENT tests on the 6˚ bicrystal in both pure and doped states. In this plot, each data point corresponds to an image that was taken during each load hold segment during testing. The displacement of the Pt markers in each image was determined using DIC software and then paired with the known load for each image to generate the full curve. This procedure was carried out for every test. The first thing to note about these curves is that their overall shape appears much cleaner and more akin to a typical stress-strain curve from a tensile test. There is a clear linear elastic region at the beginning of the test with much more realistic and relatively comparable slopes, as shown in Figs. 47 and 48 for the pure and doped specimens, respectively. The discrepancy between these two slopes (44 vs. 65 GPa) would likely be significantly reduced by averaging over many tests. Unfortunately, due to the nature of small-scale mechanical testing, generating statistically large sample sizes is difficult and such discrepancies in elastic modulus are quite

common. However, these values do compare relatively well with the results from FEM simulations (will be discussed later), proving that the DIC technique works correctly.

Another point that should be made about these curves is the apparent difference in yield strength, σ_y, between the doped and pure specimens. This discrepancy could come from a number of different sources including, but not limited to: differences in notch root radius, differences in the ratio of *a/w*, differences in crystallographic alignment, or an actual decrease in G_{disl} due to the presence of Bi on the boundary. The first few of these possibilities all deal with small variations in the fabrication procedure from one specimen to the next, which are certainly possible given that each specimen is individually fabricated and that the FIB-steps are essentially manually controlled. Furthermore, while it has been suggested in the literature that Bi segregated to a boundary could lower G_{disl}[29], it has never been experimentally observed. Therefore, it is not possible to draw any reliable conclusions about this behavior from the current experiments. As such, this discrepancy will be not be discussed in any further detail until suggestions for future work are made towards the end of this manuscript.

4.3.2 SEM imaging of fracture morphology

Figs. 49 and 50 show post-mortem SEM images of pure and doped specimens, respectively, that are representative of all tests conducted on similar specimens. These images show a very similar fracture morphology in both specimen types, despite the apparent difference in the stress-strain curves as discussed above. The fractures were both transgranular and have a zig-zag, shear-like appearance. At first glance, the presence of clear slip steps on the surface agrees with the amount of plasticity seen in the stress-strain

curves. However, the last images taken during testing of these specimens, which correspond to the last data points in the stress-strain curves (shown in Fig. 51 for a pure specimen), do not show any sign of these slip traces. This means that the massive plasticity that can be seen in the post-mortem images occurred very rapidly during the fracture process and not continuously over several load intervals. Ultimately, this is the biggest drawback to using a series of still images to make strain measurements, as it is impossible to know the actual strain at fracture. Knowing the actual fracture load from the transducer allows an estimate to be made by fitting a curve to the data and extrapolating it beyond the last point. However, it is very clear that the deformation behavior immediately before and during the fracture event is quite different than it is up to that point, so this extrapolation is, at best, a lower bound on the actual strain at fracture.

Despite this, these slip steps, in conjunction with the crack path, do provide some insight into the fracture mechanism. For example, a number of these traces appear to originate at the notch tips, particularly in the pure specimen (Fig. 49). This makes some sense given that the stress is largest directly ahead of these notches, leading to a larger number of dislocations being generated and emitted from the boundary in this region. Once generated, these dislocations progress through the crystal along a specific slip plane until they reach the surface, where they generate a slip step. The steps seen in the post-mortem images shown here are likely due to a number of identical dislocations emitted from the same source that propagated along the same slip system and combined to create a large slip step on the surface. The fact that there are likely to be multiple active slip

systems (due to a combination of crystal structure and orientation) that intersect with one another suggests that localized shear thinning was ultimately responsible for the failure. By this mechanism, the failure would occur at the intersection point, which would be midway between the boundary (where the dislocations originated) and the slip steps on the surface (where they terminated). The zig-zag shape of the crack path could therefore be interpreted as localized thinning at the intersection of different sets of slip systems. Unfortunately, it is difficult to prove this theory based solely on the experiments conducted here, as the actual stress and strain distributions near the notch tips are unknown. However, FEM analysis can provide some insight into these details, as shall be discussed in more detail in section 4.7.

4.3.3 Calculation of fracture toughness

As with the SENT specimens, a K_C value was calculated for each test conducted. For DENT specimens, the equation used was[47]:

$$K_C = \sigma_f \sqrt{\pi a} \left(\frac{1.122 - 0.561\left(a/b\right) - 0.205\left(a/b\right)^2 + 0.471\left(a/b\right)^3 - 0.190\left(a/b\right)^4}{\sqrt{1 - a/b}} \right) \qquad (5)$$

where σ_f, a, and b are the same quantities as they were in Eq. 4. Table 2 reports the average toughness value and standard deviation for each specimen type. These values suggest that the doped specimens were embrittled (~14% decrease in K_C), implying that there were Bi atoms segregated to the boundary. This conclusion is consistent with the experimental stress-strain curves, which show a lower fracture stress and suggest a lower fracture strain. However, it is not consistent with the post-mortem SEM images as the transgranular shear failure that both specimen types consistently showed would likely be

unaffected by the presence of Bi on the boundary, if any is even there at all (Fraczkiewicz and Biscondi showed that low angle grain boundaries like this were unlikely to contain a measurable amount of Bi[9]). Some preliminary AEM results suggest that this may be the case for this particular boundary, but more work is needed to be sure.

With all of this in mind, it seems most likely that this boundary is not embrittled and that the discrepancy in toughness values is due to the limited number of specimens tested. The values listed in Table 2 show that the average value for the doped specimen falls within the range of the pure value minus the standard deviation. It is therefore believed that more testing on both specimens would be likely to bring the averages closer together, eliminating any confusion. Unfortunately, such a significant commitment to testing only one specimen type has not yet been undertaken.

4.3.4 Comparison with 13˚ boundary results

Taking a closer look at the values in Table 1, a similar argument as the one mentioned above could be made regarding the possible embrittlement of the 13˚ boundary. However, unlike the 6˚ specimens, the fracture morphologies of the 13˚ specimens do actually appear slightly different, suggesting that the segregation behavior of each boundary is also different.

It must be noted that the magnitude of these toughness values is significantly lower than those measured via SENT testing of the 13˚ boundary. For the pure specimens, there should be no difference between the two boundaries (the doped specimens must be ignored for now as the embrittlement could be different in each). Therefore, this difference is almost certainly a size effect caused by the second notch

further limiting the volume of the plastic zone, as previously discussed. In the SENT specimen geometry, the plastic zone grows outward from the notch tip and can grow as large as the entire specimen width (~6 μm) minus the notch length (~2 μm, leaving 4 μm). However, in the DENT geometry, two separate plastic zones grow independently from each notch until they eventually meet in the center of the specimen. In this case, the radius of each plastic zone can be no larger than the distance from the centerline of the specimen to the tip of each notch (~1.5 μm). Even if both notches are taken into account, the volume of material contained in the plastic zone of a DENT specimen is less than that of a SENT specimen, leading to a decrease in the measured fracture toughness.

4.4 DENT testing of 33˚ boundary

4.4.1 Discussion of test results

Fig. 52 shows representative stress-strain curves generated from DENT testing of the 33˚ boundary (analogous to the curves in Fig. 46 for the 6˚ boundary). Again, these curves show a similar elastic slope for both curves, an apparent drop in yield strength for the doped specimen, and a lower fracture stress for the doped specimen. However, it appears that there is a more substantial difference between these two curves than there was for the 6˚ specimens. This suggests that there may be more embrittlement of this particular boundary, as expected. This observation will be revisited in more detail in the following sections.

4.4.2 SEM imaging of fracture morphology

Figs. 53 and 54 show post-testing SEM images of a 33˚ pure and doped specimen, respectively. Unlike the previously discussed pairs of similar images, there is a dramatic difference between these two images. First and foremost, the fracture morphology in the pure specimen is similar in nature to those shown for the 6˚ specimens (both pure and doped, with slightly smaller zig-zag features (likely a crystallographic effect). This is an expected result, as all pure boundaries will fail in a ductile fashion (6˚ doped likely contains little to no Bi, so it is essentially pure as well). However, the doped specimen exhibited pure intergranular fracture with significantly less evidence of plasticity (slip steps) than any other specimen type. This observation agrees with the significantly lower strain to failure suggested by the doped curve in Fig. 52 (remember, the actual strain at failure is unknown).

4.4.3 Calculation of fracture toughness

Eq. 5 was again used to calculate the toughness of these specimens and the values are reported in Table 3. Looking at this table, the first thing to note is that the toughness value of the 33˚ pure specimens is the same as the 6˚ pure value (shown in Table 2). This makes sense based on the similar stress-strain curves and fracture morphologies exhibited by these specimen types. The next important thing to note is the clear drop (~40%) in the calculated toughness for the doped specimen. Even though the error is rather large (~33%), there is no overlap in the range of values with the pure specimens. Combining this with the clear shift in fracture morphology provides irrefutable evidence of boundary

embrittlement in this boundary (NOTE: preliminary AEM work has detected the presence of Bi on this boundary, further solidifying this conclusion).

4.5 Further discussion of testing results and comparison with literature

4.5.1 Effect of misorientation angle on embrittlement

Both Li and Zhang[31] and Fraczkiewicz and Biscondi[9] found that there was a critical misorientation angle of ~20-25˚ below which neither boundary segregation nor embrittlement would occur in <001> tilt boundaries. This angle is likely linked to the grain boundary energy, which is shown in Fig. 56. This plot shows that the GB energy has a very broad maximum value between ~25˚ and 65˚ with a significant drop off outside of that range. A similar plot for <001> twist boundaries (like those studied here) is shown in Fig. 57[48], which shows a similar behavior, but with a lower maximum energy. This is in direct agreement with the observed difference between the 6˚ and 33˚ specimens here (33˚ lies above the critical angle, 6˚ lies below it). However, it does not explain the behavior of the 13˚ specimen as easily. It is possible that instead of a single critical angle, there is a range over which the transition gradually occurs. If this were the case, 13˚ may lie in this transition region, so some embrittlement would still be expected. It must be noted that the results presented above may be misleading on this front, as it would appear that the 13˚ boundary experienced more embrittlement that the 33˚ boundary (48% vs 40% decrease in toughness). However, the further limitation on plasticity in the DENT geometry is likely responsible for this. As previously discussed, by confining the plastic zone between two notches instead of only one, the ability for the pure specimen to dissipate energy through dislocation nucleation and motion is limited

and the toughness goes down. This will also affect the doped specimen as well, but on a much smaller scale. This argument can be expanded to explain the difference in behavior between these tests and the bulk-scale tests by Li and Zhang[31]. These authors showed a much larger difference in the fracture strength of pure and doped boundaries (~80%). This suggests that there is clearly a trend between specimen size (which controls the amount of energy absorbed via plastic deformation) and the observed difference in fracture behavior between pure and doped GBs. It is therefore likely that if DENT tests were conducted on the 13˚ boundary, the drop in toughness would be measurable, but would be less than 40%, depending on what the threshold angle actually is.

4.5.2 Comparison with Cu-Bi studies using notched micro-cantilever testing

As mentioned previously, Armstrong *et al.*[34,35] have conducted the only other studies of Cu-Bi embrittlement using small-scale mechanical testing. These authors used a FIB-machined micro-cantilever approach to measure the toughness of a number of random grain boundaries in Bi-doped polycrystalline Cu. Toughness values ranging from 2.7-7.2 $MPa \cdot m^{1/2}$ were calculated, with no apparent correlation between toughness and misorientation angle or GB plane. Also, while there were no intentional attempts to test pure GBs, a number of tests were performed on GBs that turned out to contain no measurable Bi, similar to the 6˚ "doped" specimens used here. However, due to the nature of the micro-cantilever test, these pure boundaries could not be broken due to the large amount of plasticity that they exhibited. Given that this work is by far the most direct comparison for the work presented here, it warrants a detailed comparison between the results.

First off, the values of toughness that were calculated for embrittled boundaries using cantilever tests were significantly larger than those measured here. Given that both studies observed embrittlement, that aspect of things will be ignored for now. However, the one thing that cannot be ignored is the size of the specimens used in each. As mentioned several times already, the fracture toughness of small-scale samples is heavily dependent on the specimen dimensions. As shown in Fig. 58, the dimensions of the cantilevers used were much larger than the DENT specimens used here. The thickness of a DENT specimen (~1 μm) would correspond to the width of a cantilever (~5 μm) and the un-notched ligament width of a DENT specimen (~3 μm) would correspond to the thickness of a cantilever (~5-6 μm). With only these dimensions in mind, even if identical specimens were tested in each study, the toughness measured using the cantilever approach would likely be much larger than that measured by DENT testing.

However, the specimen dimensions are not the only difference between the two tests that will affect the toughness value. In the DENT specimens tested here, the toughness values do not compare to bulk values because the dimensions of the specimen limit the size of the "natural" plastic zone. This zone grows out from the notch tips and eventually encompasses the entire un-notched ligament. However, because the cantilever approach loads the specimen in bending, the plastic zone is limited by a combination of the specimen dimensions and the stress gradient in the beam. In bending, the stress in the beam will drop to zero at the centerline of the beam and go compressive on the bottom half. This means that the plastic zone is inherently confined to the top half of the beam only (less than that, in fact, because the stress will be below the yield strength for some

distance away from the centerline). Therefore, the specimen dimensions will have an even smaller role impact on the size of the plastic zone, which can grow relatively unimpeded to its "natural" size. This is the reason that the toughness values measured using the micro-cantilever approach are in good agreement with bulk values.

Based on this, it may seem that the micro-cantilever approach is far superior to the tensile approach used here. However, it must be remembered that the cantilever approach cannot be used to measure the toughness of ductile specimens, making it impossible to quantify the effect of Bi segregation to a Cu GB. While the tensile approach certainly has some shortcomings, it does ensure that every specimen (no matter how brittle or ductile) can be broken and a toughness value obtained (the appropriateness and validity of this value will be discussed in more detail in the following section). So unfortunately, the choice of test technique is a bit of a "catch-22" in that neither technique can provide a complete data set that is comparable to all of the previous research done on the subject.

4.5.3 Validity of toughness values

As with all fracture toughness tests, the validity of the toughness value can only be determined after the fact. According to the ASTM E399 specification[49] for plane strain toughness (K_{IC}) testing, there are two criteria that must be met in order to qualify as a valid K_{IC} value. These criteria are designed to ensure that LEFM conditions are met. The first of these requires that the sample's behavior up to the point of fracture be primarily linear elastic. In other words, K_{IC} is not a valid fracture toughness quantity for materials that exhibit significant plasticity. As outlined in the ASTM specification, this is

determined by comparing the maximum load, P_{max}, which occurs at fracture, with a value, P_Q, which is an estimate of the elastic limit. P_Q is defined as the intersection of the data curve with a line starting at the origin that has a slope equal to 95% of the initial slope of the data curve. This construction is illustrated in Fig. 55 for the 33˚ doped specimen (chosen as the best-case scenario due to the least plasticity) and shows that $P_Q \approx 110$ MPa (using stress instead of load makes no difference) and $P_{max} \approx 160$ MPa. In order to be a valid test, the ratio P_{max}/P_Q must be less than 1.1. For this specimen, that ratio has a value of 1.45, meaning that the calculated toughness is not a valid plane strain toughness value. All other tests exhibited even more plastic deformation than this specimen, so this value would be even larger for the others. While this is less than ideal, it is certainly not unexpected given the dimensions of the specimens used in this work. Plane-strain testing of metals typically requires very large specimens so that enough triaxiality can build up at the crack tip to prevent plasticity. Smaller specimens typically fall under the plane stress category (or even lower), labeled as t_1 in Fig. 17. Unfortunately, there are no accepted standards for plane stress testing, primarily because the value of t_1 (corresponding to the maximum K_C) will be different for every material and any deviation from this value will have a significant impact on the results.

The second requirement essentially states that the size of the plastic zone must be significantly smaller than the dimensions of the specimen (a.k.a. small-scale yielding). A more detailed discussion on the size of the plastic zone developed during the tests conducted here will be given in a later section, but for now it is sufficient to say that this criterion is not met due to the extremely small specimens being used.

Based on these analyses, it is clear that the values being reported here are not valid K_{IC} values, and no claims to that end will be made. In fact, K is likely not the appropriate fracture toughness metric to use at all in this case. Based on the fairly large amount of plasticity seen, a technique such as the J-integral or the essential work of fracture (EWF) is likely more appropriate. However, these techniques typically require that a large number of specimens be tested with varying initial crack lengths and, in the case of J-testing, the displacements of many locations on the specimen must be measured experimentally, both of which would be extremely difficult and time-consuming using the experimental procedure used here. Therefore, caution must be taken when comparing the toughness values reported here with values that have been previously published from other studies. However, despite these shortcomings, the use of K_C in this document is perfectly acceptable for the purposes of comparison between self-similar tests.

4.6 Microtensile testing of un-notched single crystal specimen

One un-notched single crystal specimen was tested so that an accurate measurement of yield strength could be made. This value is critical when calculating the actual size of the plastic zone, which will be discussed in more detail later. However, it cannot be accurately determined from the fracture tests because the notches act as stress concentrators, so an un-notched specimen is needed. A single-crystal specimen was used, rather than a bicrystal, so that the uniaxial yield strength could easily be converted into the critical resolved shear stress, τ_{CRSS}, using the Schmid factor for the specimen's known crystallographic orientation (<100> loading axis). Fig. 59 shows the stress-strain curve generated from this test. This plot has the appearance of a classic tension test with linear

elasticity at first, followed by a period of strain hardening after the yield point, and ultimately ending with fracture. Looking at the elastic portion of the curve, shown in Fig. 60, a modulus of 72.2 GPa was measured, which is in fair agreement (~10% error) with the expected value of 66.7 GPa for a Cu single crystal with a uniaxial load applied along a <100> axis. In order to ensure that this error was not caused by misalignment of the specimen (i.e. loading axis slightly off from <100>), the modulus, E_{hkl}, was calculated as a function of orientation using the following equation[50]:

$$\frac{1}{E_{hkl}} = s_{11} - 2\left[s_{11} - s_{12} - \frac{1}{2}s_{44}\right]\left(m^2n^2 + n^2p^2 + m^2p^2\right) \tag{6}$$

where s_{11}, s_{12}, and s_{44} are the elastic compliance constants for Cu[44] and m, n, and p are the direction cosines defining the direction hkl. The resulting plot, shown in Fig. 61, shows that the modulus only varies by ~1 GPa if the loading axis of the specimen is 5° off from the desired orientation. This means that if the orientation of any sample (fracture specimens included) is off by a few degrees (which could happen during fabrication), there should be a very minimal impact on the modulus.

Furthermore, the maximum Schmid factor among the primary slip systems ({111}<110>) in this orientation is ~0.4. The stress-strain curve shows a yield strength (determined by its proportional limit) of ~150 MPa, corresponding to a critical resolved shear stress of ~60 MPa. This value will be very important as an input for the FEM work that will be discussed later in this chapter.

Fig. 62 shows an SEM image taken just after fracture of the single crystal specimen. Looking at this image, it appears that there may be a very slight neck formed across the width. There appears to be significant thinning near the edges of the fracture

zone. The slip steps on the surface are similar to those seen in the DENT fracture test specimens. It must be pointed out, however, that the engineering stress-strain curve shows no evidence of a neck forming because there is no maximum in the curve followed by a decrease in stress that would indicate a period of neck instability. This abrupt failure at a maximum load without clear formation and extension of a necked region is expected for a tension test performed under load control. This means that the neck (as well as all the slip steps) formed rapidly immediately before or during the fracture event, similar to how they formed in the fracture specimens. Also, it appears that final failure of this specimen occurred via a similar shear thinning mechanism as the DENT specimens.

4.7 Finite element modeling

Unfortunately, because full-field strain mapping was not possible using the techniques employed in this work, it is difficult to know the distributions of important quantities such as stress and strain near the notch tips. However, FEM can provide a good numerical estimate of these values, assuming the model is based on the real behavior of the material. To that end, a standard model for single-crystal plasticity[51] was incorporated into a commercial FEM program (ABAQUS) and used to simulate the behavior of the single crystal bowtie specimen discussed above. This model was then used to simulate the behavior of 6˚ and 33˚ bicrystal DENT specimens. The following sections will discuss the results of this modeling, including a detailed comparison to the experimental data in an effort to better understand the conditions in the test specimens at the point of fracture.

4.7.1 Modeling of single-crystal bowtie specimen

The single-crystal plasticity code used in this work employs a hardening law that uses three parameters: the critical resolved shear stress, the initial hardening modulus, and the easy-glide saturation stress. The critical resolved shear stress is, as previously discussed, the shear stress value required to initiate plastic deformation on a given slip system. The initial hardening modulus is the slope of the shear stress-shear strain curve just after the onset of plasticity. This slope gradually decreases until it reaches zero at the easy-glide saturation stress. At this point in the deformation process, there is essentially no work hardening and massive plastic deformation will occur. In order to accurately model the behavior of the single crystal specimen, a series of FEM simulations were performed with different values for these three parameters until a satisfactory fit was found.

Fig. 63 shows the meshed FEM part used in these simulations. This part represents $1/8^{th}$ of the actual bowtie specimen as it takes advantage of mirror-plane symmetry elements in all three dimensions. This part was pulled in tension by applying a known displacement in a series of steps to the wide end where it would be Pt-tacked in the actual experiment. It should be noted that no Poisson contraction was allowed at this end in order to better mimic the constraint imposed by the Pt tacks, even though some contraction was probably present in the real case. Fig. 64 shows the uniaxial stress distribution in the part at an early step during the simulation. In order to generate a stress-strain curve from the simulation, average single values for stress and strain were calculated for each displacement step. In order to calculate the stress value in the gauge

section for a given step, an average was taken using every node on the surface corresponding to the centerline of the part (the left side in this image). This was done in part to minimize any influence of the stress concentration located at the end of the gauge section, but also because the failure of the actual specimen occurred very close to the center of the beam. In order to calculate the strain for a given simulation step, a similar technique to that used in the actual experiment was employed. The displacement of a single node located along the centerline of the beam at the end of the gauge section was tracked for each step. The zero location was set at the beam center so that this nodal displacement was identical to the change in length of the gauge section. This was then converted into an engineering strain value by dividing by the initial gauge length. Fig. 65 shows the displacement contours for the same simulation step as shown before, as well as the location of the node used for calculating the uniaxial strain (indicated by a red dot). Using this procedure, a stress-strain curve was generated from every simulation and compared to the experimental curve shown in Fig. 59. Based on the goodness of this fit, the hardening parameters were modified for the next run until a good fit was found. Table 4 shows the values corresponding to this fit and Fig. 66 shows both the simulated and experimental stress-strain curves.

An assumption that was made in this analysis was that the Pt markers on the actual specimen were located precisely at the end of the gauge section (in line with the corner on the side of the specimen). However, if these were markers were slightly off to one side it is possible that it would impact the resulting stress-strain curve. If the markers were misplaced towards the center of the specimen, there would likely be no effect

because the cross-sectional area at this point is still the same. However, if the markers were located closer to the end of the specimen, this could increase the measured stiffness of the specimen because the cross-sectional area is effectively increased by a small amount. While it is difficult to know exactly how pronounced this effect would be experimentally, FEM can provide an estimate very easily. To that end, the simulated stress-strain behavior of the bowtie specimen was determined using a point ~1 μm past the end of the gauge section for the calculation of strain. Fig. 67 shows the elastic portions of the simulated curves using the end of the gauge section (blue curve) and 1 μm past this point (red curve). This plot shows that while the stiffness does increase, the effect is very small and can therefore be ignored. This is an important observation because it means that even if the Pt markers are not in the exact same spot on every specimen, the resulting stress-strain curves should not be affected.

4.7.2 Modeling of DENT bicrystal specimens

Once the single crystal behavior was well modeled, the FEM code was used to model the 6˚ and 33˚ DENT bicrystal specimens. The parts were created with a notch root radius of 125 nm, which is on the same order as the FIB-cut notches in the actual specimens. The length of the specimen was reduced to 7.5 μm (3.75 μm on either side of the boundary) to reduce the number of elements needed (and thus, computing time). Figs. 68-70 show a series of images depicting this model and the mesh used for all simulations. This model represents ¼ of an actual specimen and employs mirror plane symmetry elements in both the width and thickness (also to reduce computing time). The $1/8^{th}$ model used for the single crystal was not suitable in this case because the elastic

properties on the two sides of the grain boundary are different due to differences in crystallographic orientation. It should be noted that the mesh is significantly finer in the area surrounding the notch (see Fig. 70) so that the stress concentration in this region is correctly modeled. Once again, the model was loaded by applying a fixed, vertical displacement to one end (top) of the part with the other end (bottom) kept stationary. This loading configuration is a reasonably accurate representation of the loading conditions in an actual test.

Figs. 71 and 72 show the uniaxial stress distributions in the 6˚ and 33˚ bicrystals, respectively. From these images, the stress concentration effect of the notch is very clear. However, the stress contours are not symmetric with respect to the boundary (this is particularly clear in the 33˚ model). This asymmetry is obviously caused by the differences in orientation between the two grains and the resultant change in Schmid factors for active slip systems. This observation will have important consequences for the size and shape of the plastic zone, as well as the eventual transgranular shear failure. This point will be discussed in more detail later. In order to create a stress-strain curve for the part as a whole, the stress at each node on the top edge of the part was averaged for each simulation step. This is similar to what was done in the single-crystal bowtie model, except that the stress at the end of the part, instead of the middle, was used. This was done because it is identical to the gross-section stress that was used in the experimental stress-strain curves.

Fig. 73 shows the uniaxial displacement contour map for the 6˚ model. As in the single-crystal bowtie model, the engineering strain for each simulation step was

determined by tracking the displacement of two nodes whose locations correspond directly to the Pt markers used for strain measurement of the actual specimens, 2.5 μm away from the boundary on both sides.

Fig. 74 shows the stress-strain curves generated from FEM modeling of both misorientation angles, as well as the experimental curve from the 6˚ pure specimen for comparison (remember that the 33˚ pure experimental curve was nearly identical, so it was not included for clarity). There are several important features about this plot that should be discussed. First, the elastic slopes of the FEM curves, depicted in Fig. 75, are identical and match fairly well with the experimental curve. This effective modulus, ~59 GPa, is less than the <100> modulus of Cu due to the reduced cross-section between the notches. Recall that the experimental stress was calculated using the cross sectional area of the un-notched portions of the beam (i.e., the gross section stress). As previously mentioned, the low effective modulus value was expected and this value falls easily within the range of the experimentally measured values. This agreement provides even further evidence that the DIC technique is accurately measuring specimen elongation. Furthermore, Fig. 74 shows that the misorientation angle has almost no effect on the stress-strain behavior of a bicrystal, as the curves from each overlap perfectly. While perhaps surprising at first, this actually makes perfect sense given that the boundaries being modeled are pure twist boundaries, rather than tilt or random boundaries. This means that not only are the loading axes the same in each grain (identical elastic stiffnesses), but the Schmid factors for every slip system will also be identical on both sides of the boundary, regardless of misorientation angle. This means that yielding will

occur at the same stress level and that the hardening behavior of each grain will be similar as well when a continuum-based hardening model is used. This is exactly what was observed in the experimental results as well, as the behavior of both pure boundaries was nearly identical. It should be noted again that the doped boundaries did exhibit a slightly different stress-strain behavior, which could potentially be due to a change in the dislocation emission behavior of the boundary due to the presence of Bi. However, this conclusion is pure speculation at this point, as significantly more experimental and modeling work would be necessary for proof. Lastly, and perhaps most importantly, there is a distinct difference in the behavior of the simulated curves and the experimental curves after the yield point: the experimental curves show significantly less work hardening than the FEM predicts. In order to understand the cause of this discrepancy, it must be remembered that the hardening behavior in the FEM code was based solely on the hardening behavior of a single-crystal (i.e. boundary-less) specimen. However, it is well established that the boundary will act as the primary dislocation nucleation (or emission) site in a bicrystal specimen[29]. Therefore, it is perfectly reasonable that the work hardening behavior of a bicrystal specimen (even an un-notched one, if such a test were to be conducted) would be different than that of a single crystal, simply due to the relative ease of nucleating a much larger number of dislocations at the boundary vs. generating them from other types of defects (i.e. Frank-Read sources).

With this difference in behavior between the simulated and experimental curves in mind, a question of which curve should be used as a fit for the hardening parameters arises. In this work, as discussed above, the hardening behavior of the single crystal was

used as for fitting and then applied to the bicrystal. It is believed that this is the more appropriate choice (rather than fitting directly to the bicrystal data) because work hardening is not, in its truest sense, based on dislocation nucleation. Rather, it is based on the interactions of a network of already mobile dislocations as they glide through the crystal. These interactions are already accurately included in the FEM model based on the single-crystal data. If the hardening behavior were modified to account for dislocation emission from the boundary, it is likely that the behavior of the material away from the boundary (at the edge of the plastic zone, for example) would no longer be correctly modeled. In this example, the size of the plastic zone would be overestimated, leading to the potential for inaccurate conclusions to be drawn from the FEM results.

As mentioned above, and several times previously, the size and shape of the plastic zone ahead of the notches is extremely important and will have a significant impact on the fracture test results. The FEM models used here can provide a reasonable estimate of this, now that the material parameters used in the models are known to be accurate. Unfortunately, the single-crystal plasticity code used in these models does not directly differentiate between elastic and plastic deformation, so the FEM software can not directly identify which elements have yielded and which have not at a given point in time. Furthermore, the rate-dependent hardening law that is used in the code creates a finite amount of plastic strain in every simulation step, even if the resolved shear stress is not above the critical value on any slip systems. While this strain is very small when the local stress is below the yield stress, it still complicates things in terms of defining a yield criterion. In bulk-scale testing, a 0.2% offset technique is typically used to define yield

stress from a simple tension test. There are a number of reasons why this is done, but one of them is to ensure that true yielding has occurred, not just localized micro-plasticity. This is even more important in small-scale testing, particularly when a stress concentration (such as a notch) is present. With this in mind, a plastic strain of 0.002 (0.2%) was used as the threshold for determining whether a given element has yielded or not. While this value is not an insignificant portion of the total strain at failure (~10% for pure specimens), it is a commonly used metric and there would be no strong justification for using a smaller value.

Figs. 76 and 77 show the plastic zone (in red) for the 6˚ and 33˚ models, respectively, at a simulation increment prior to reaching the elastic limit (yield point) on the stress-strain curves shown in Fig. 74. As expected, they demonstrate that plastic deformation occurs at the notches while the rest of the beam is behaving elastically. These images show that for the 6˚ model, the plastic zone is quite symmetric with respect to the boundary, as would be expected for a low angle boundary with very similar orientations on both sides. However, for the 33˚ boundary, the plastic zone is very asymmetric and is larger in one grain than in the other. This is likely caused by a number of different factors, including a larger elastic mismatch between the grains orthogonal to the loading direction and differences in orientation of active slip systems relative to the notch (where the stresses are the highest). It is interesting to note that despite the development of a clear plastic zone with a radius of ~50% of the specimen width, the overall behavior of the notched specimen still appears to be linear elastic at this point.

This is likely due to constraint from the surrounding material that has not yet yielded, limiting the impact of the plastic zone on the overall strain behavior.

Fig. 78 shows the shape of the plastic zone for the 33˚ model at the elastic limit (~130 MPa) of the stress-strain curve shown in Fig. 74. The equivalent image for the 6˚ boundary looks similar, with symmetric zones in each grain. This image represents the first step in the simulation where the plastic zone encompassed the entire width of the specimen (in the notched region). This means that the apparent yield point of both the simulated and experimental stress-strain curves corresponds to the point at which the entire ligament has plastically deformed. While this is certainly not an unexpected result, it was impossible to know for sure from just the experimental results. As the specimen is strained past this point, the plastic zone will grow outward (away from the boundary) until it encompasses the entire specimen. However, this is where the FEM model can no longer accurately simulate the behavior of the real specimen, as the model simply cannot take dislocation nucleation sites into account, as previously discussed. In the actual specimen, the number of dislocations nucleated at the grain boundary will likely outnumber those nucleated elsewhere in the plastic zone by a significant margin. Furthermore, it is entirely likely that dislocation emission from the boundary into one of the grains will be preferred over the other, leading to an even more asymmetric plastic zone than predicted by the FEM model.

Ultimately at the point of failure, the majority of the plastic deformation will have occurred in a region much smaller than the plastic zone size predicted by the FEM simulation, as evidenced by the locations of the slip steps on the post-fracture SEM

images (Fig. 49, for example). While it is difficult to make any exact measurement of this region due to the extreme amount of plasticity that occurred during the fracture event, no slip steps can be seen more then ~1 μm away from the boundary. Because the slip planes are oriented close to 45˚ (54.5˚, in reality) from the boundary, this distance should be roughly the same as the specimen thickness, as this is the maximum distance a dislocation emitted from the boundary can travel before it reaches the surface of the specimen (where it creates a slip step). This limitation on the "acting" plastic zone size reduces the volume of material that is actually dissipating energy through plasticity even more than would be predicted by the FEM model, and may ultimately cause the measured toughness value to be even lower than would be predicted based solely on the specimen dimensions.

5. CONCLUSIONS

While the work presented here is only a portion of a much larger project that could potentially have much more far-reaching implications, there are some very important conclusions that can be drawn from this work on its own.

1. It was shown that micro-scale SENT and DENT tests could be used to measure fracture toughness in specimens exhibiting ductile fracture. This is not true of the more popular micro-cantilever test, suggesting that the tensile techniques have a significantly broader range of potential applications even though they are more difficult to perform.
2. As expected based on previously published work, no grain boundary embrittlement was observed in a low angle (6˚) twist boundary and a significant amount was seen in a high angle (33˚) twist boundary. However, some degree of embrittlement was observed in an intermediate (13˚) twist boundary, suggesting that the critical angle for both segregation and embrittlement may be slightly different for pure twist grain boundaries than for pure tilt boundaries.
3. All fracture toughness values from DENT tests, regardless of the amount of ductility seen in the stress-strain curves, were observed to be extremely low, with values ranging from ~0.5 $MPa \cdot m^{1/2}$ down to ~0.3 $MPa \cdot m^{1/2}$. The magnitude of these values can be explained by a size-effect where the specimen dimensions limit the size of the plastic zone that develops ahead of the notch tips. This limits the volume of material available for energy dissipation through plastic deformation and results in a reduction in the measured toughness.

4. A standard single-crystal plasticity model was incorporated into a commercial FEM software package in order to simulate the deformation behavior of the DENT bicrystal specimens. These models show that the plastic zone size that develops can be asymmetric across the boundary due to the misorientation of the two grains, which is likely to influence the direction of crack propagation during final fracture. Furthermore, the size of the plastic zone at failure is likely overestimated by the FEM models, as they cannot take the boundary's role in dislocation nucleation into account.

6. SUGGESTIONS FOR FUTURE WORK

First and foremost, the other portions of this project (chemical analysis and atomic-resolution imaging of the boundaries) must be completed so that the results presented here can be put into the correct context. Without this information, it is impossible to even speculate about the mechanism responsible for the observed embrittlement, which is the ultimate goal of the project as a whole. However, the mechanical testing has brought up several interesting points that deserve to be investigated on their own. For example, it would be very interesting to conduct micro-cantilever tests on the boundaries that exhibited embrittlement (13˚ and 33˚) to see how the results compare with the results from Armstrong *et al.*[34,35]. Could these boundaries, which still showed a fair amount of ductility despite being embrittled, even be fractured in a micro-cantilever test? This type of direct comparison between the two techniques could be extremely valuable in determining the applicability of each technique in other areas of research.

Another possible spin-off from this work could be an investigation into the effect of specimen size on the degree of embrittlement. The focus of this would not be on the size dependence of the toughness values themselves, but rather on the degree to which the toughness decreases due to Bi-doping (in the boundaries that can be embrittled at all). As mentioned earlier, the results from the SENT tests on the 13˚ and the DENT tests on the 33˚ boundary suggests that there should be a relationship between the allowable plastic zone size (as determined by specimen dimensions and geometry) and the magnitude of the toughness difference between pure and doped boundaries. While this

does not have direct implications for the Cu-Bi system on its own, it could be important in the design and fabrication of small-scale structures, such as those found in MEMS devices. If it is the case that the degree of boundary embrittlement scales with specimen dimensions, this could impact the design requirements for such structures that are made out of materials susceptible to embrittlement (almost all materials are to some degree).

Another aspect of this work that would benefit from further study is the determination of the critical misorientation angle for segregation and embrittlement in pure twist grain boundaries. This would require the fabrication of more bicrystals with misorientation angles spaced out at regular intervals (between 3-5˚ would likely be sufficient) in the range between 6˚ and 33˚. Ultimately, the goal would be to create a plot similar to that shown in Fig. 12 for twist boundaries. The results of this work suggest that the two boundary types may not behave identically in this respect. Further investigation would reveal if this is actually the case and, if so, why? The difference in boundary types could influence the plasticity that occurs during testing, as both the relative ease of nucleation as well as hardening behavior may be different for edge dislocations emitted from a tilt boundary vs. screw dislocations emitted from a twist boundary.

Finally, and perhaps most interestingly, further investigation into the effect of impurity segregation on plasticity could result in extremely impactful conclusions. This would likely require mechanical testing of un-notched bicrystal specimens (both pure and doped with a variety of dopants) as well as some form of atomistic modeling to determine the energy required to emit a dislocation from a grain boundary under a variety of different conditions (i.e. different misorientations, different dopants, different doping

levels, different loading configurations, etc.). This topic has yet to be investigated in any great detail, but if it turns out that impurity segregation does impact the yield strength of a material, the potential implications could impact the entire field of materials science.

7. REFERENCES

1. Bannister, C. O. & Doyle, W. M. Bismuth in copper: Its effects, determination, and some experiments in its gaseous elimination. *Trans. Inst. Min. Met.* **44,** (1935).

2. Voce, E. & Hallowes, A. P. C. The mechanism of the embrittlement of deoxidized copper by bismuth. *J. Inst. Met.* **73,** 323–376 (1947).

3. McLean, D. *Grain boundaries in metals*. (Clarendon Press, 1957).

4. Brunauer, S., Emmett, P. H. & Teller, E. Adsorption of gases in multimolecular layers. *J. Am. Chem. Soc.* **60,** 309–319 (1938).

5. Seah, M. P. & Hondros, E. D. Grain Boundary Segregation. *Proc. R. Soc. Lond. Math. Phys. Sci.* **335,** 191–212 (1973).

6. Joshi, A. & Stein, D. F. An Auger spectroscopic analysis of bismuth segregated to grain boundaries in copper. *J. Inst. Met.* **99,** 178–181 (1971).

7. Powell, B. D. & Mykura, H. Segregation of bismuth to grain boundaries in copper-bismuth alloys. *Acta Met.* **21,** 1151–1156 (1973).

8. Powell, B. D. & Woodruff, D. P. Anisotropy in grain boundary segregation in copper-bismuth alloys. *Philos. Mag.* **34,** 169–176 (1976).

9. Fraczkiewicz, A. & Biscondi, M. Intergranular segregation of bismuth in copper bicrystals. *J. Phys.* **46,** 497–503 (1985).

10. Li, G. H., Wu, X. J., Cai, M., Qiu, Q. & Tang, Q. H. A fractographic study of bismuth embrittlement of tilt boundaries in a copper bicrystal. *Scr. Met. Mater.* **24,** 2129–2134 (1990).

11. Laporte, V., Berger, P. & Wolski, K. Quantitative AES, XPS and RBS determination of intergranular bismuth coverage in copper bicrystals at 500 C. *Surf. Interface Anal.* **37,** 809–820 (2005).

12. Keast, V. J., La Fontaine, A. & du Plessis, J. Variability in the segregation of bismuth between grain boundaries in copper. *Acta Mater.* **55,** 5149–5155 (2007).

13. Baumann, S. F. & Williams, D. B. A STEM/X-ray microanalytical study of the equilibrium segregation of bismuth in copper. *J. Microsc.* **123,** 299–305 (1981).

14. Michael, J. R. & Williams, D. B. An analytical electron microscope study of the kinetics of the equilibrium segregation of bismuth in copper. *Met. Trans.* **15A,** 99–105 (1984).

15. Bruley, J., Keast, V. J. & Williams, D. B. Measurement of the localized electronic structure associated with bismuth segregation to copper grain boundaries. *J. Phys. Appl. Phys.* **29,** 1730 (1996).

16. Keast, V. J., Bruley, J., Rez, P., Maclaren, J. M. & Williams, D. B. Chemistry and bonding changes associated with the segregation of Bi to grain boundaries in Cu. *Acta Mater.* **46,** 481–490 (1998).

17. Keast, V. J. & Williams, D. . Quantitative compositional mapping of Bi segregation to grain boundaries in Cu. *Acta Mater.* **47,** 3999–40008 (1999).

18. Bruley, J., Keast, V. . & Williams, D. . An EELS study of segregation-induced grain-boundary embrittlement of copper. *Acta Mater.* **47,** 4009–4017 (1999).

19. Duscher, G., Chisholm, M. F., Alber, U. & Rühle, M. Bismuth-induced embrittlement of copper grain boundaries. *Nat. Mater.* **3,** 621–626 (2004).

20. Wang, J.-S. A new type of brittle fracture in a fcc metal bicrystal with intergranular segregation. *J. Mater. Res.* **3,** 16–28 (1988).

21. Watanabe, M. *et al.* Improvements in the X-Ray Analytical Capabilities of a Scanning Transmission Electron Microscope by Spherical-Aberration Correction. *Microsc. Microanal.* **12,** 515–526 (2006).

22. Sutton, A. P. & Vitek, V. An atomistic study of tilt grain boundaries with substitutional impurities. *Acta Met.* **30,** 2011–2033 (1982).

23. Peng, B., Wu, X., Zhou, F. & Tang, Q. Molecular dynamic study of grain boundary embrittlement for [101] tilt copper bicrystals induced by bismuth segregation. *J. Appl. Phys.* **71,** 1229–1236 (1992).

24. Alber, U., Müllejans, H. & Rühle, M. Bismuth segregation at copper grain boundaries. *Acta Mater.* **47,** 4047–4060 (1999).

25. Hondros, E. D. & McLean, D. Cohesion margin of copper. *Philos. Mag.* **29,** 771–795 (1974).

26. Russell, J. D. & Winter, A. T. Orientation effects in embrittlement of copper bicrystals by bismuth. *Scr. Met.* **19,** 575–579 (1985).

27. Chikwembani, S. & Weertman, J. Fatigue and fracture of copper-bismuth bicrystals. *Scr. Met.* **19,** 1499–1502 (1985).

28. Chikwembani, S. & Weertman, J. Fatigue crack growth and fracture behavior of bismuth-doped copper bicrystals. *Met. Trans. Phys. Met. Mater. Sci.* **20 A,** 1221–1231 (1989).

29. Wang, J.-S. & Anderson, P. M. Fracture behavior of embrittled F.C.C. metal bicrystals. *Acta Met. Mater.* **39,** 779–792 (1991).

30. Rice, J. R. & Thomson, R. Ductile versus brittle behaviour of crystals. *Philos. Mag.* **29,** 73–97 (1974).

31. Li, G. H. & Zhang, L. D. Relationship between misorientation and bismuth induced embrittlement of [001] tilt boundary in copper bicrystal. *Scr. Met. Mater.* **32,** 1335–1340 (1995).

32. Uchic, M. D., Shade, P. A. & Dimiduk, D. M. Plasticity of micrometer-scale single crystals in compression. *Annu. Rev. Mater. Res.* **39,** 361–386 (2009).

33. Legros, M., Gianola, D. s. & Motz, C. Quantitative in situ mechanical testing in electron microscopes. *Mrs Bull.* **35,** 354–360 (2010).

34. Armstrong, D. E. J., Wilkinson, A. J. & Roberts, S. G. Measuring local mechanical properties using FIB machined microcantilevers. in **1185,** 7–13 (Materials Research Society, 2009).

35. Armstrong, D. E. J., Wilkinson, A. J. & Roberts, S. G. Micro-mechanical measurements of fracture toughness of bismuth embrittled copper grain boundaries. *Philos. Mag. Lett.* **91,** 394–400 (2011).

36. Schweinfest, R., Paxton, A. T. & Finnis, M. W. Bismuth embrittlement of copper is an atomic size effect. *Nature* **432,** 1008–1011 (2004).

37. Geng, W. T., Freeman, A. J. & Olson, G. B. Atomic size effect in impurity induced grain boundary embrittlement. *Mater. Trans.* **47,** 2113–2114 (2006).

38. Muller, D. A. Why changes in bond lengths and cohesion lead to core-level shifts in metals, and consequences for the spatial difference method. *Ultramicroscopy* **78,** 163–174 (1999).

39. Kraft, O., Schwaiger, R. & Nix, W. d. Measurement of Mechanical Properties in Small Dimensions by Microbeam Deflection. *Mrs Online Proc. Libr.* **518,** null–null (1998).

40. Ichikawa, Y. *et al.* Fracture Behavior of Micro-Sized Ni-P Amorphous Alloy Specimens. *Mrs Online Proc. Libr.* **605,** null–null (1999).

41. Koyama, S., Takashima, K. & Higo, Y. Fracture toughness measurement of a micro-sized single crystal silicon. in **297-300,** 292–295 (Trans Tech Publications Ltd, 2005).

42. Di Maio, D. & Roberts, S. g. Measuring fracture toughness of coatings using focused-ion-beam-machined microbeams. *J. Mater. Res.* **20,** 299–302 (2005).

43. Hosokawa, H., Desai, A. V. & Haque, M. A. Plane stress fracture toughness of freestanding nanoscale thin films. *Thin Solid Films* **516,** 6444–6447 (2008).

44. Hertzberg, R. W. *Deformation and Fracture Mechanics of Engineering Materials*. (John Wiley & Sons, Inc., 1995).

45. Kang, Y.-L., Zhang, Z.-F., Wang, H.-W. & Qin, Q.-H. Experimental investigations of the effect of thickness on fracture toughness of metallic foils. *Mater. Sci. Eng.* **394,** 312–319 (2005).

46. Telari, K. A. *et al.* Characterization of platinum films deposited by focused ion beam-assisted chemical vapor deposition. *J. Vac. Sci. Technol. B Microelectron. Nanometer Struct.* **20,** 590–595 (2002).

47. Tada, H., Paris, P. C. & Irwin, G. R. *The stress analysis of cracks handbook*. (American Society of Mechanical Engineers, 2000).

48. Gjostein, N. . & Rhines, F. . Absolute interfacial energies of [001] tilt and twist grain boundaries in copper. *Acta Met.* **7,** 319–330 (1959).

49. ASTM standard E399-08. *Standard test method for linear-elastic plane-strain fracture toughness KIC of metallic materials*. (ASTM International, 2008).

50. Hopcroft, M. A., Nix, W. D. & Kenny, T. W. What is the Young's Modulus of Silicon? *J. Microelectromechanical Syst.* **19,** 229–238 (2010).

51. Huang, Y. *A user-material subroutine incorporating single crystal plasticity in the ABAQUS finite element program*. (Harvard Univ., 1991).

Table 1. Fracture toughness values calculated from SENT tests on 13˚ boundary.

Specimen	**K_C (MPa·$m^{1/2}$)**
Pure	2.24 ± 0.98
Bi-doped	1.17 ± 0.18

Table 2. Fracture toughness values calculated from DENT tests on 6˚ boundary.

Specimen	**K_C (MPa·$m^{1/2}$)**
Pure	0.54 ± 0.08
Bi-doped	0.46 ± 0.01

Table 3. Fracture toughness values calculated from DENT tests on 33˚ boundary.

Specimen	**K_C (MPa·$m^{1/2}$)**
Pure	0.54 ± 0.06
Bi-doped	0.33 ± 0.11

Table 4. Hardening law constants used in single-crystal plasticity FEM code. Values were determined by fitting to results of single-crystal microtensile test.

Parameter	Value (MPa)
τ_0	58
h_0	2400
τ_1	165

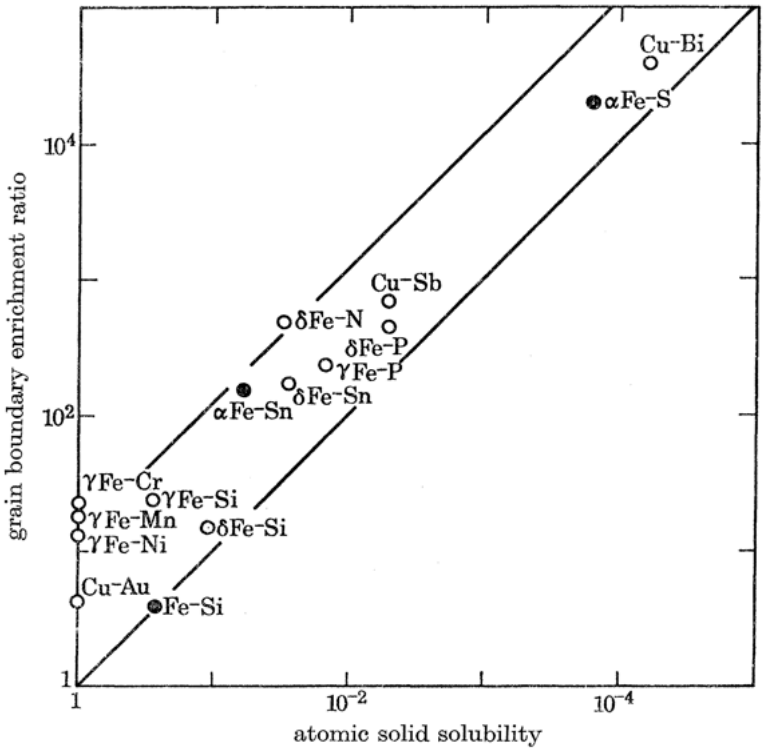

Fig. 1. Grain boundary enrichment ratio vs. atomic solid solubility for a variety of binary alloy systems[5].

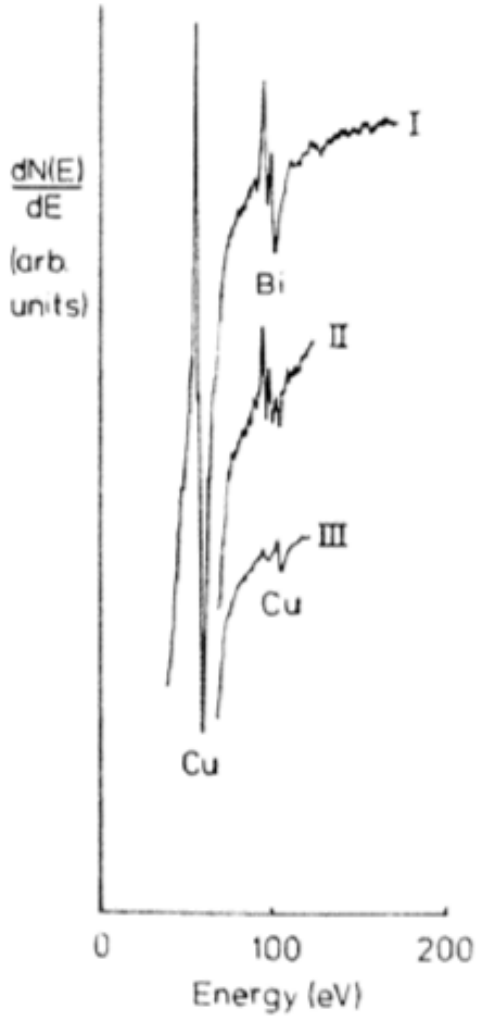

Fig. 2. AES spectra collected from Cu specimens containing different amounts of Bi[7].

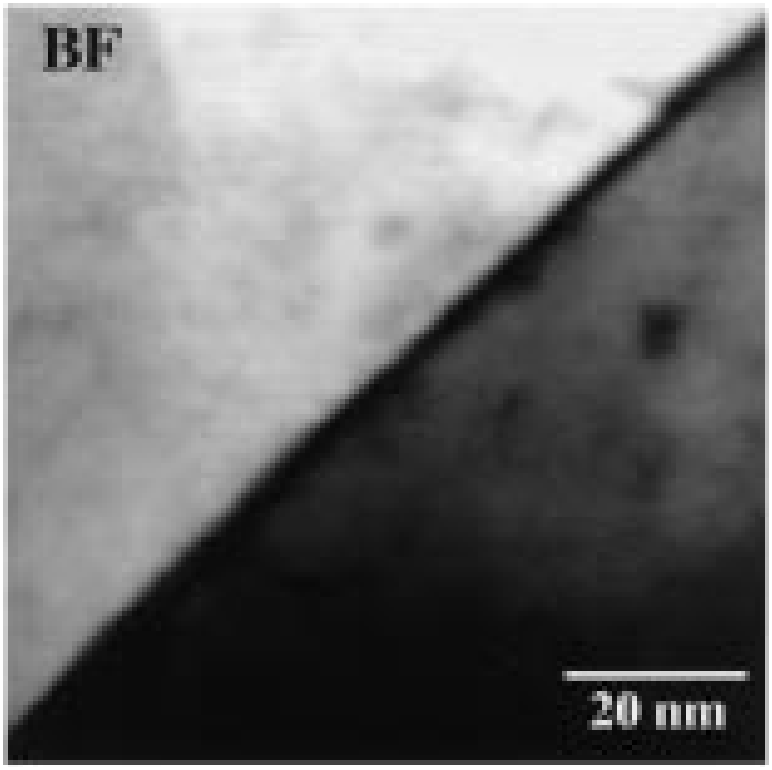

Fig. 3. Bright-field TEM image of a grain boundary in Cu showing diffraction contrast between the grains[17].

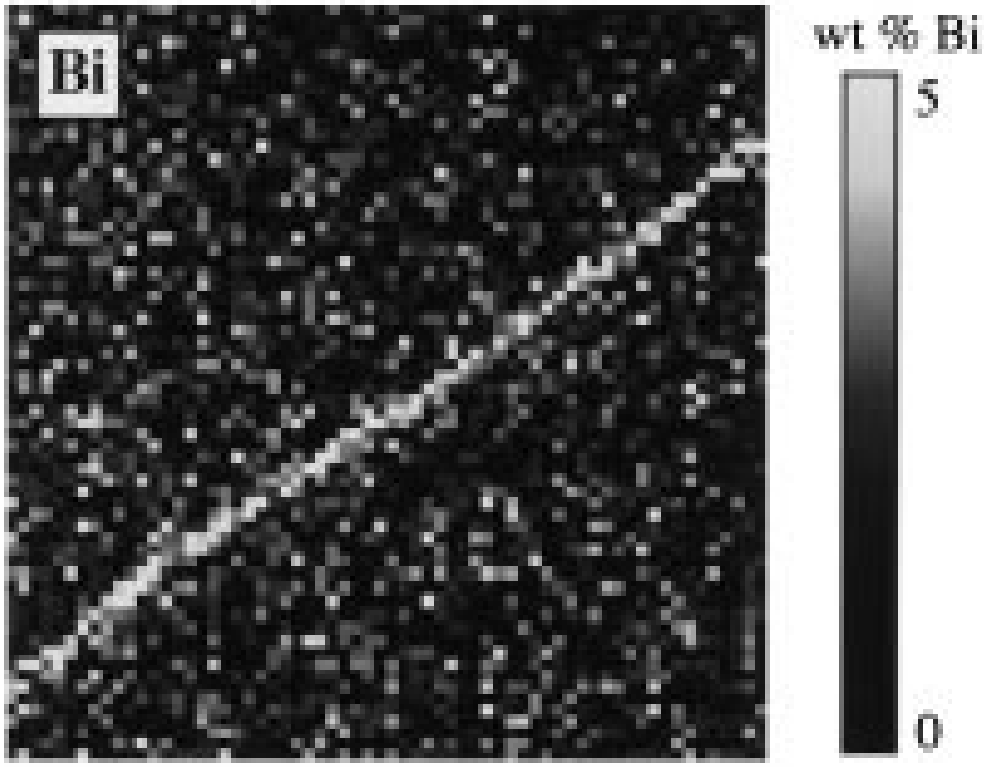

Fig. 4. Quantitative EDS map depicting the concentration of Bi at a Cu grain boundary [17].

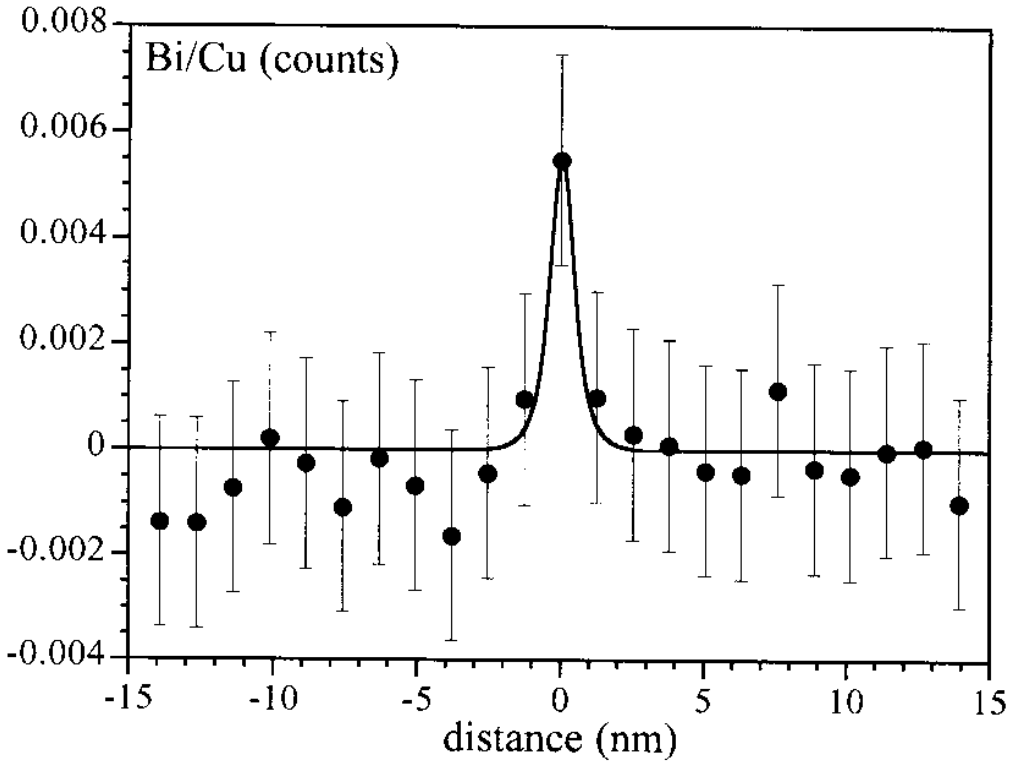

Fig. 5. Ratio of Bi to Cu counts in EDS spectra taken along a line perpendicular to a grain boundary located at x=0[17].

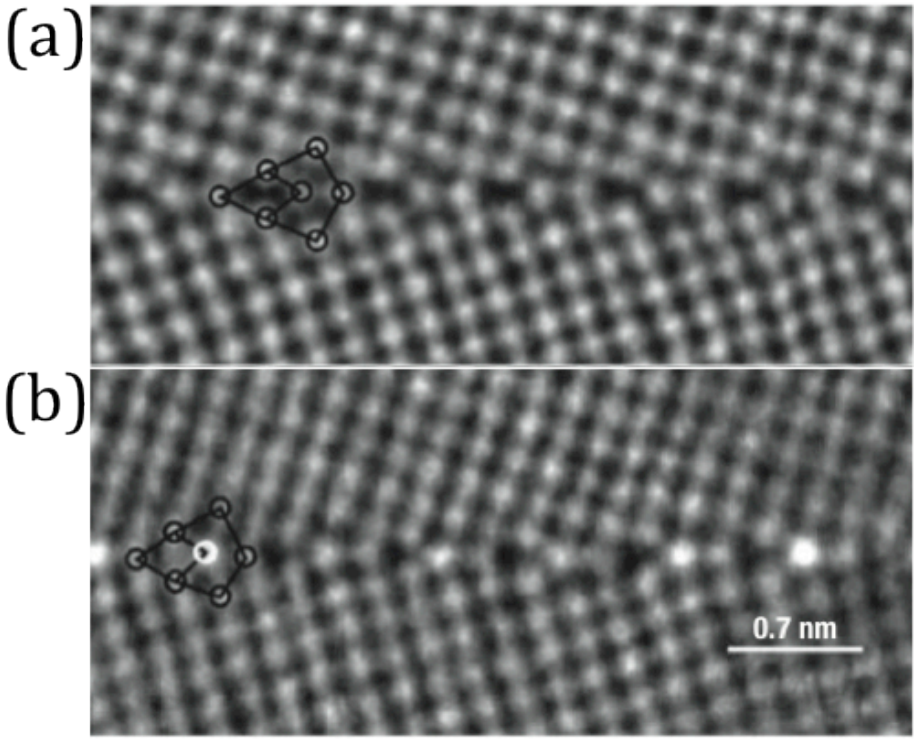

Fig. 6. Atomic resolution STEM images of a (a) pure and (b) Bi-doped symmetric 36.8° <001> tilt boundary[19]. Bright spots visible in (b) but not in (a) represent Bi atoms segregated to the boundary in a periodic arrangement.

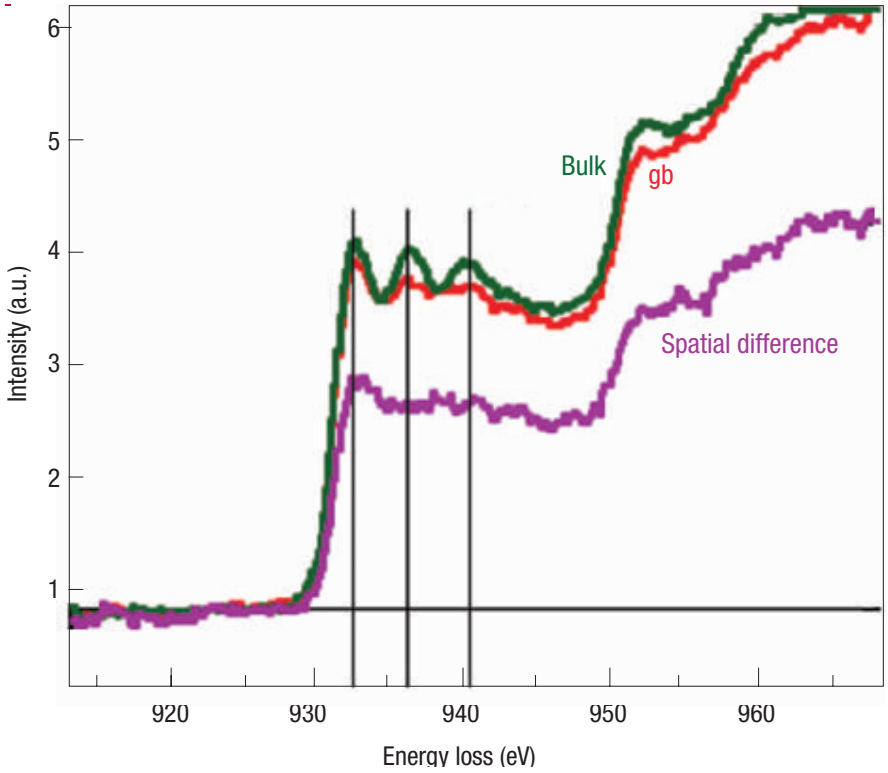

Fig. 7. EELS spectra taken in bulk Cu and near a Bi-doped boundary showing a difference in the electronic structure of atoms near the boundary [19].

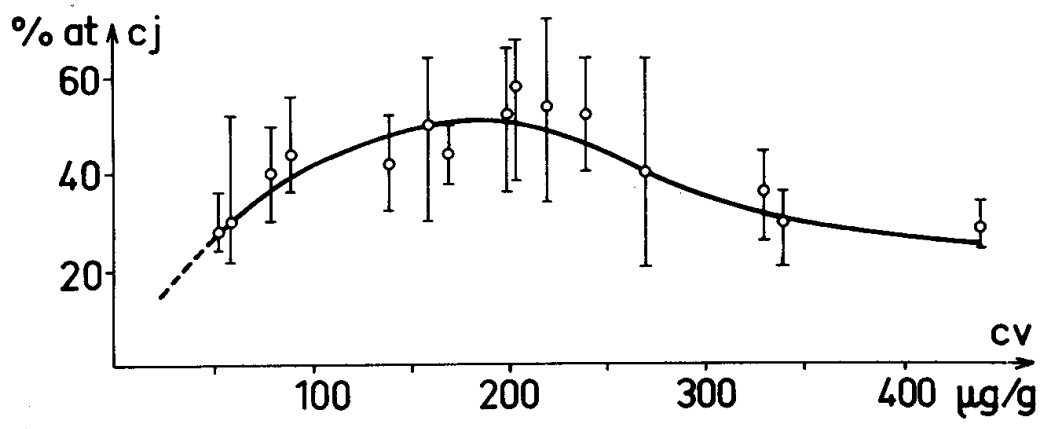

Fig. 8. Grain boundary Bi concentration (*cj*) vs. bulk Bi concentration (*cv*) for <001> tilt boundary (misorientation angle unknown)[9].

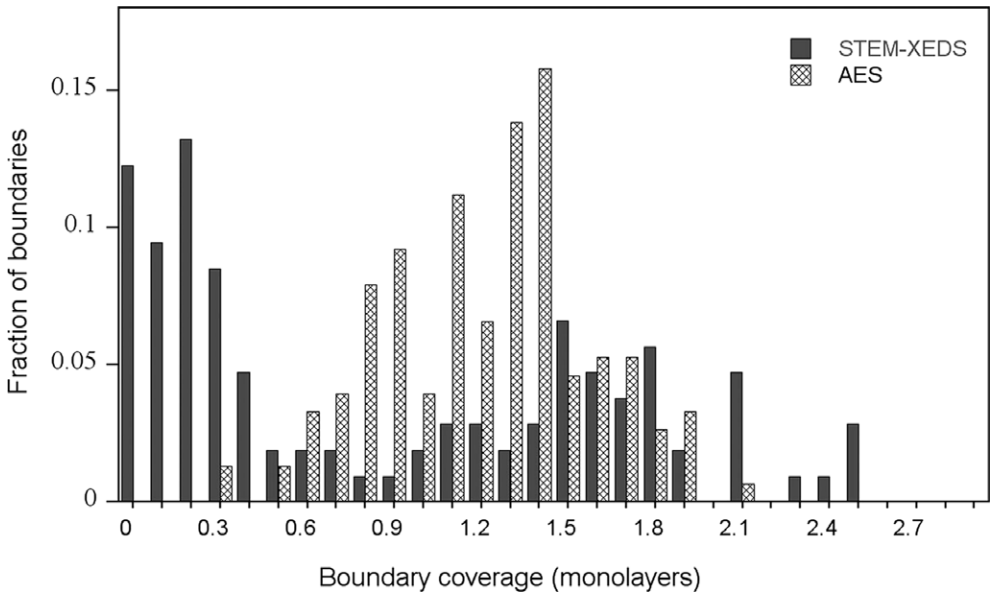

Fig. 9. Distribution of Bi boundary coverage for a large number of boundaries in polycrystalline Cu. Results shown are from both AES and AEM (labeled as STEM-XEDS)[12].

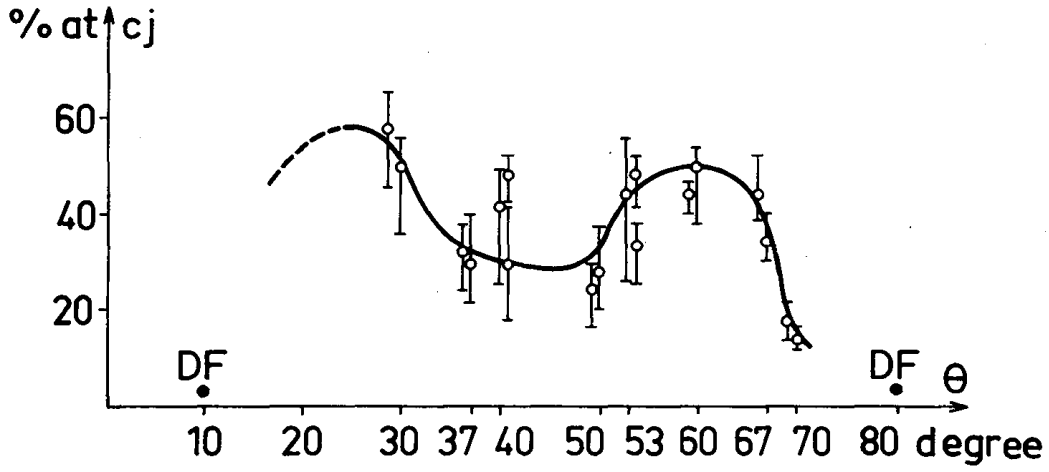

Fig. 10. Grain boundary Bi concentration as a function of misorientation angle for <100> tilt boundaries[9].

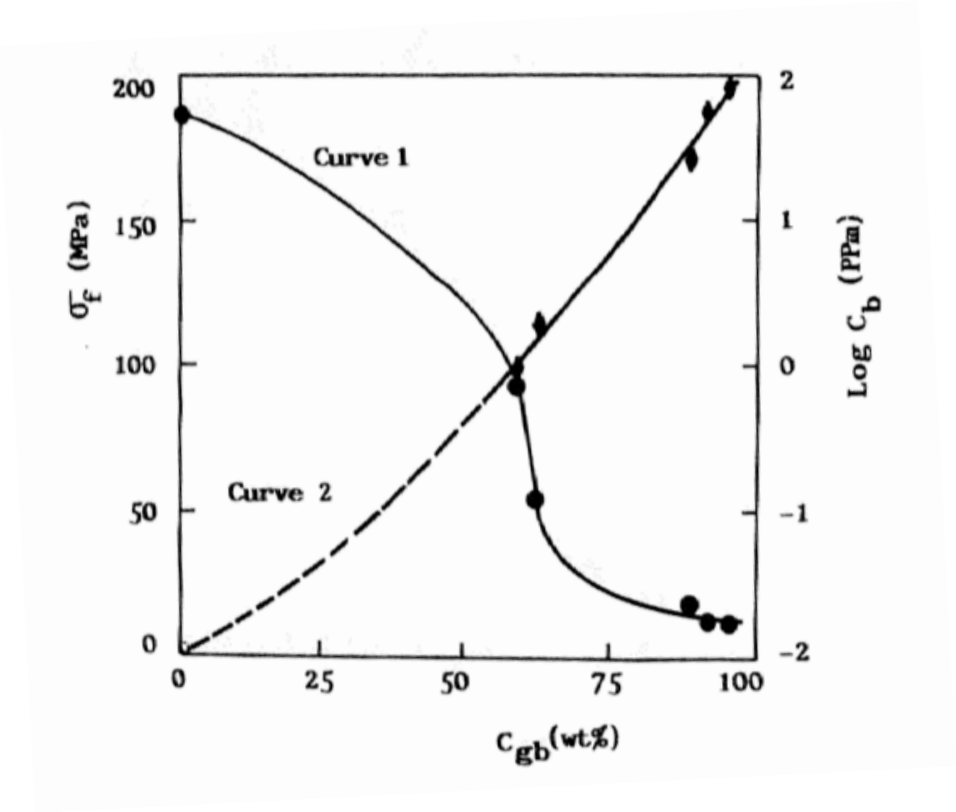

Fig. 11. Fracture stress as a function of intergranular Bi concentration for a 20.05° [110] tilt bicrystal determined by post-fracture AES[10].

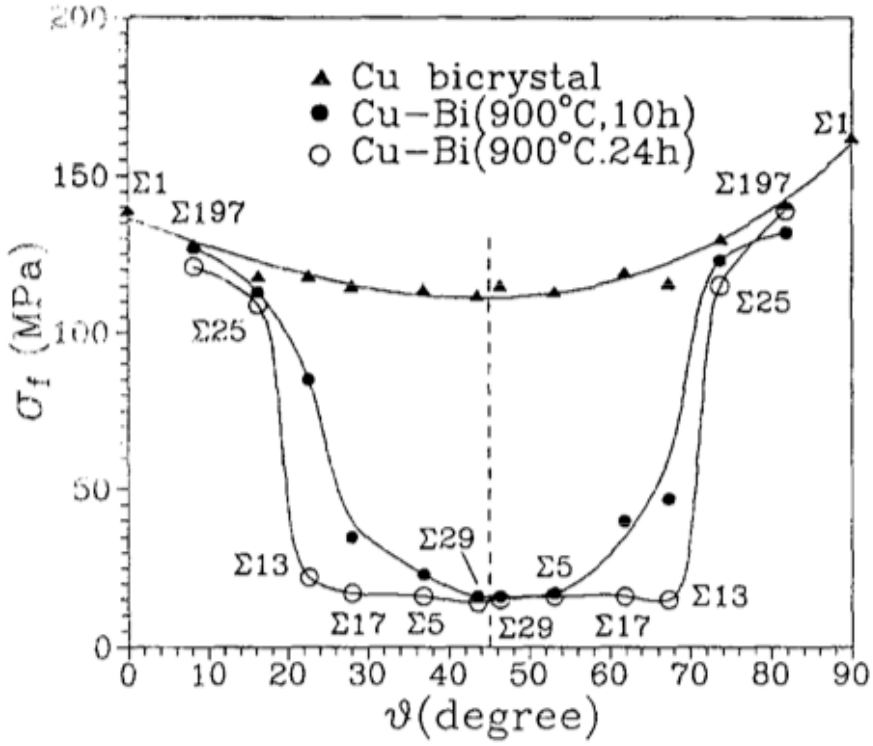

Fig. 12. Fracture stress as a function of misorientation angle and annealing time for pure and Bi-doped [001] tilt bicrystals[31].

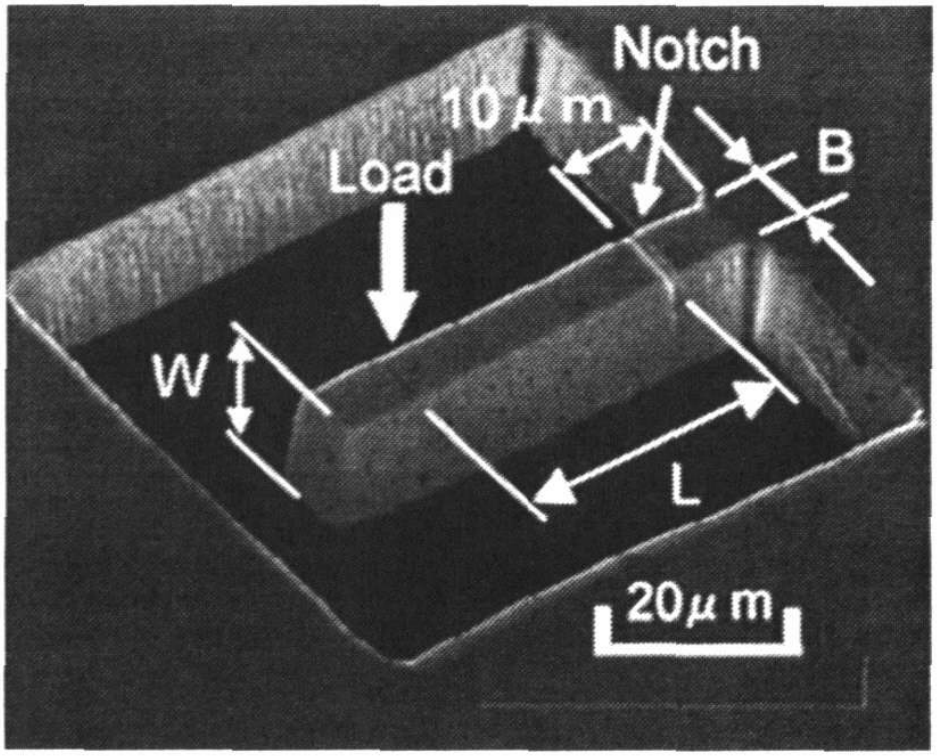

Fig. 13. SEM image of a FIB-machined notched micro-cantilever in amorphous Ni-P alloy[40].

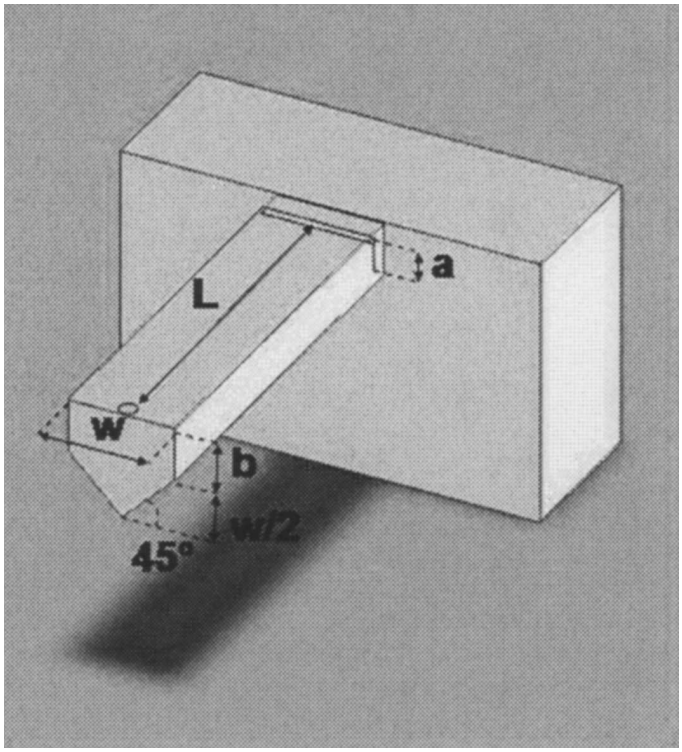

Fig. 14. Schematic diagram of FIB-machined notched micro-cantilever with pentagonal cross-section[42].

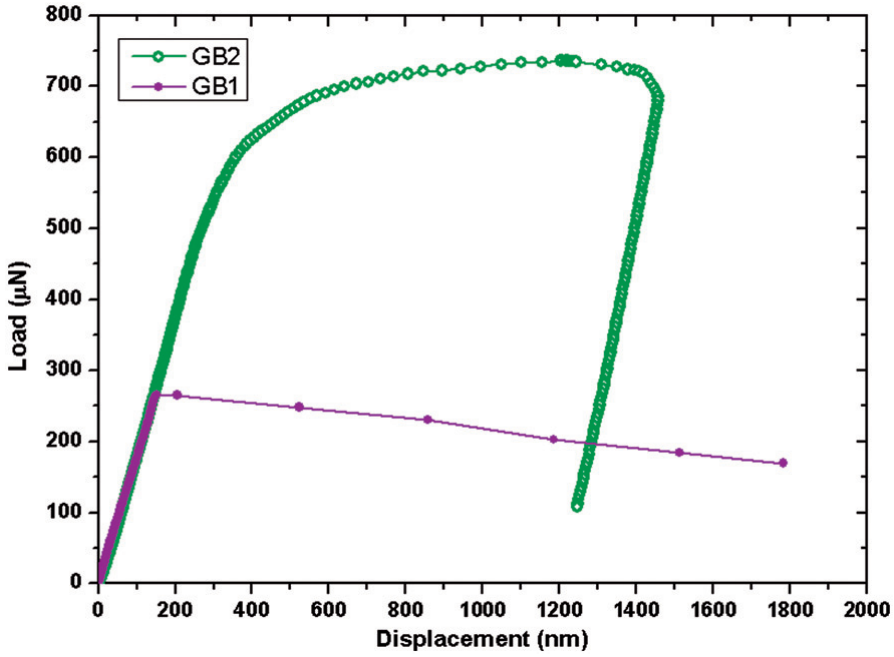

Fig. 15. Load-displacement curves from micro-cantilever tests on individual grain boundaries in Bi-doped Cu[35]. Purple curve (GB1) shows brittle fracture caused by grain boundary embrittlement and green curve (GB2) shows classic ductile behavior due to a lack of Bi segregated to boundary.

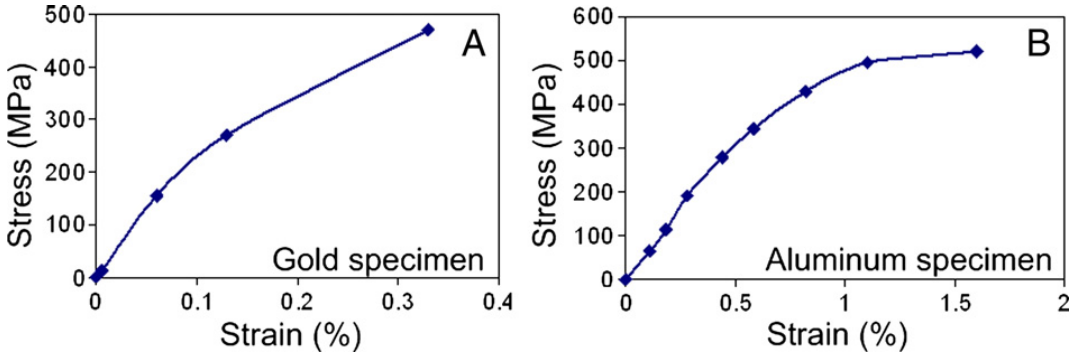

Fig. 16. Stress-strain curves generated from notched microtensile tests on (A) Au and (B) Al films[43]. Both curves show signs of plastic deformation prior to catastrophic failure.

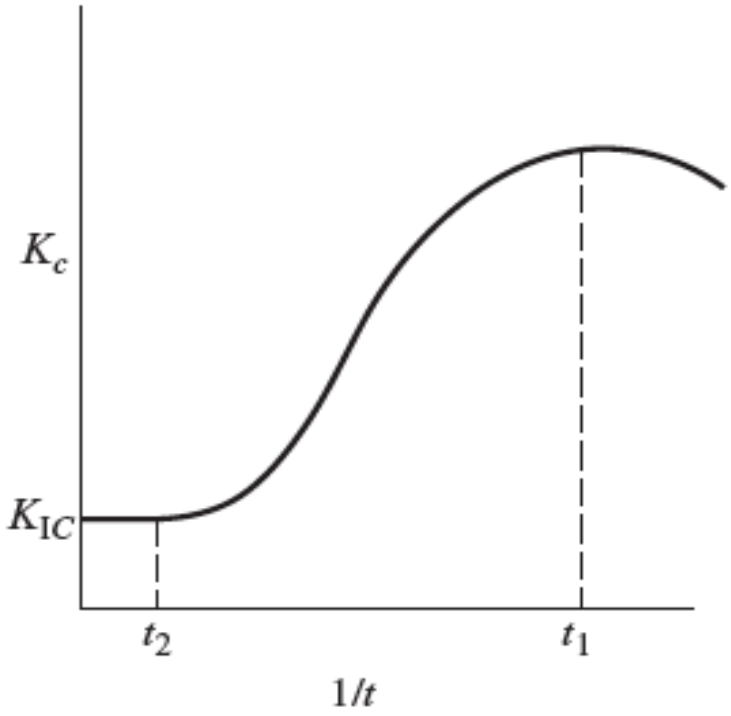

Fig. 17. Schematic plot of fracture toughness as a function of inverse specimen thickness[44]. Thicknesses greater than t_2 qualify as plane strain conditions. Thicknesses near t_1 are considered to be plane stress. Note that for specimens smaller than this the toughness begins to decrease again and will trend towards zero for very small specimens.

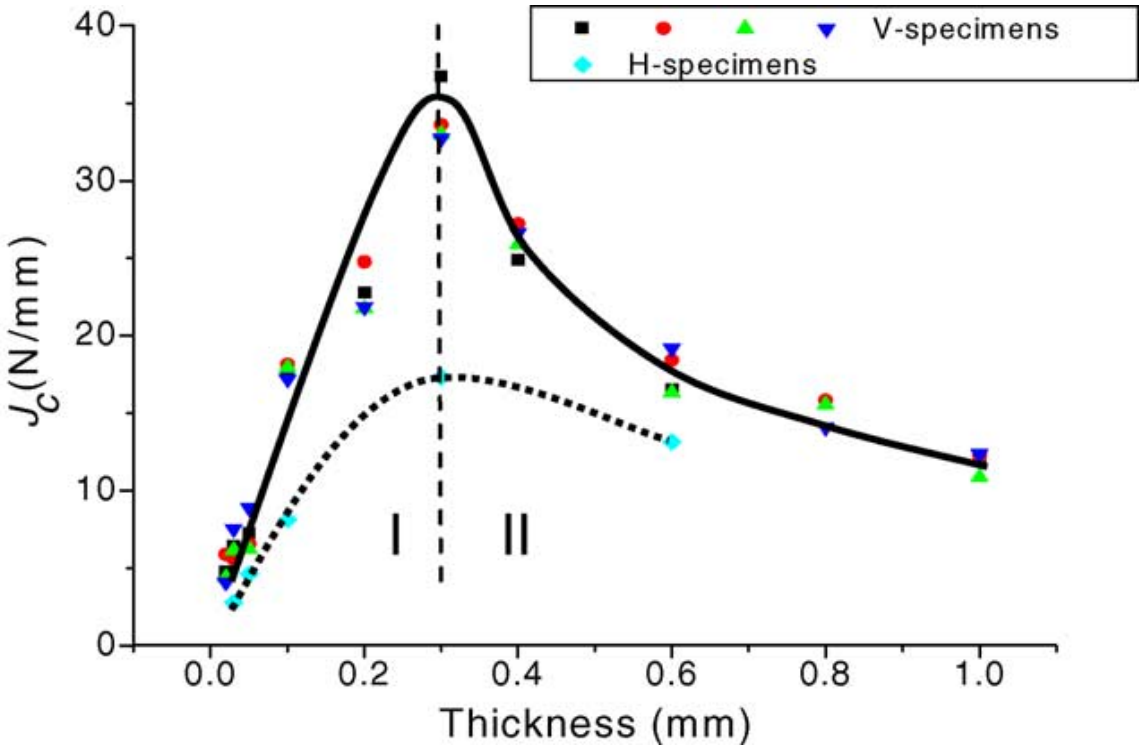

Fig. 18. Fracture toughness as a function of specimen thickness in various Cu foils[45].

Fig. 19. Bi-encrusted polycrystalline Cu rod encapsulated in evacuated glass tube for heat treating.

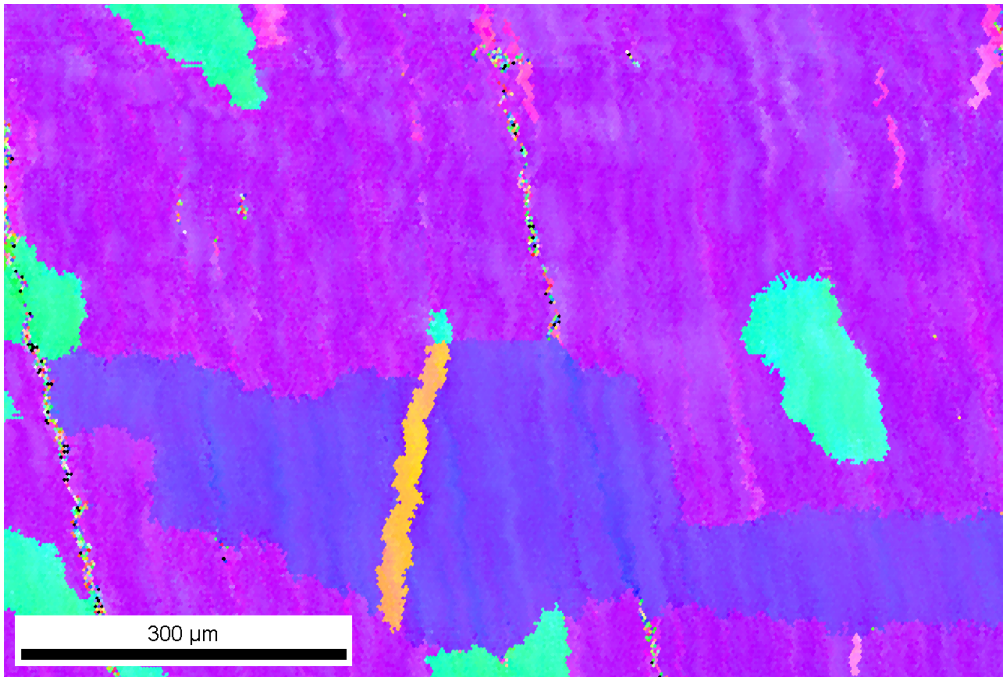

Fig. 20. EBSD map of polycrystalline Cu-Bi rod showing large grains and annealing twins.

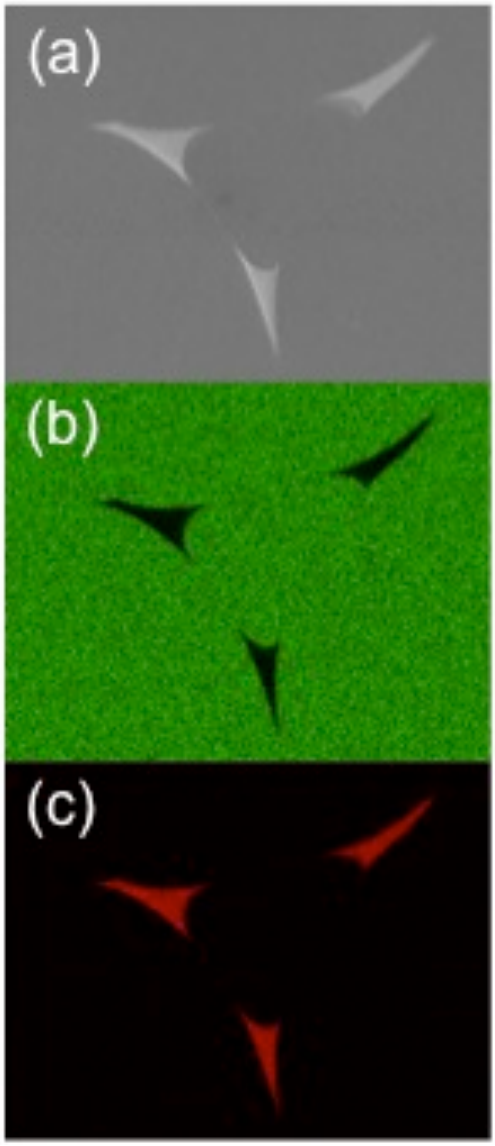

Fig. 21. (a) SEM image of a group of triple points surrounding a small grain in polycrystalline Cu-Bi. Also shown are EDS maps of same area showing location of (b) Cu and (c) Bi.

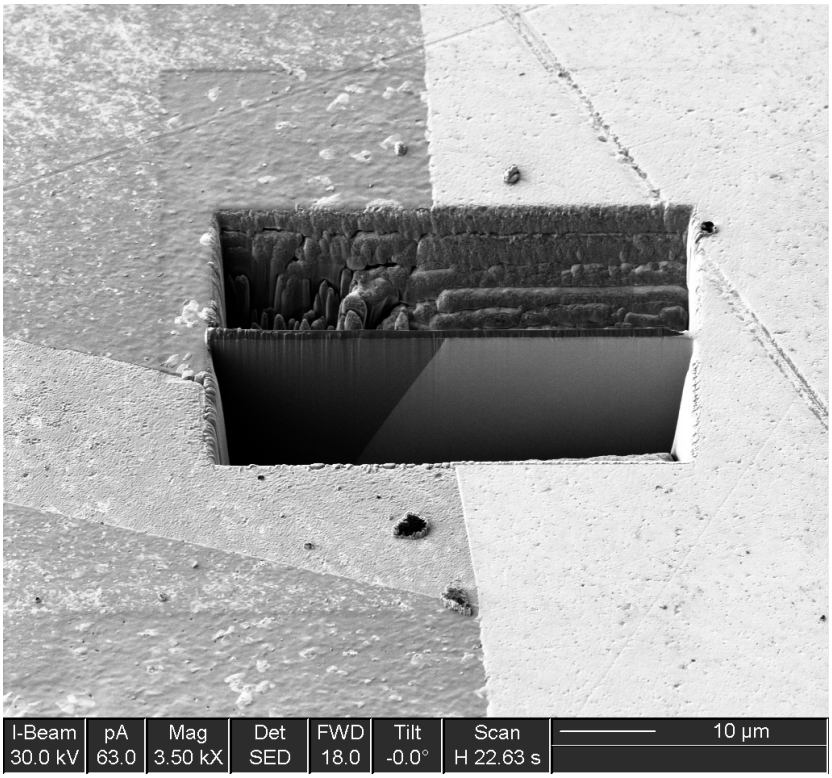

Fig. 22. FIB image of specimen during fabrication from polycrystalline Cu-Bi rod. Ion-channeling contrast shows location of boundary on the surface as well as on the specimen itself. Note the large inclination angle of the boundary beneath the surface.

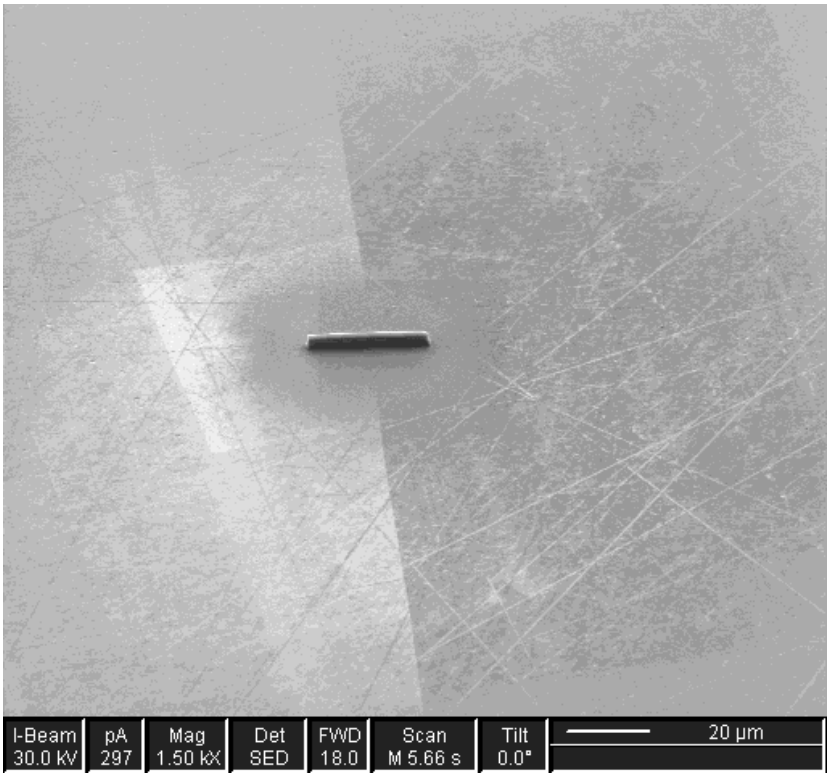

Fig. 23. FIB image of bicrystal sample showing extremely straight boundary as well as location of protective Pt layer deposited on surface.

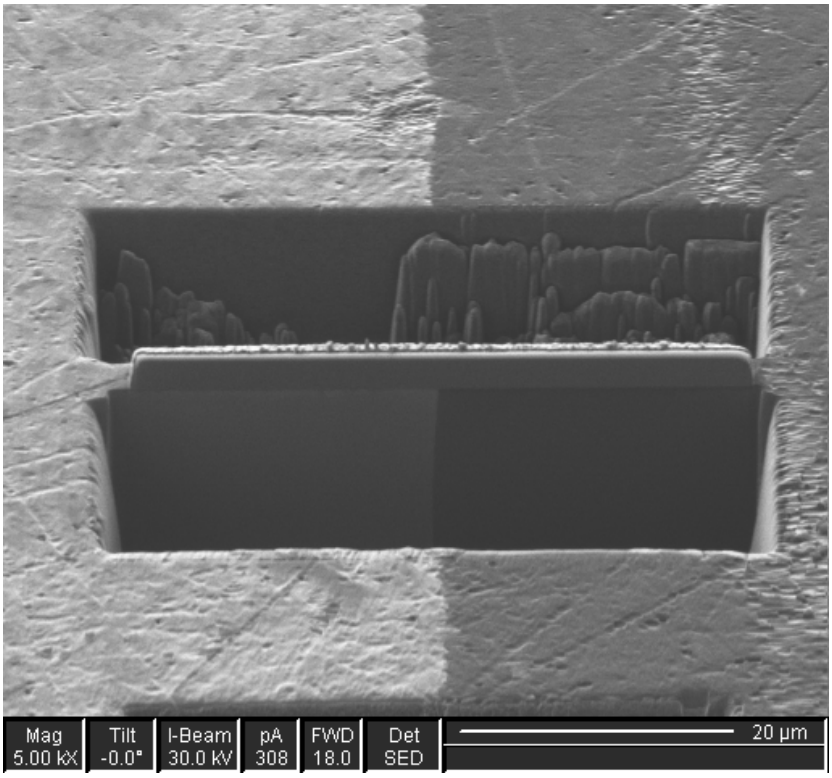

Fig. 24. FIB image of bicrystal specimen during fabrication. Note the almost negligible inclination of the boundary beneath the surface of the sample.

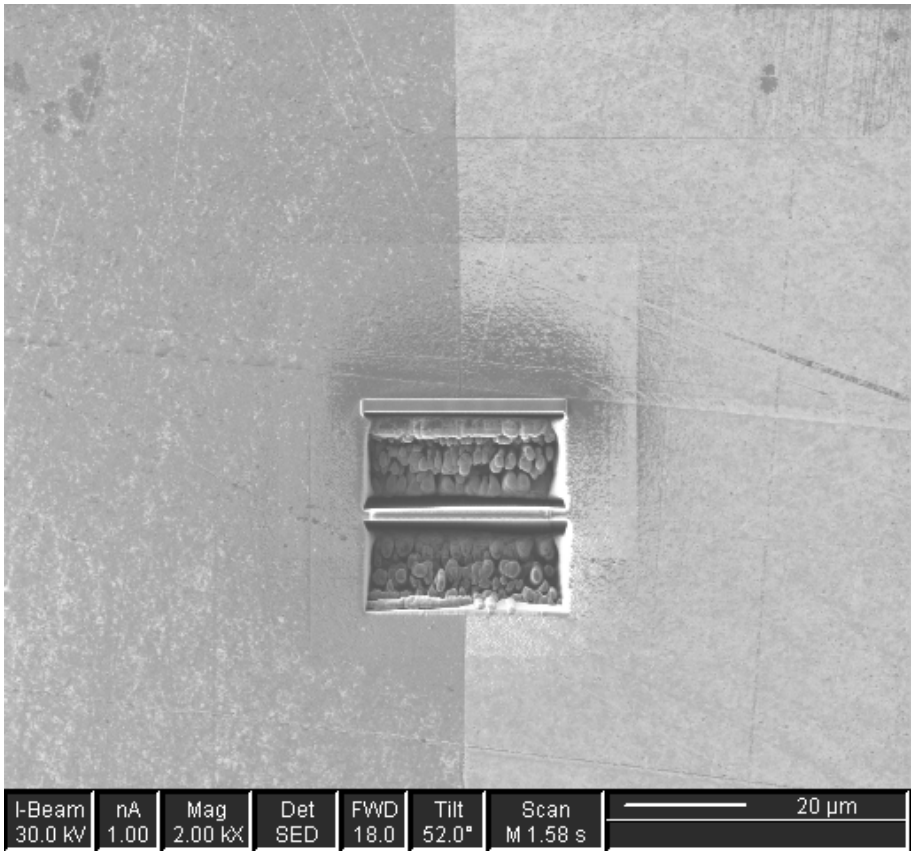

Fig. 25. FIB image showing the location of two specimens in close proximity to each other. This was done in order to reduce FIB milling time as well as ensure that variations in boundary character from one specimen to the next were minimal.

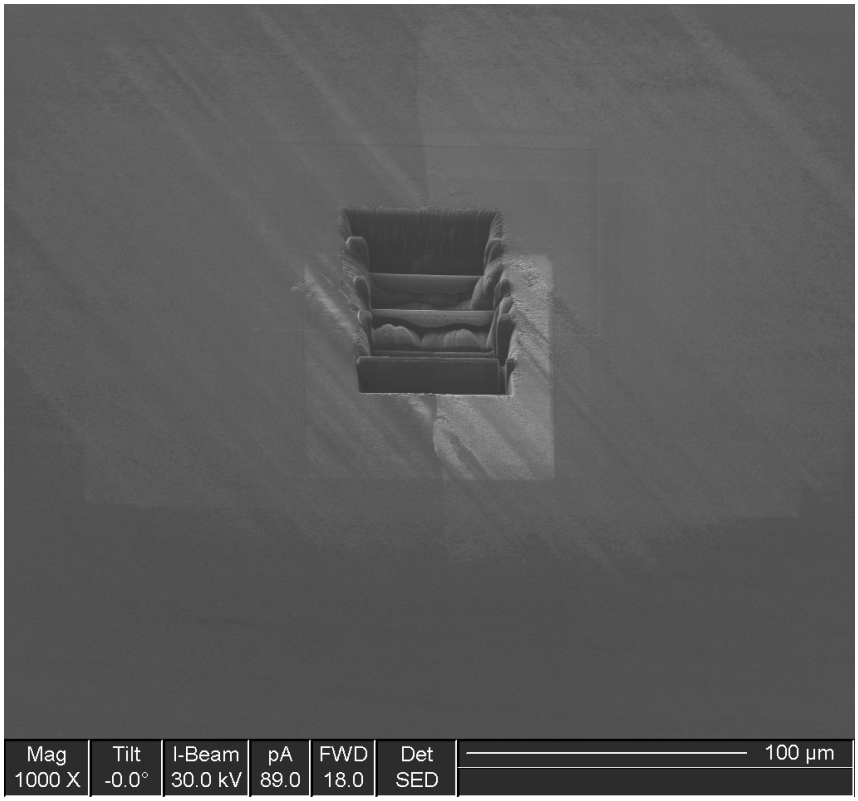

Fig. 26. FIB image showing locations of several removed specimens from a single boundary.

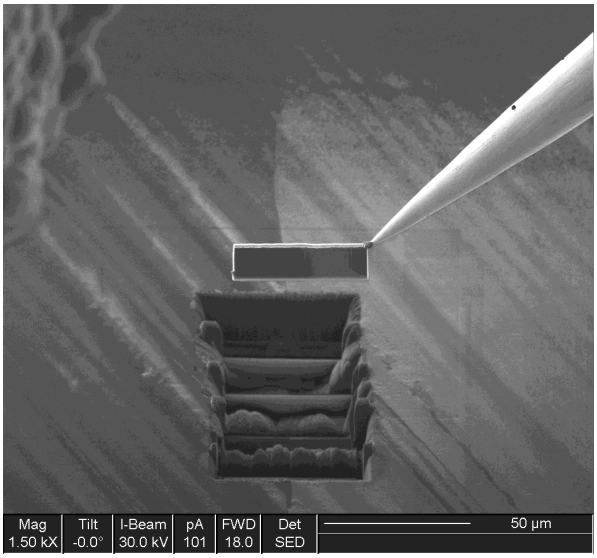

Fig. 27. FIB image showing extraction of a specimen from the bulk using a sharp W plucker needle.

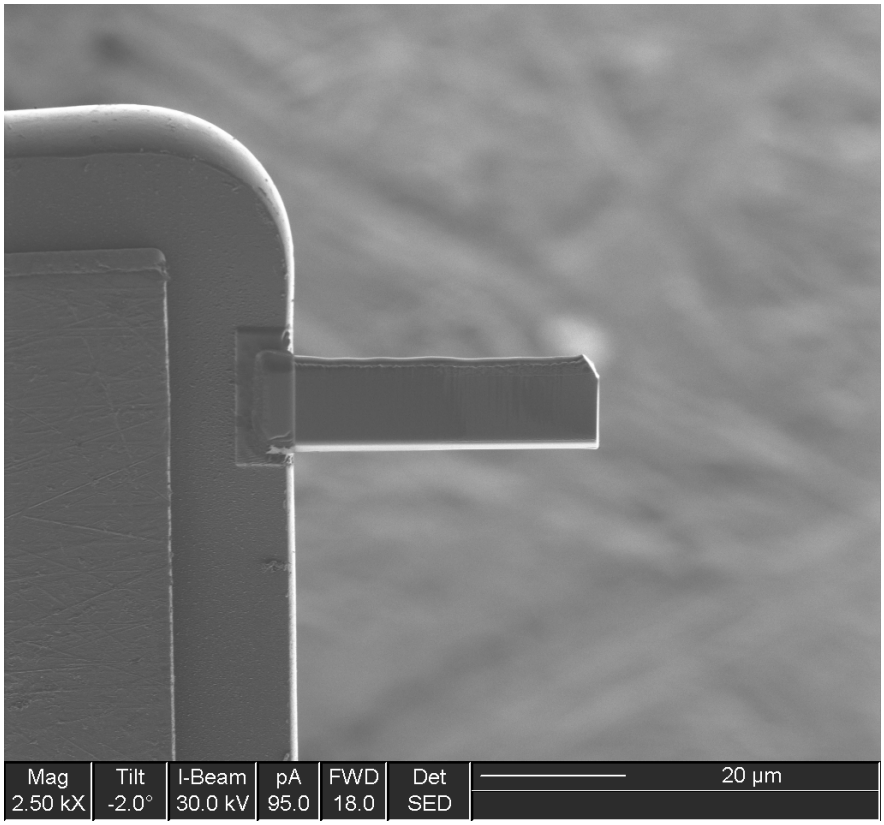

Fig. 28. FIB image of specimen mounted onto Cu grid following extraction from bulk.

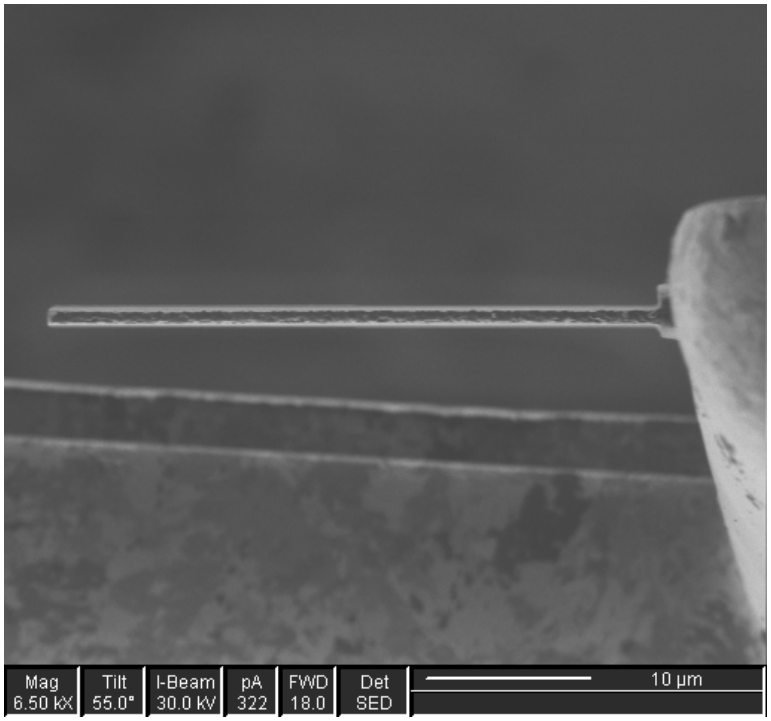

Fig. 29. FIB image showing specimen following thinning steps. Specimen is ~1.0 µm thick at this point.

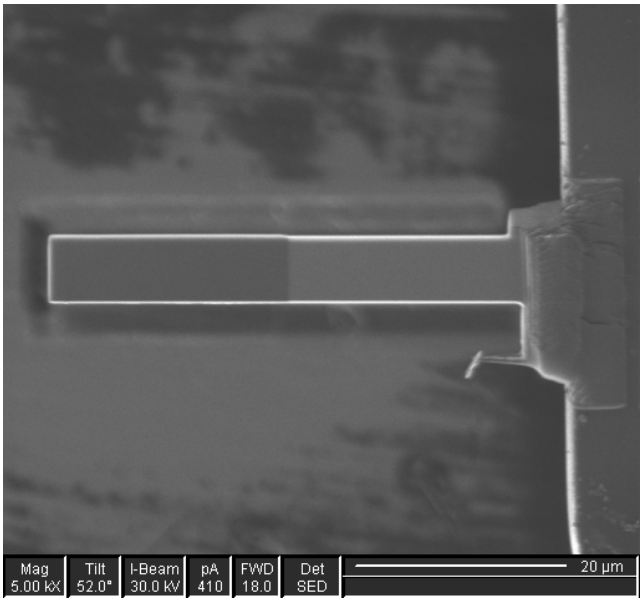

Fig. 30. FIB image of specimen after defining width of specimen to be ~6 µm with the long axis perfectly perpendicular to boundary seen in center of specimen.

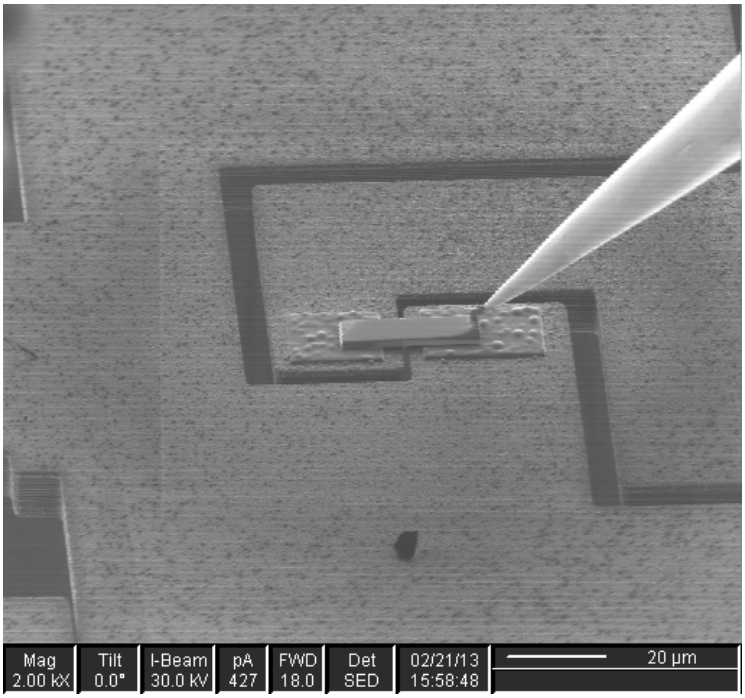

Fig. 31. FIB image showing placement of test specimen on PTP device using W plucker needle again. Once in place, specimen will be Pt-tacked down and cut free from needle.

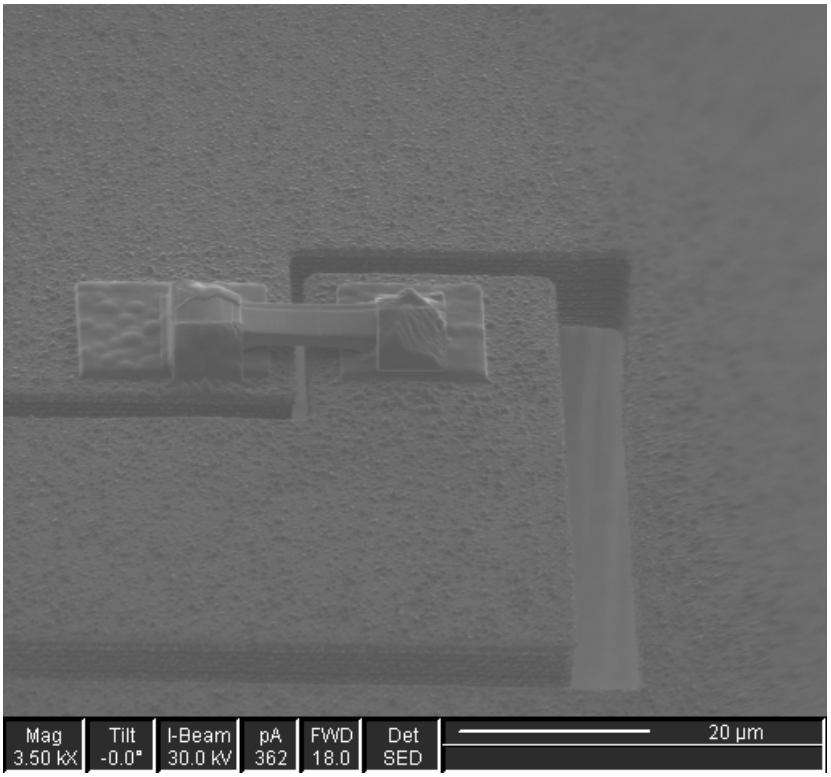

Fig. 32. FIB image of specimen after being Pt-tacked in place on PTP device.

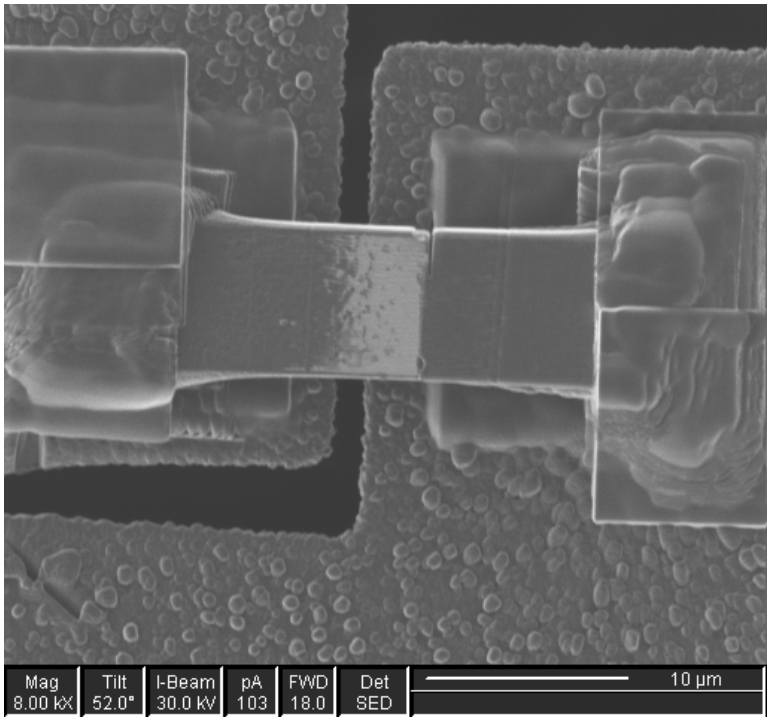

Fig. 33. SENT test specimen after notching at the boundary (on top edge). Contrast seen in left grain is due to excess Pt deposited on surface of specimen.

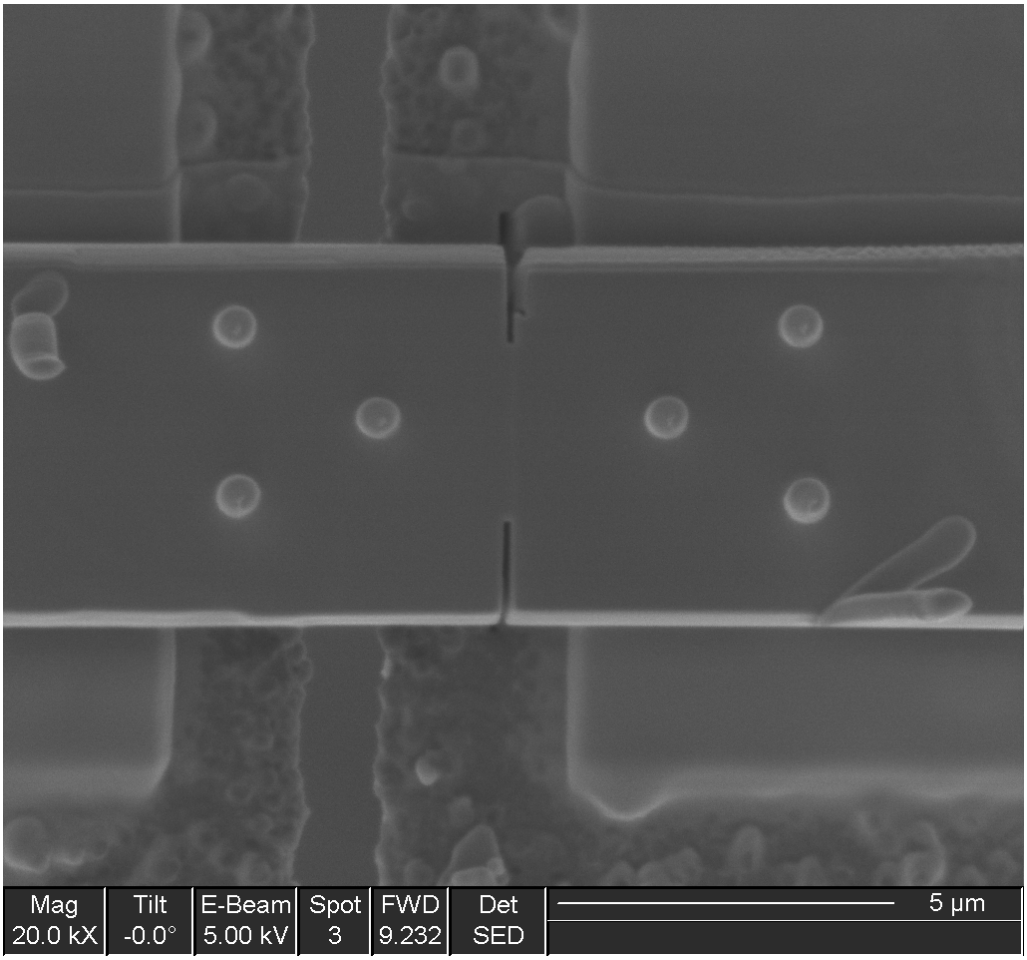

Fig. 34. DENT test specimen after notching at boundary and deposition of Pt-markers for DIC strain measurement.

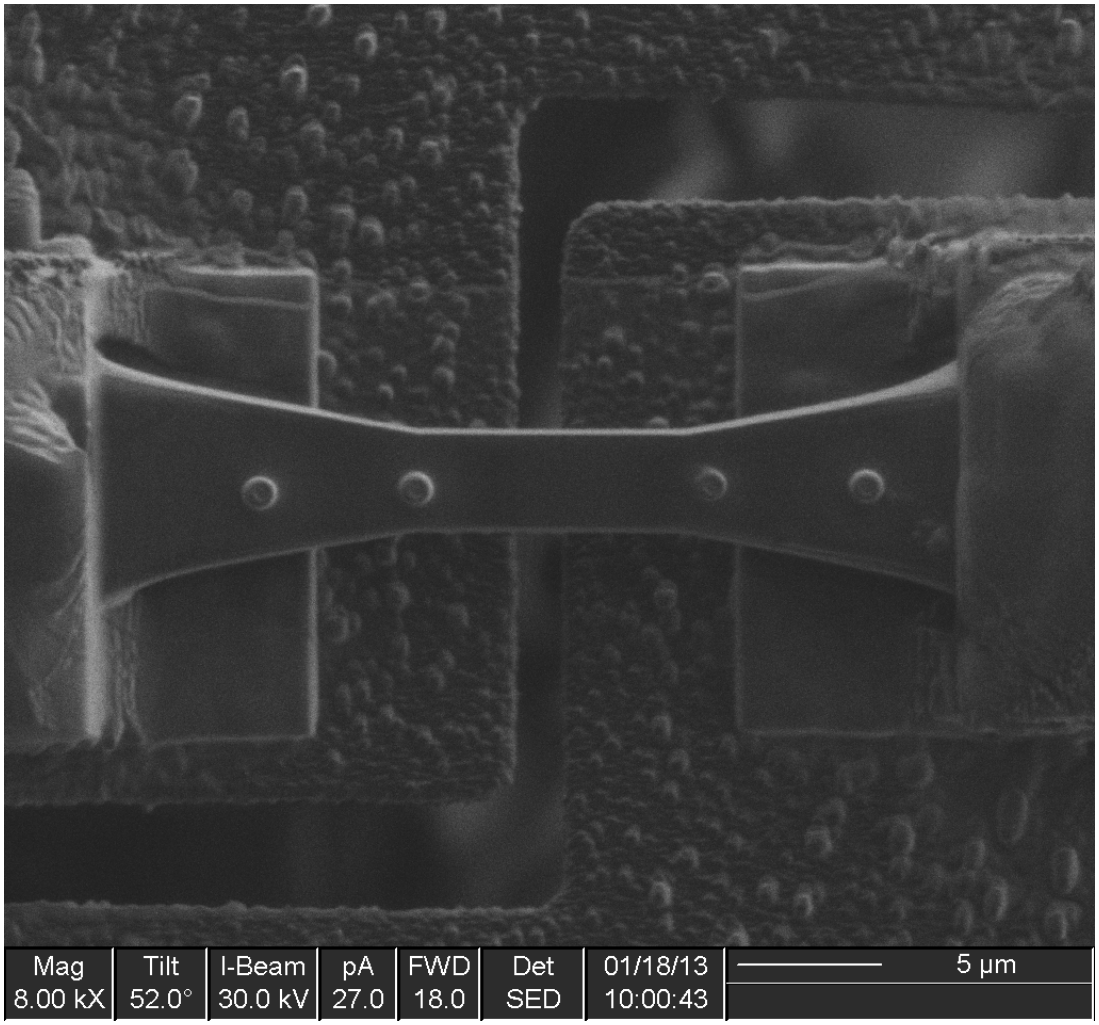

Fig. 35. Un-notched single crystal microtensile specimen after attaching to PTP device and deposition of Pt-markers.

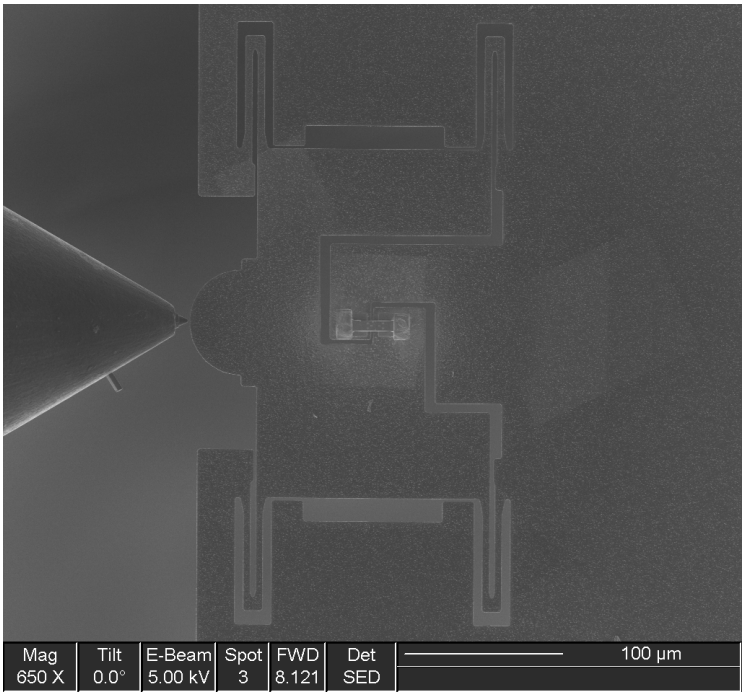

Fig. 36. Low magnification SEM image of PTP device with specimen attached and nanoindenter tip just out of contact with loading pad.

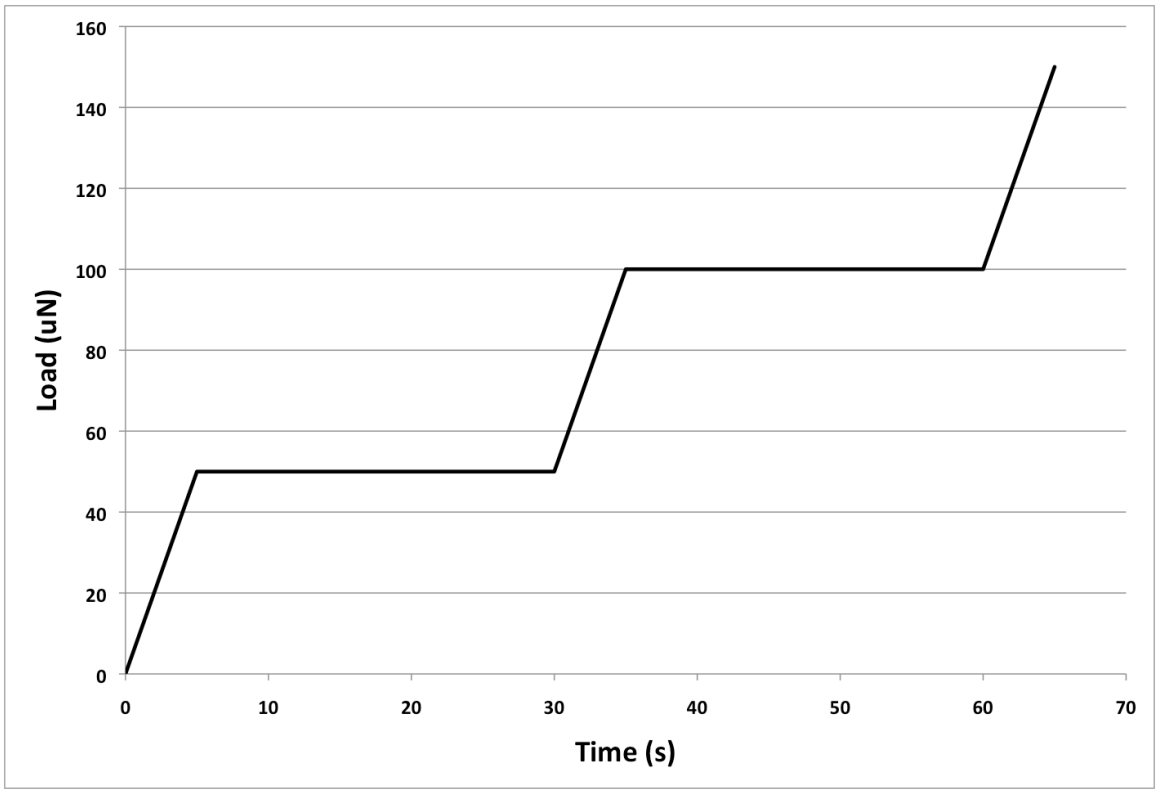

Fig. 37. Load schedule used in fracture tests. Note the built-in periodic holds so that high quality SEM images could be taken for DIC.

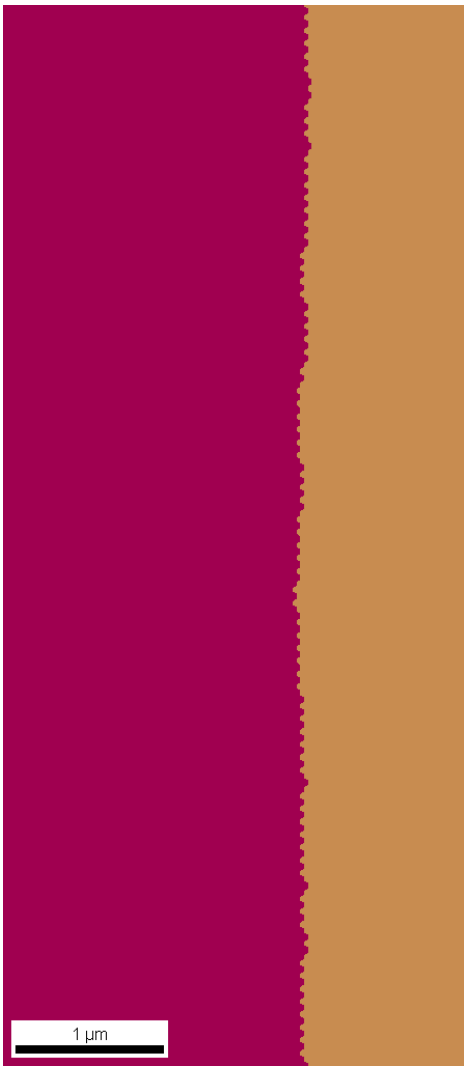

Fig. 38. EBSD map of bicrystal sample showing extremely straight boundary and no annealing twins.

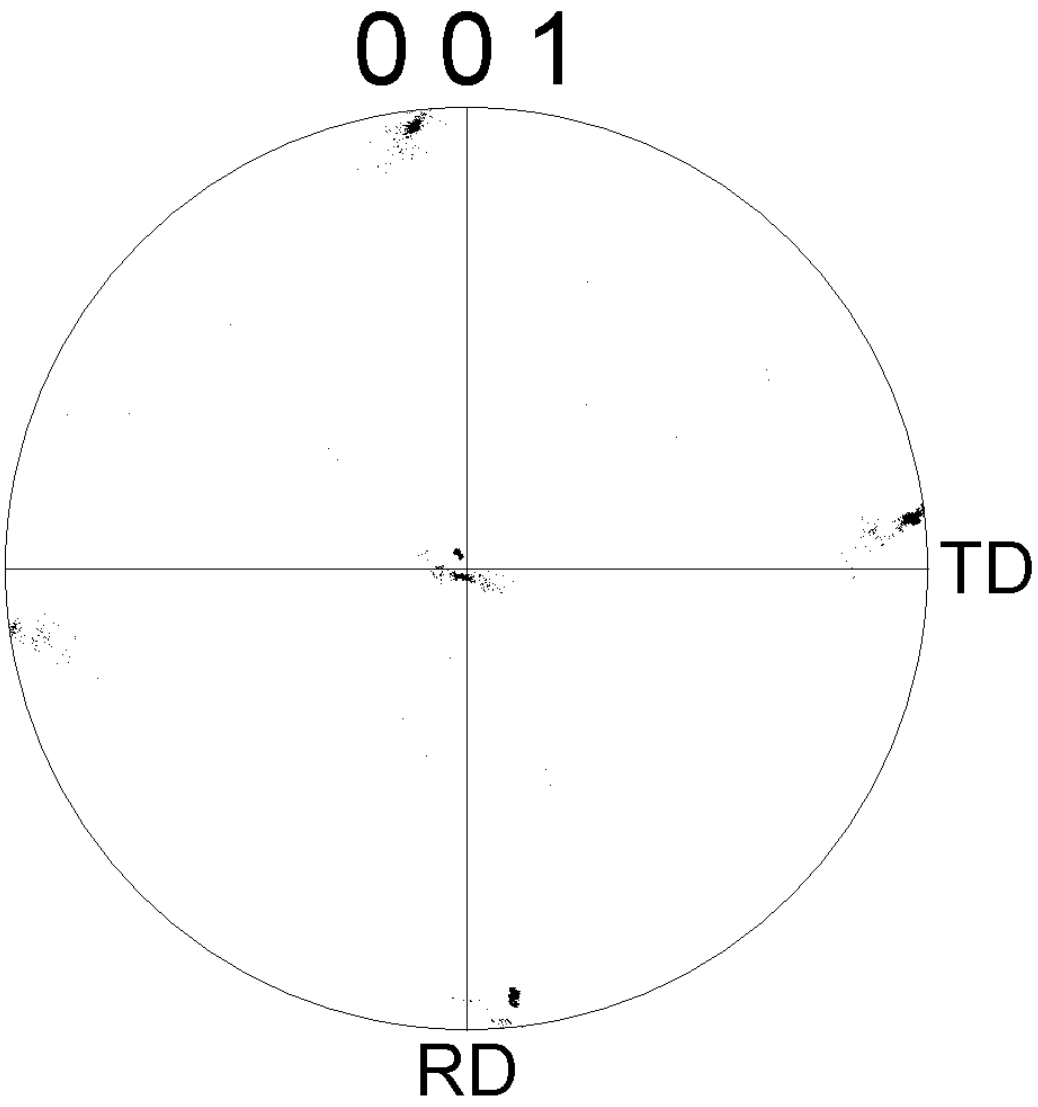

Fig. 39. Pole figure created from EBSD map of 6˚ boundary showing one common axis (twist axis) and a difference of 6˚ between center spots.

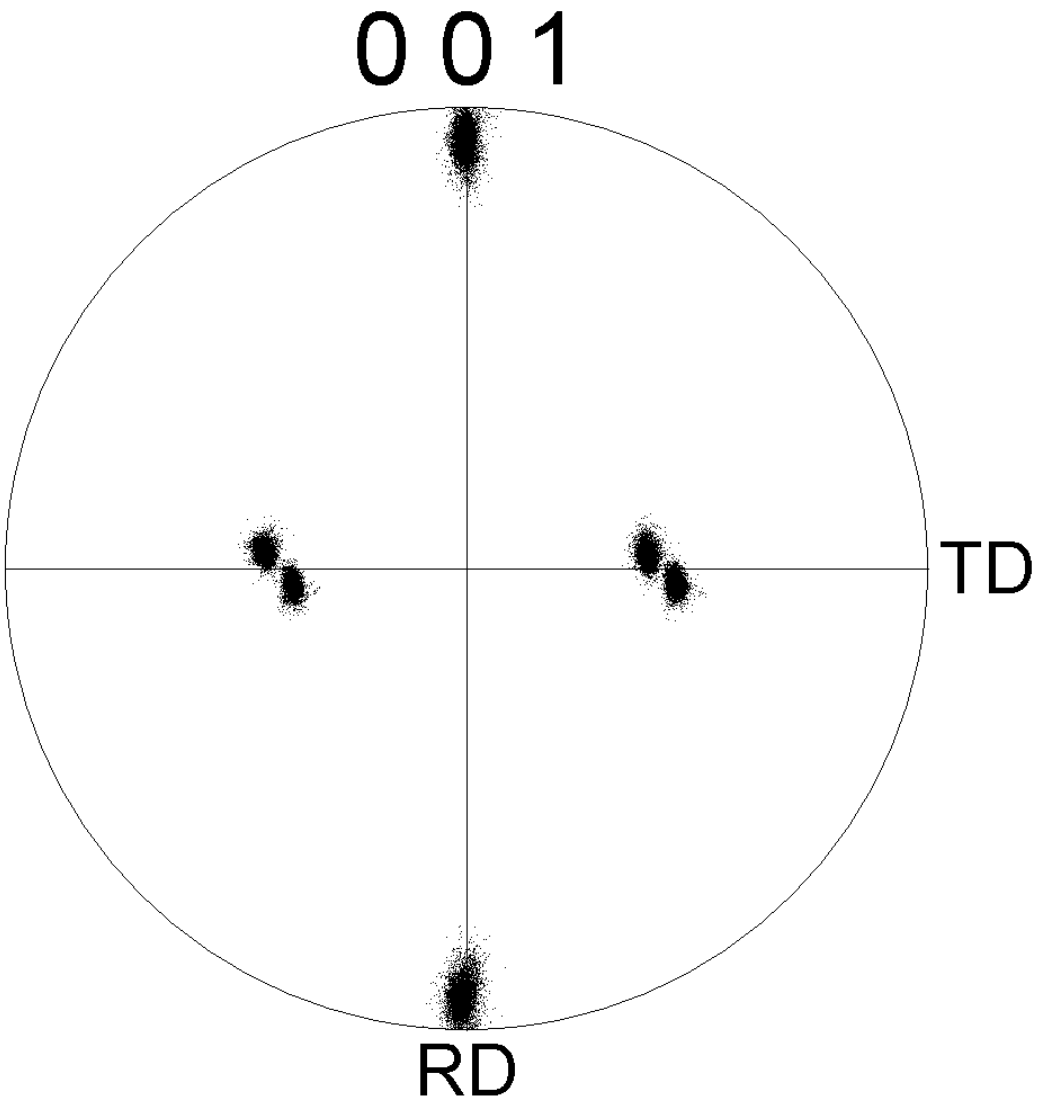

Fig. 40. Pole figure generated from EBSD map of 13˚ boundary showing one common axis (<001> twist) and 13˚ misorientation angle between other axes.

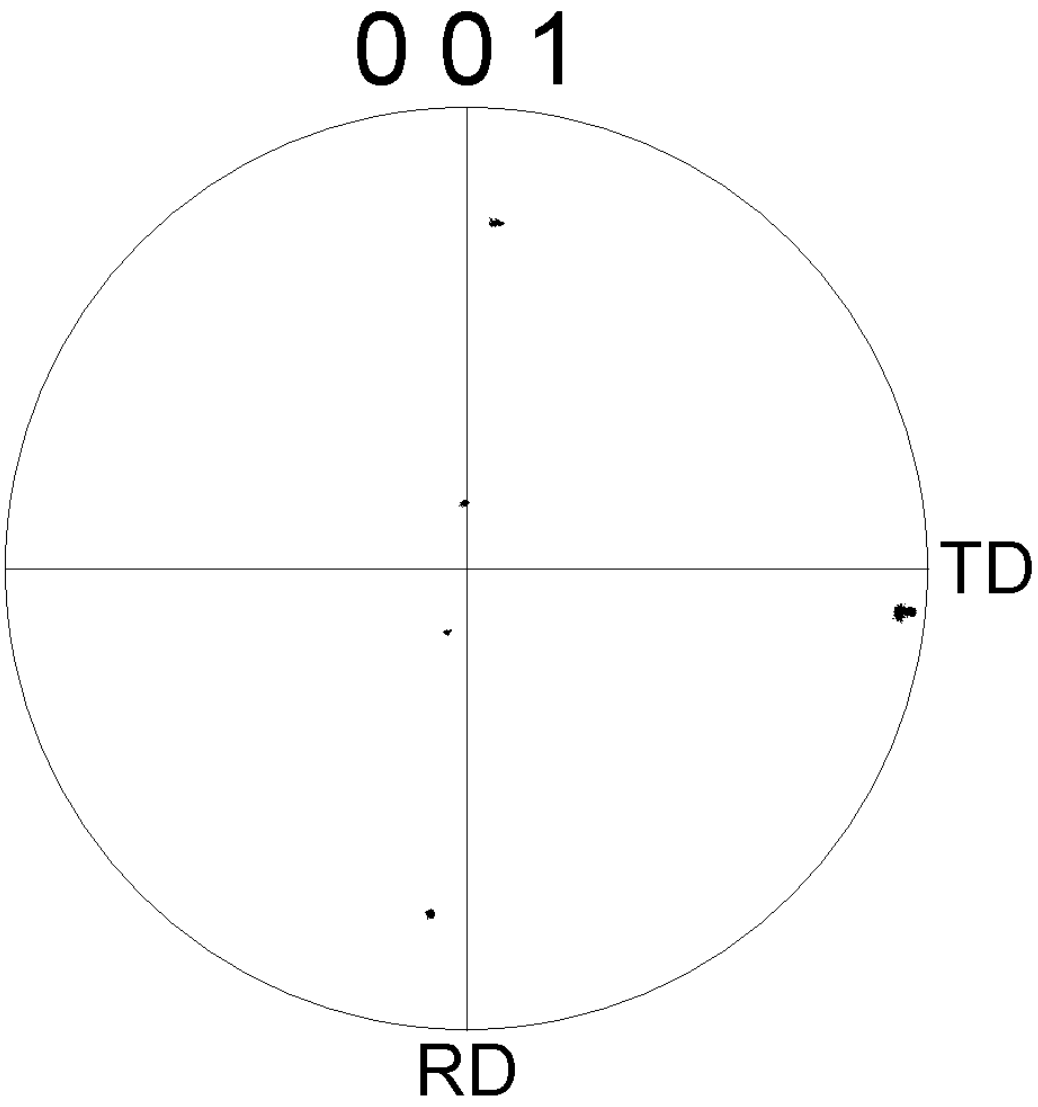

Fig. 41. Pole figure generated from 33˚ boundary showing one common axis (twist axis) and 33˚ misorientation between other axes.

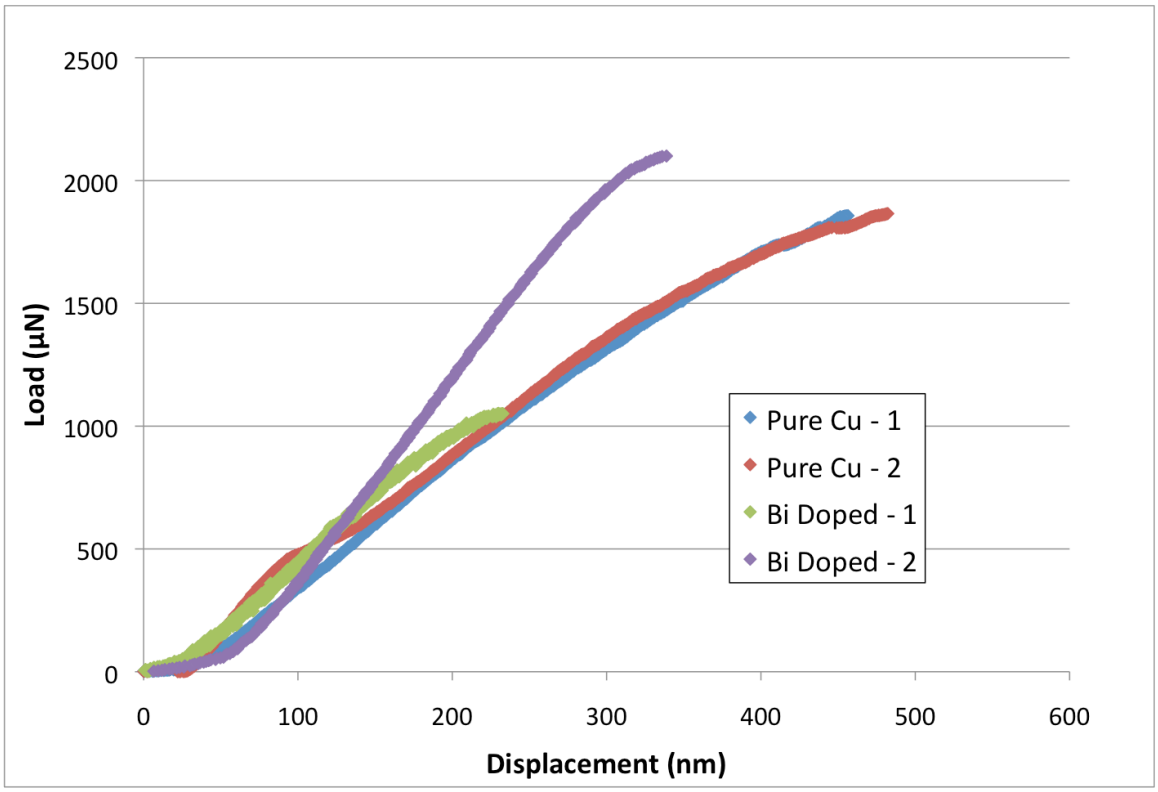

Fig. 42. Load-displacement curves generated from SENT testing of 13˚ boundary. In these tests, displacement was measured by the indenter transducer.

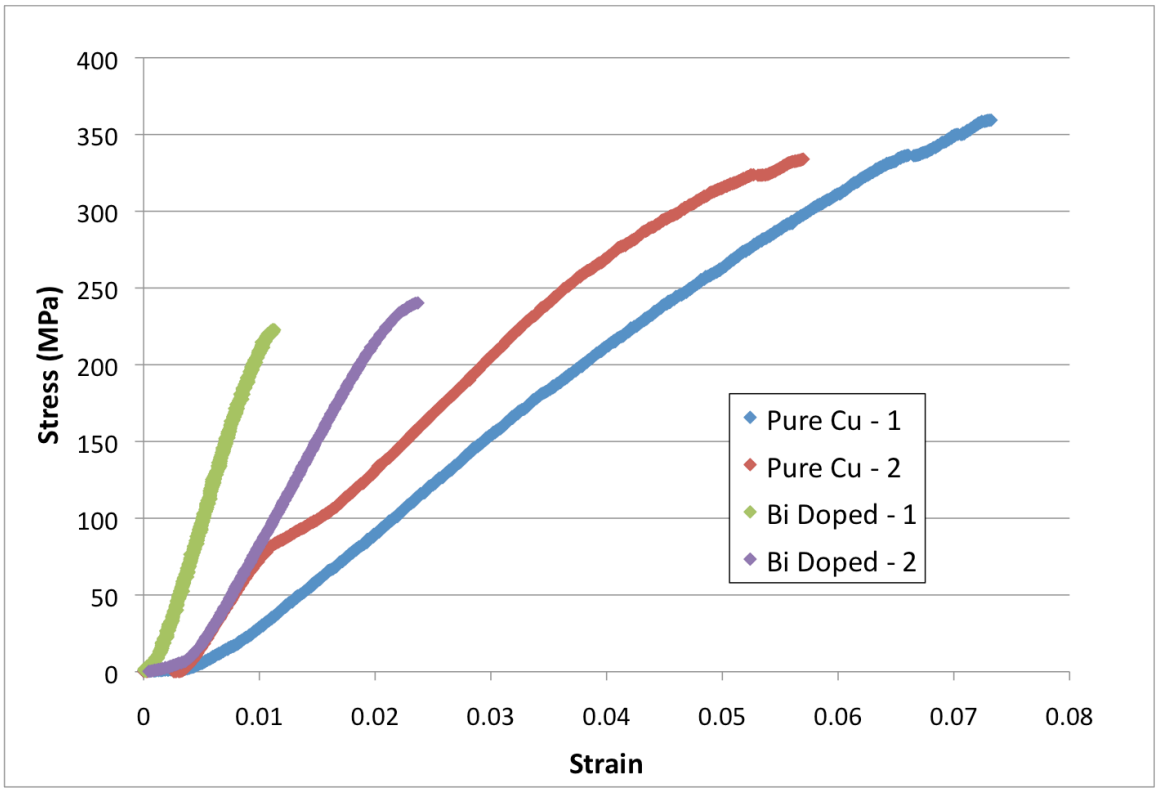

Fig. 43. Stress-strain curves generated from SENT testing of 13˚ boundary. Elastic slopes are neither consistent nor accurate, illustrating the need for direct strain measurement using DIC.

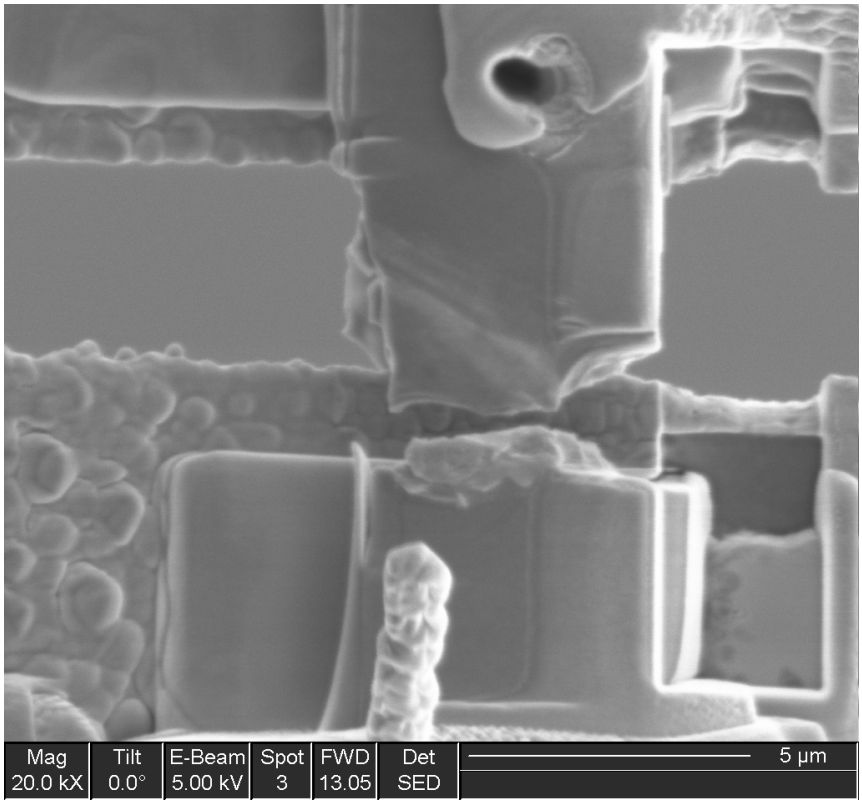

Fig. 44. Post-mortem SEM image of pure 13˚ SENT specimen showing transgranular fracture and evidence of significant plasticity.

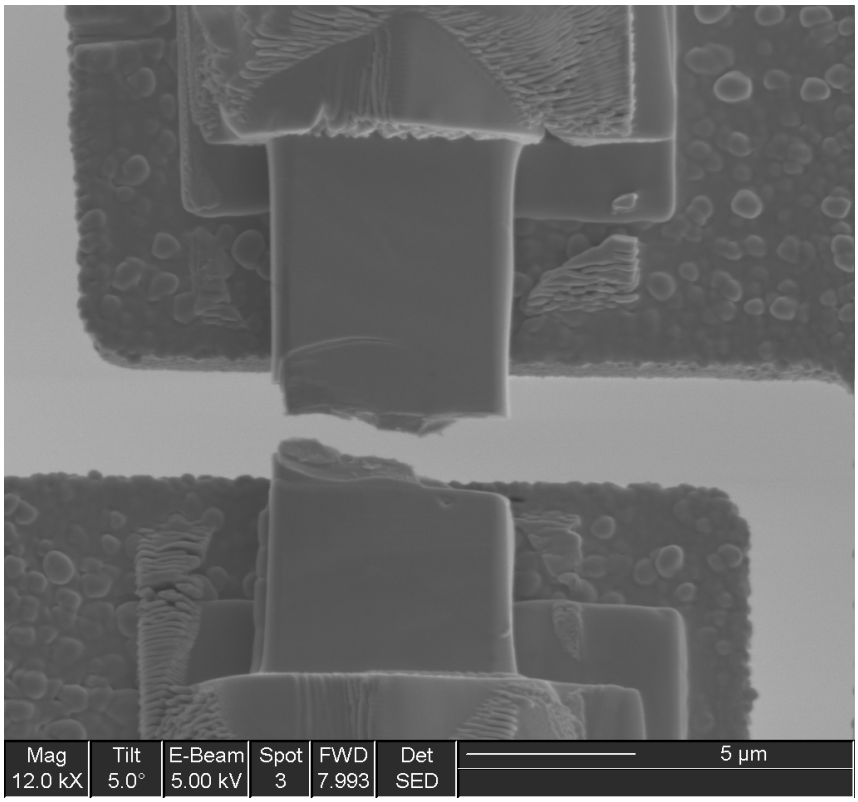

Fig. 45. Post-mortem SEM image of doped 13˚ specimen showing some evidence of plasticity and a nearly intergranular failure.

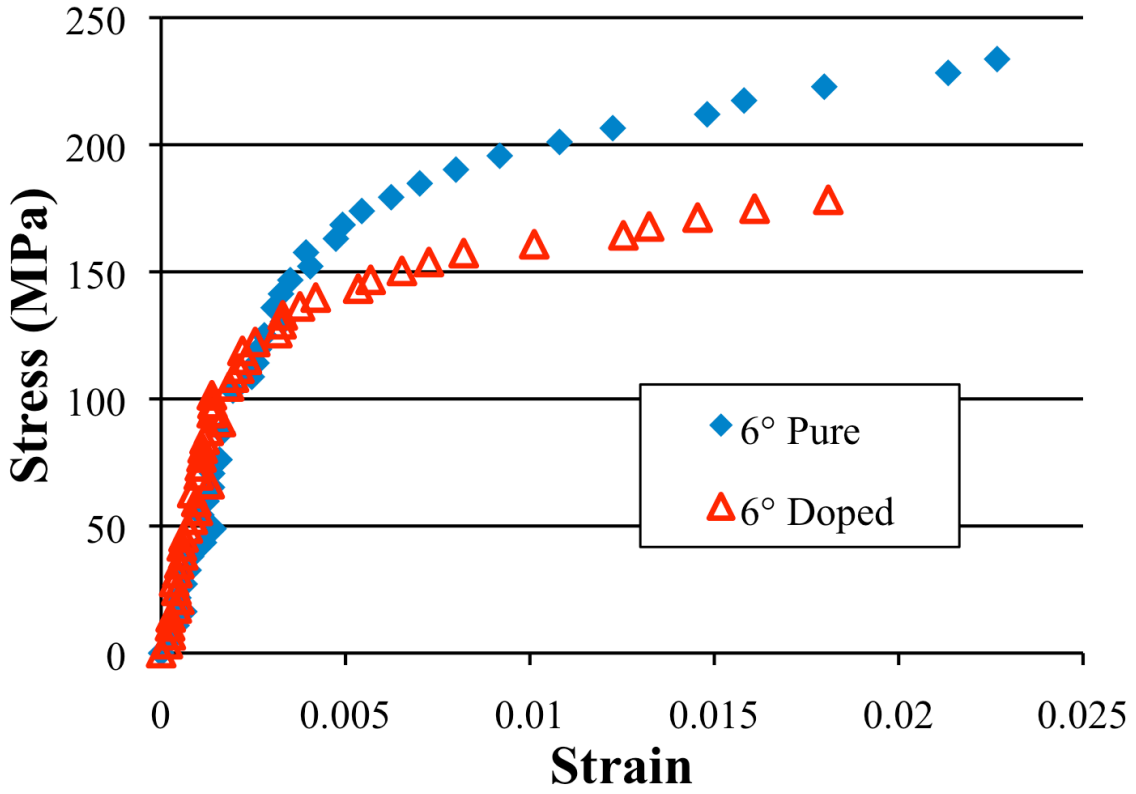

Fig. 46. Stress-strain curves generated from DENT testing of 6˚ boundary showing significant plasticity prior to failure in both specimen types.

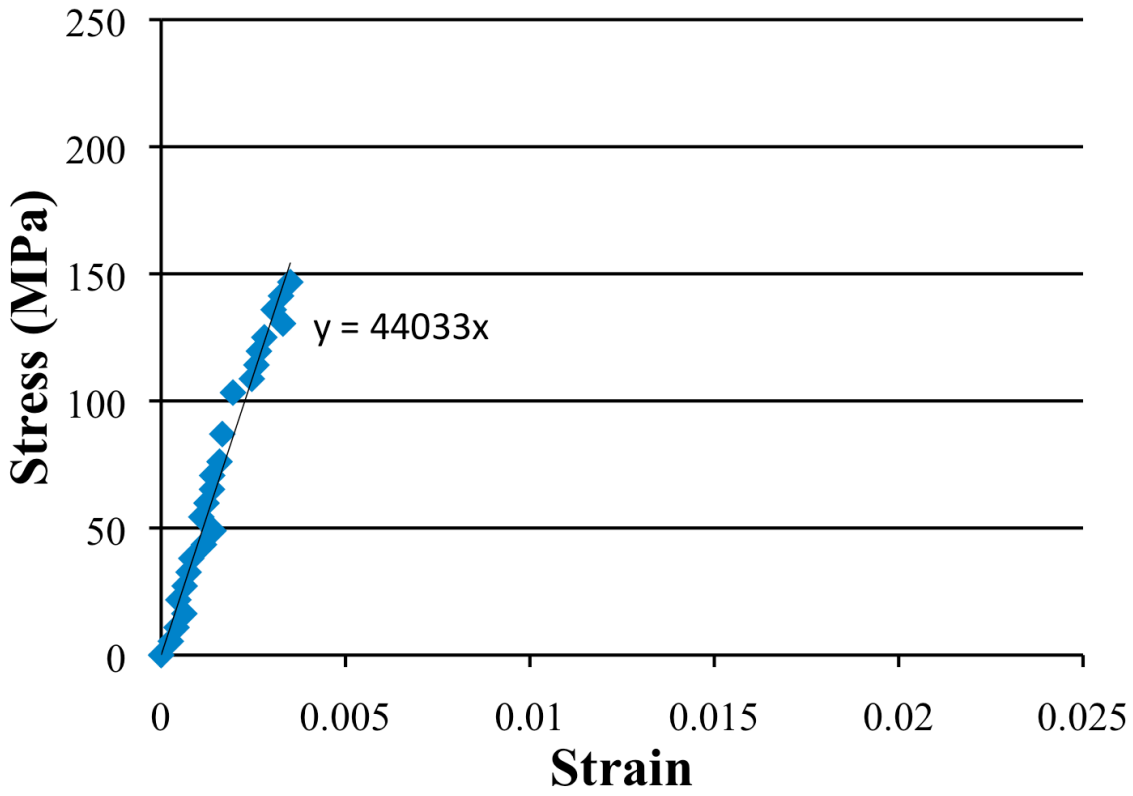

Fig. 47. Elastic region of stress-strain curve from 6˚ pure specimen showing a modulus of 44 GPa. This value is lower than the <100> modulus of Cu (66.7 GPa) due to the reduced cross-sectional area in between the notches.

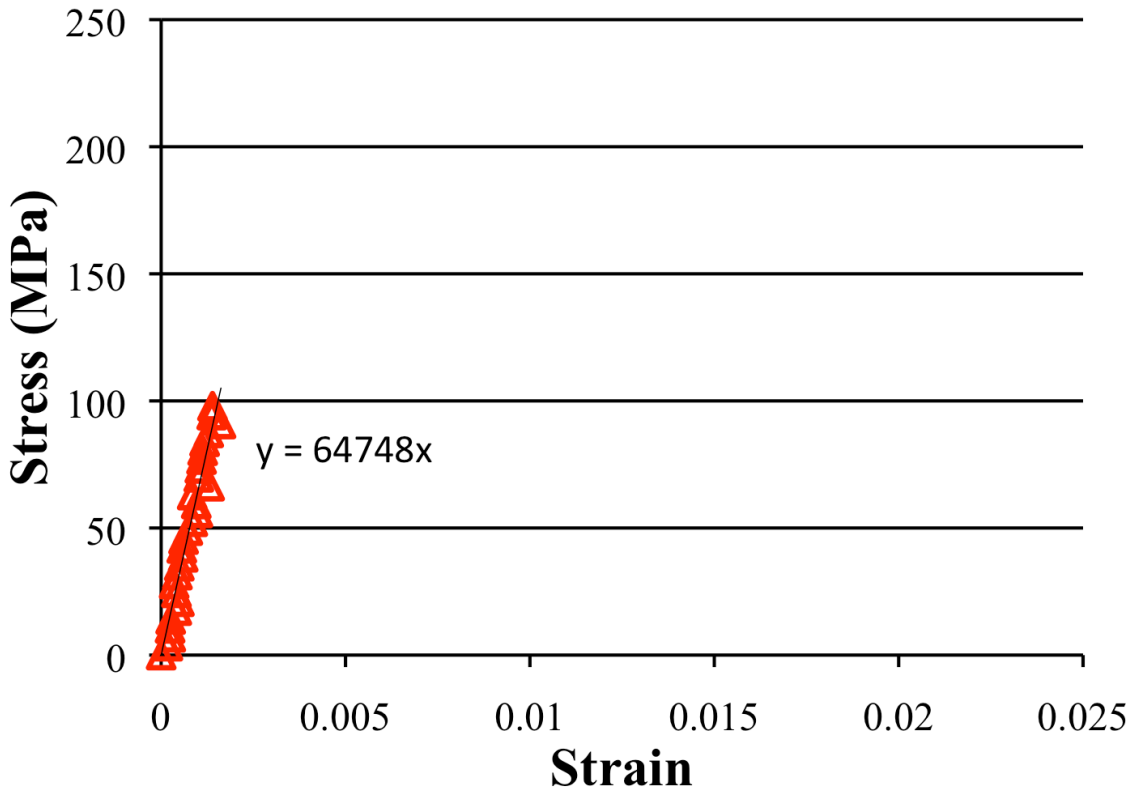

Fig. 48. Elastic region of stress-strain curve from 6˚ doped specimen showing a modulus of 64.8 GPa. This value is larger than that measured for the 6˚ pure specimen, but is still within an acceptable range of the anticipated value.

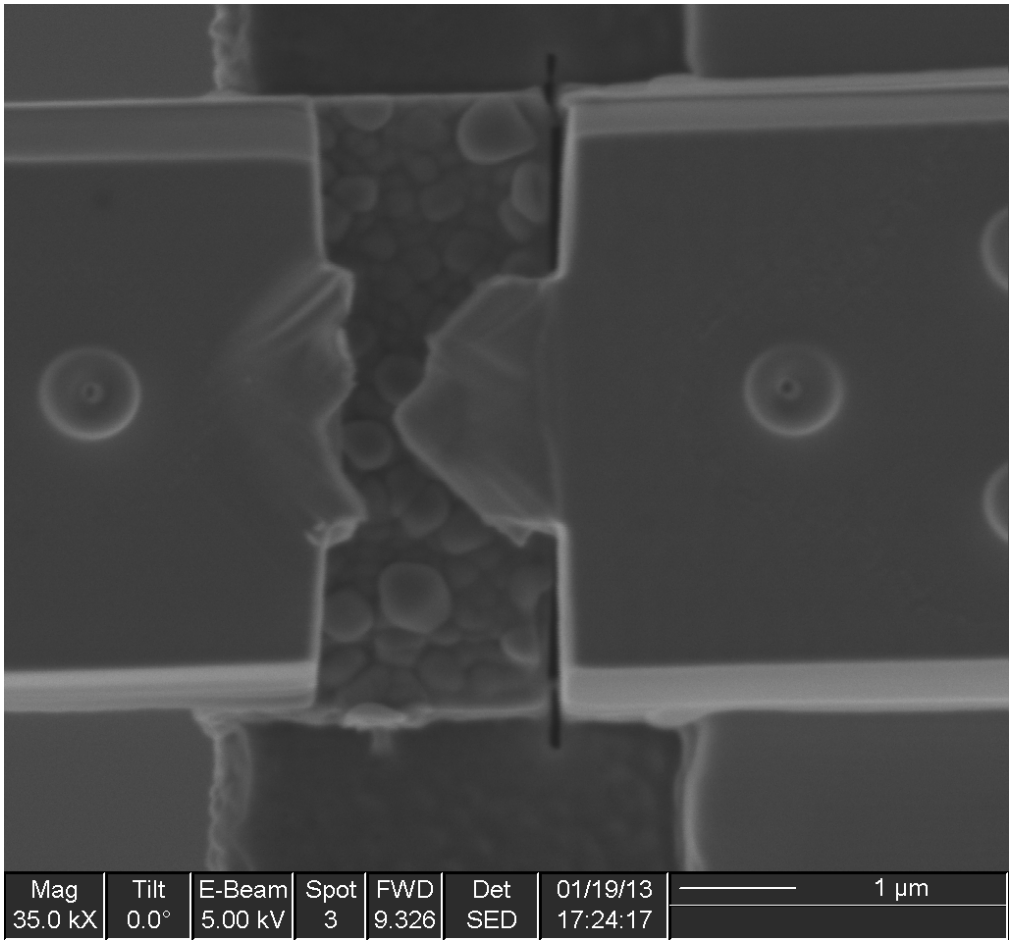

Fig. 49. Post-mortem SEM image of a 6˚ pure specimen showing a transgranular, shear-like failure.

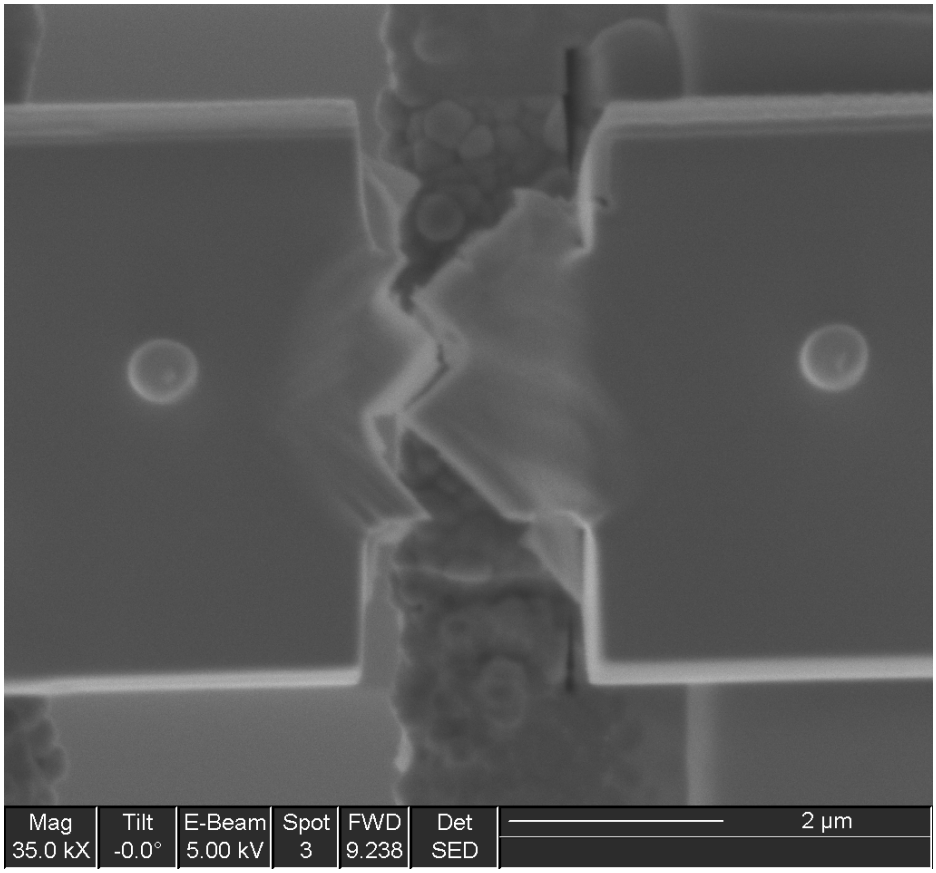

Fig. 50. Post-mortem SEM image of a doped 6˚ specimen showing a similar fracture morphology to the pure specimen in Fig. 49.

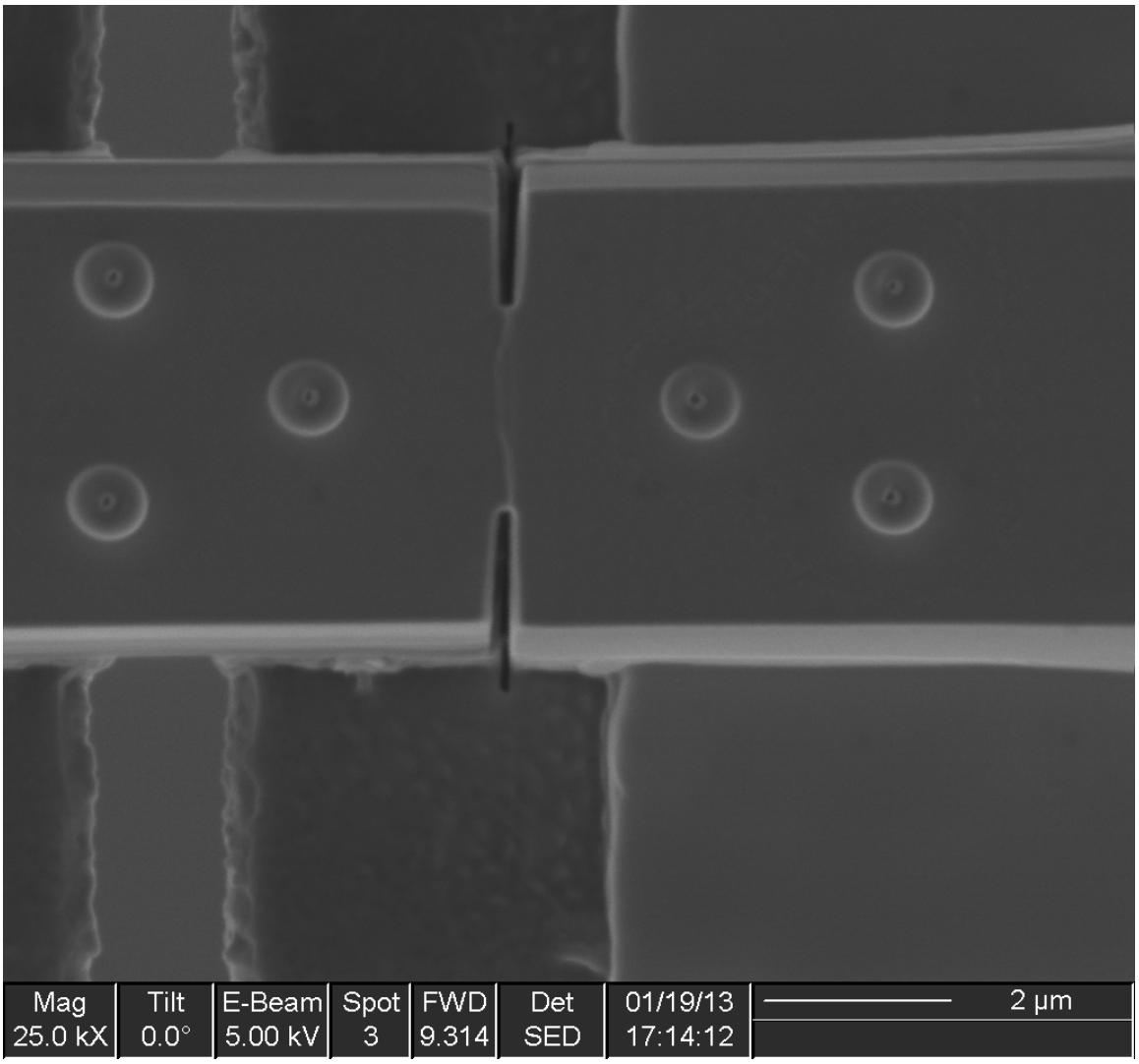

Fig. 51. SEM image acquired during testing of 6˚ pure specimen. Image represents the last data point on the stress-strain curve. Note that there are no slip steps present on the surface of the specimen yet, but some crack opening has occurred.

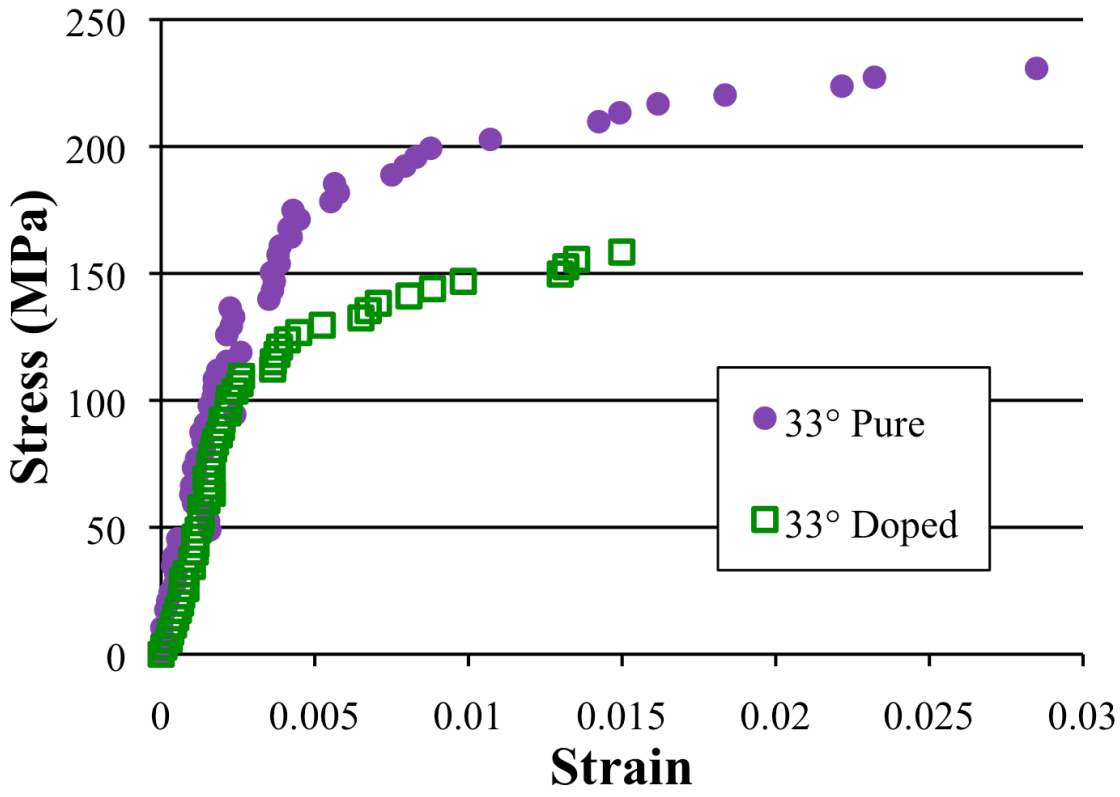

Fig. 52. Stress-strain curve generated from DENT testing of 33˚ boundary showing a lower fracture stress as well as lower fracture strain for doped specimens.

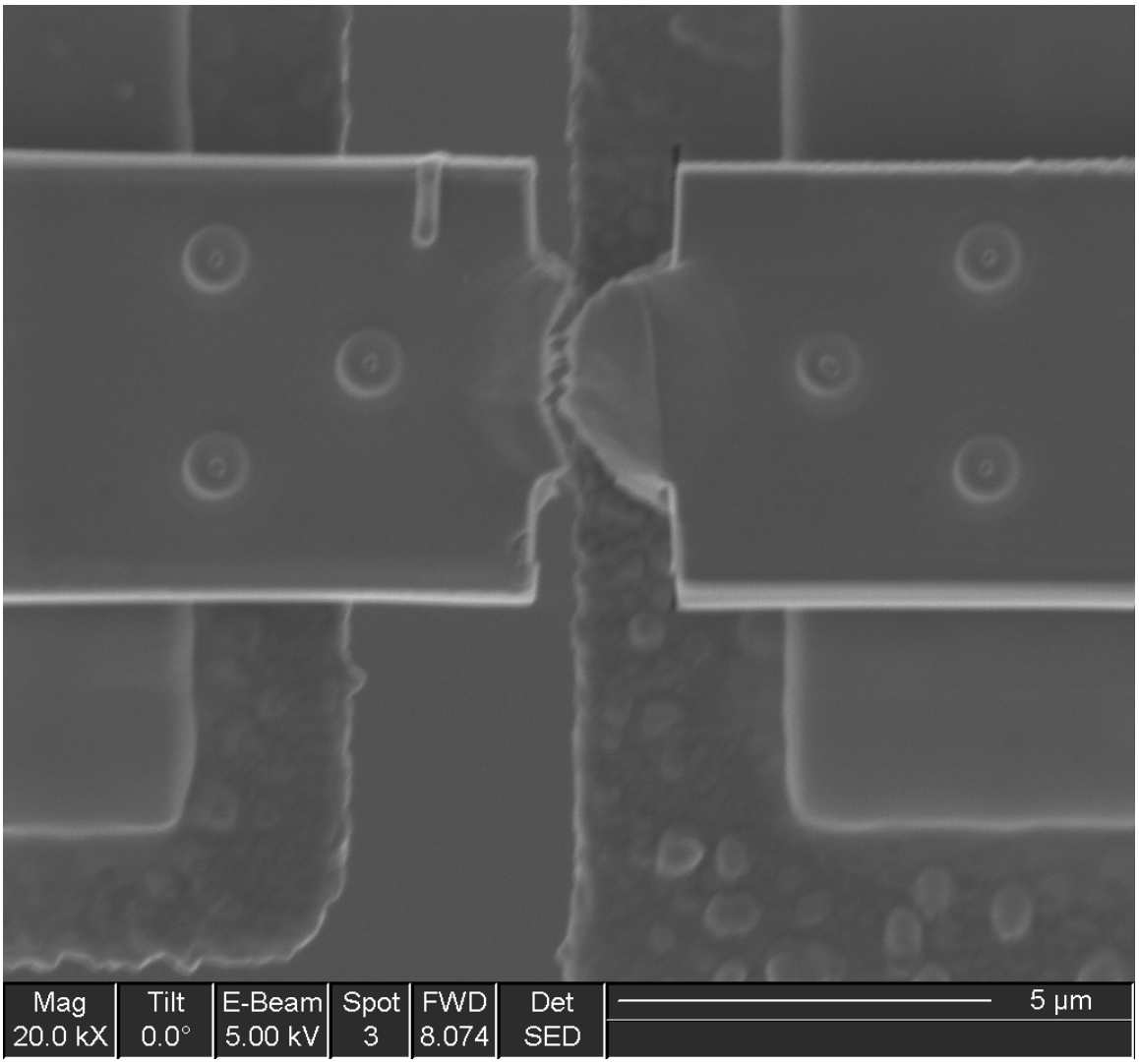

Fig. 53. Post-mortem SEM image of 33˚ pure DENT specimen showing transgranular, shear-like failure similar to that seen in 6˚ specimens.

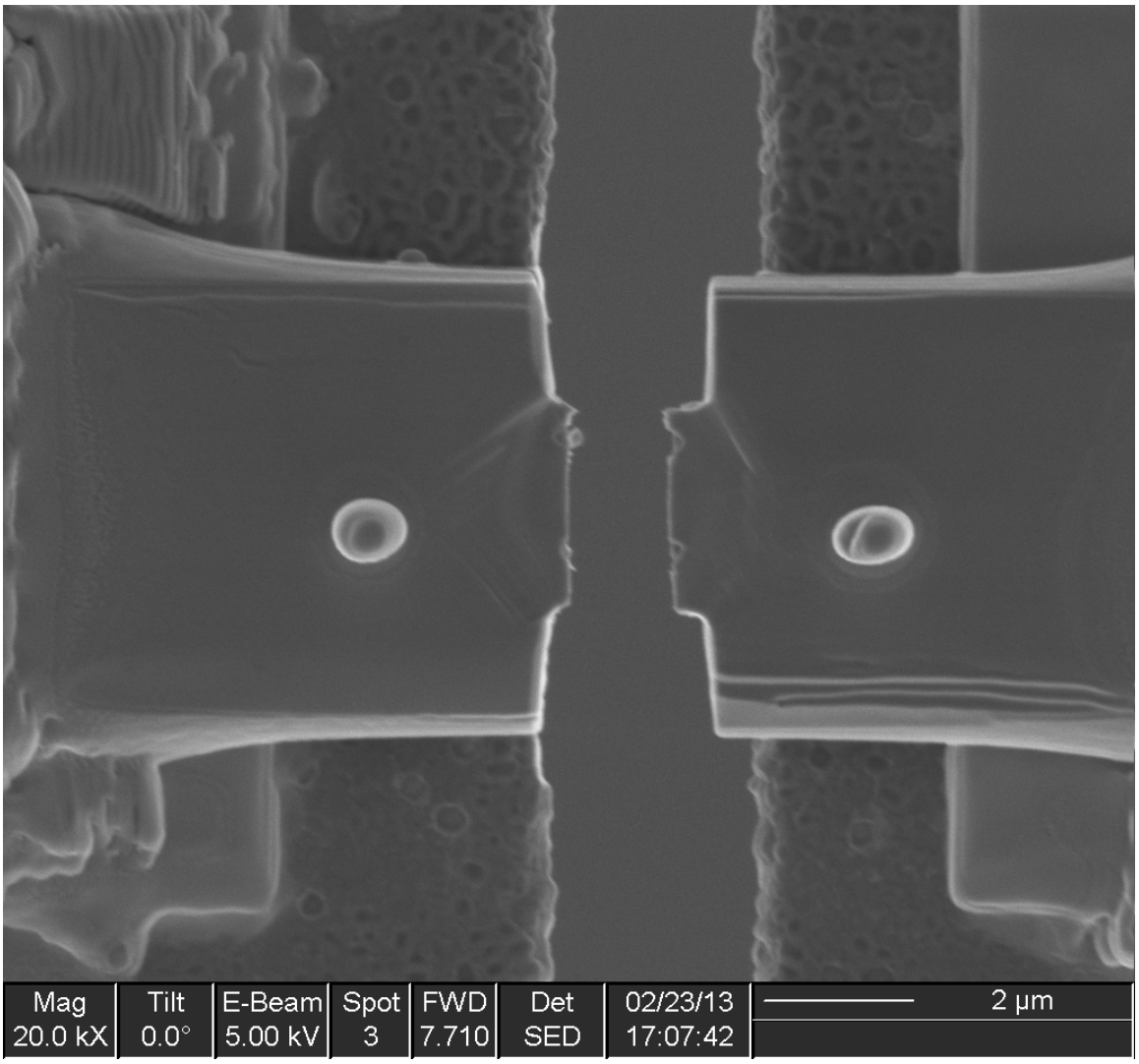

Fig. 54. Post-mortem SEM image of 33˚ doped DENT specimen showing clear intergranular fracture as well as significantly less evidence of plasticity, consistent with the stress-strain curve shown in Fig. 52.

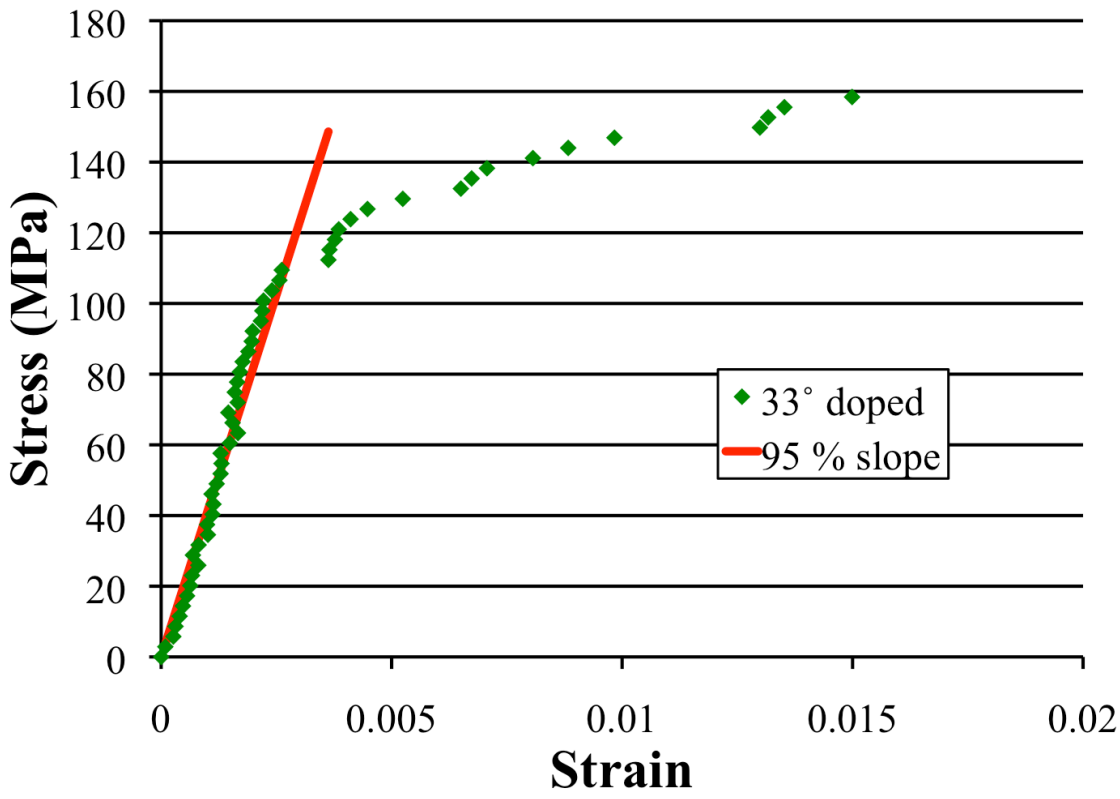

Fig. 55. Determination of validity of fracture toughness value for 33˚ doped specimen based on ASTM E399 specification[49].

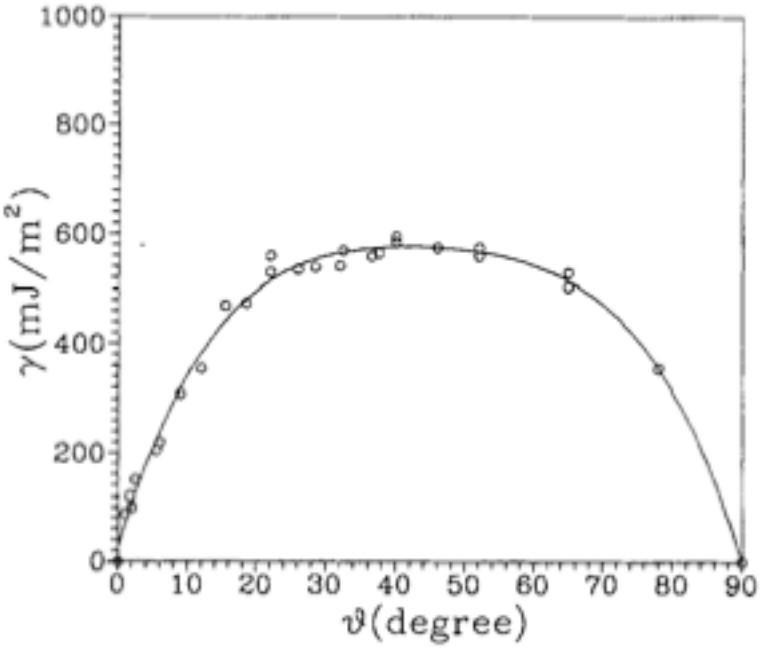

Fig. 56. Grain boundary energy as a function of misorientation angle for <001> tilt boundaries[31].

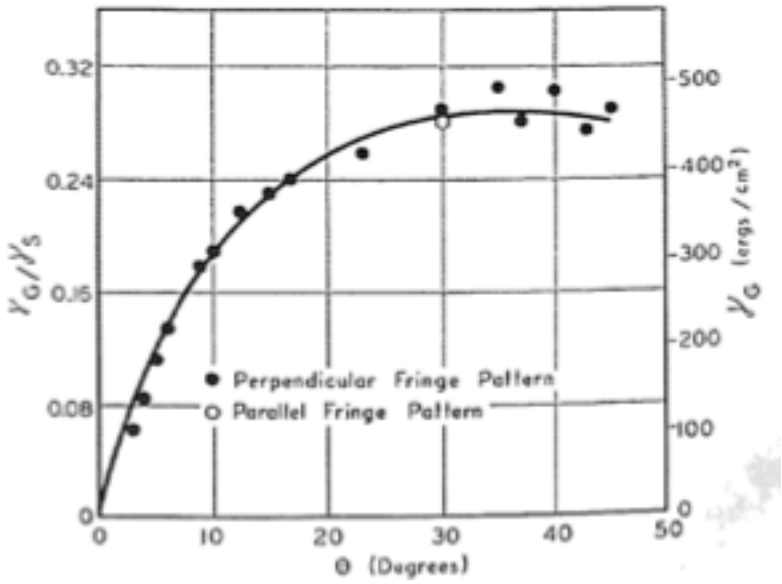

Fig. 57. Grain boundary energy as a function of misorientation angle for <001> twist boundaries[48].

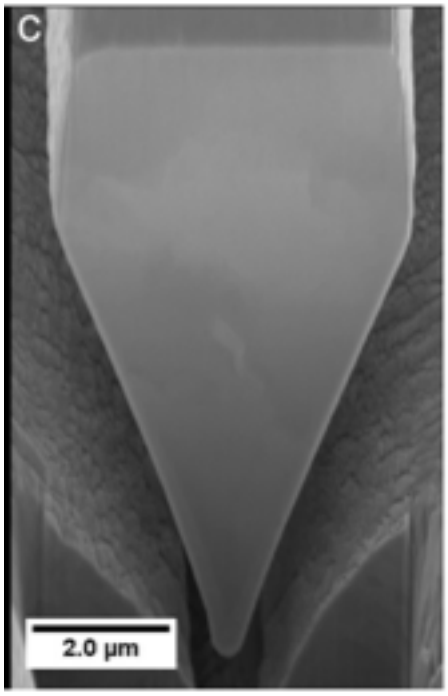

Fig. 58. End-on SEM image of microcantilever specimens used by Amrstrong *et al.*[35].

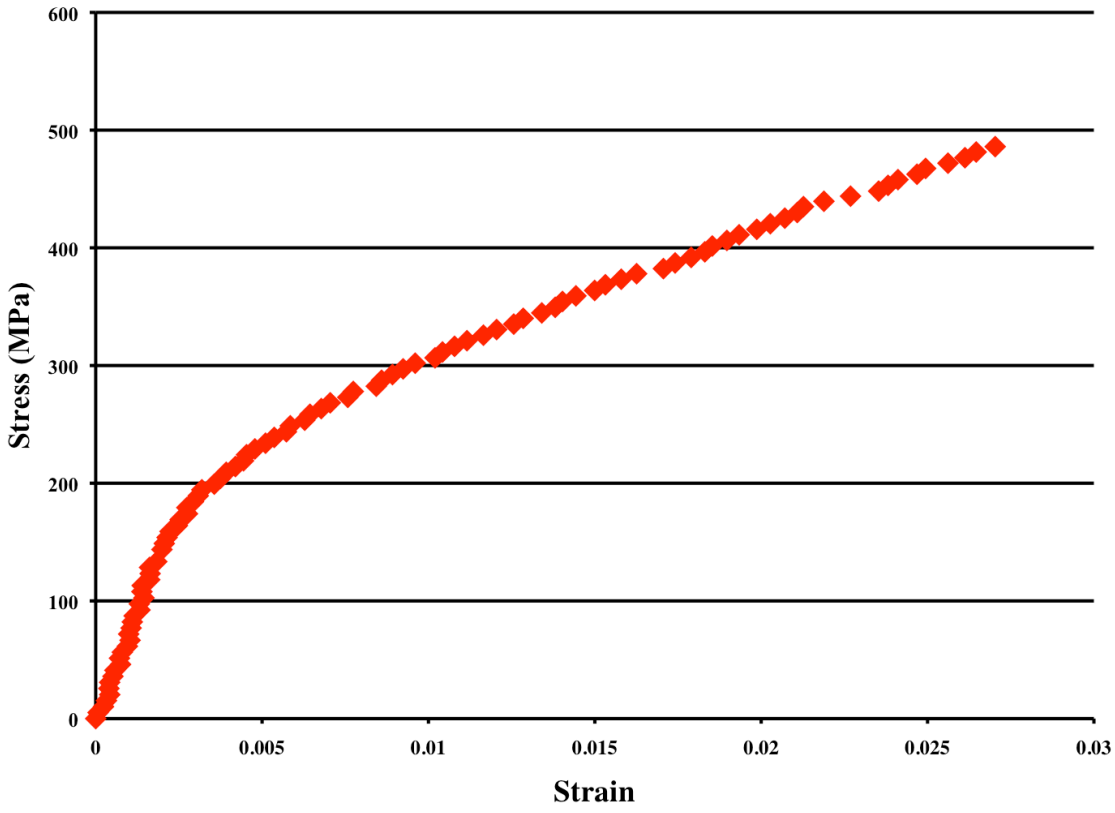

Fig. 59. Stress-strain curve generated from single-crystal bowtie micro-tensile specimen.

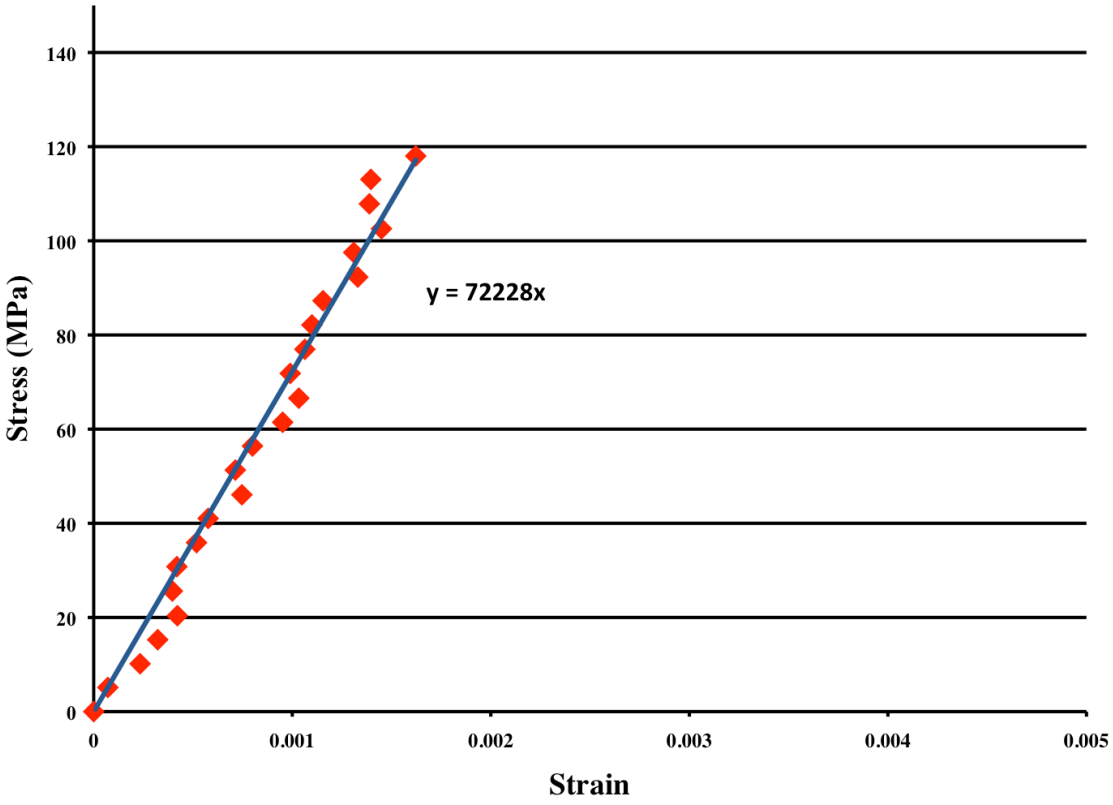

Fig. 60. Linear fit to elastic portion of curve in Fig. 59 showing a modulus of 72.2 GPa, which is in fairly good agreement with the expected <100> modulus of Cu (66.7 GPa).

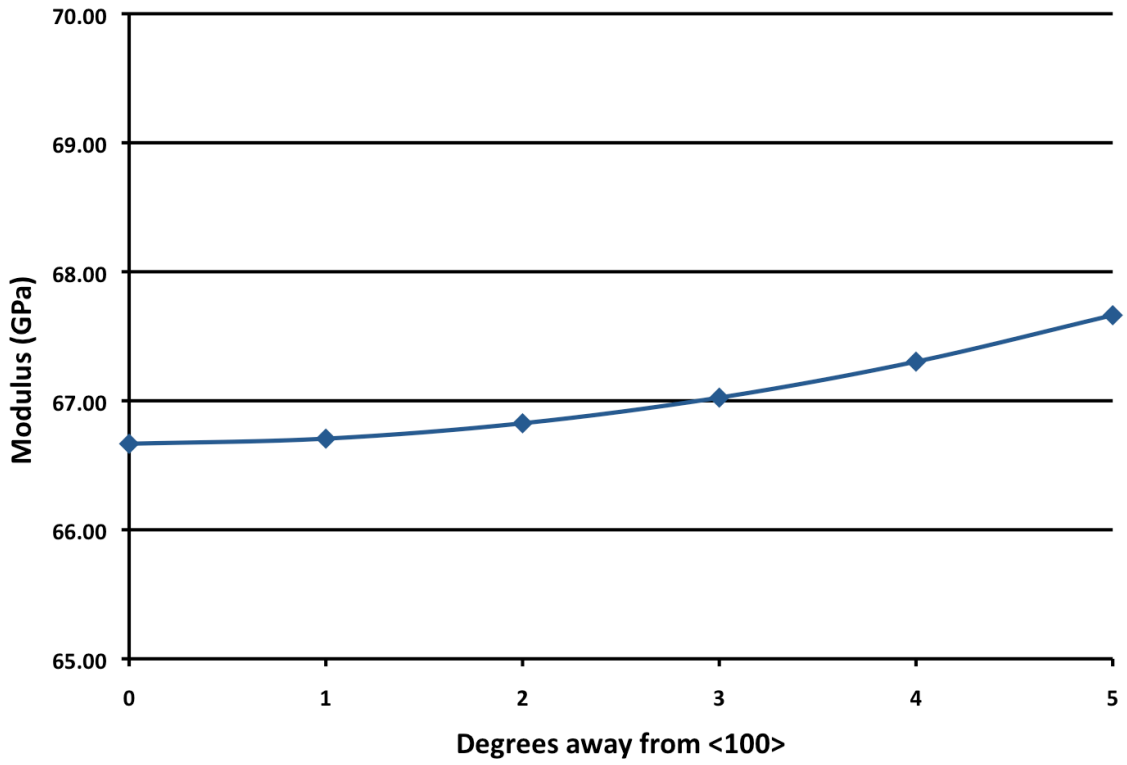

Fig. 61. Elastic modulus of Cu vs. misorientation from <100> direction. The fact the modulus stays fairly constant over this range means that slight misalignment of actual test specimens relative to the boundary is tolerable.

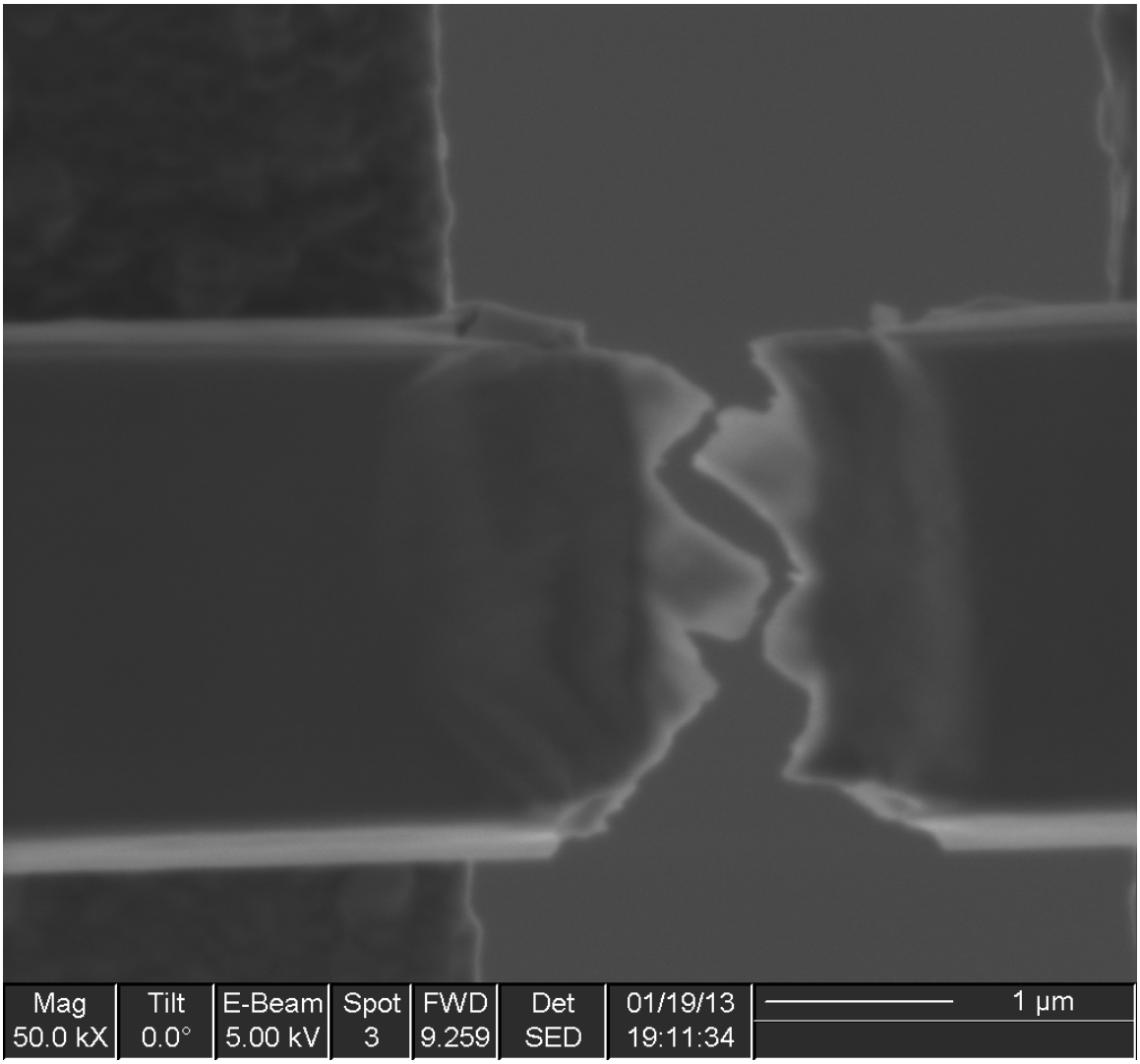

Fig. 62. Post-mortem SEM image of single-crystal specimen showing similar shear-like appearance to pure bicrystal specimens.

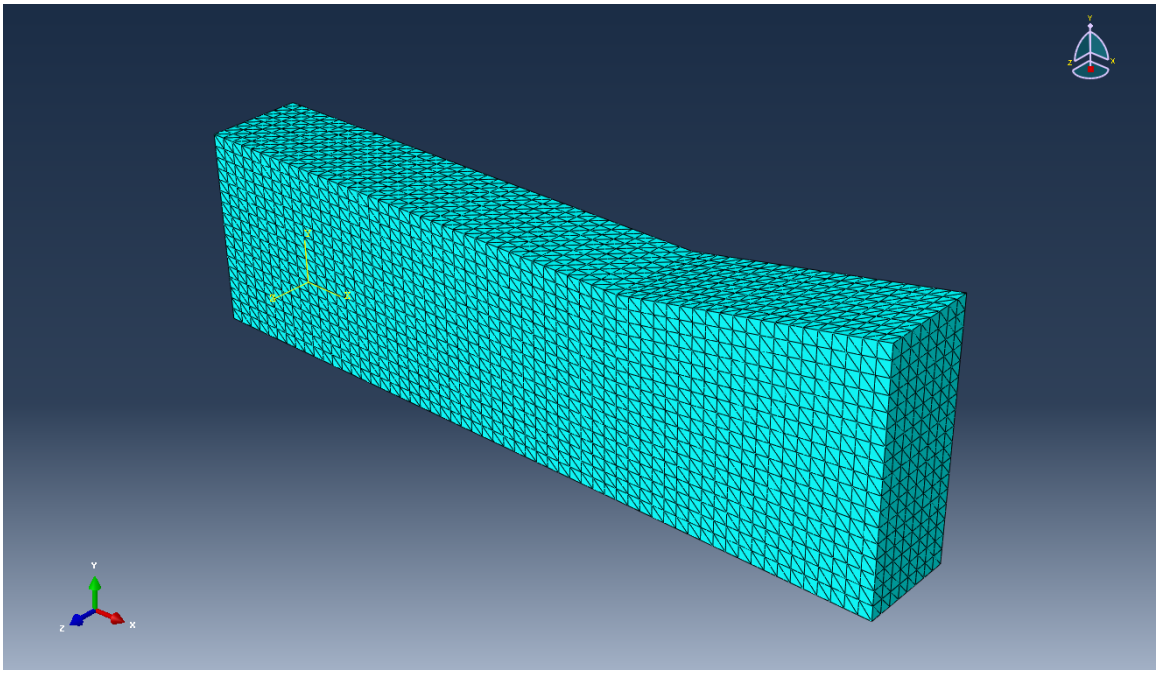

Fig. 63. FEM model of single-crystal bowtie specimen showing part geometry and mesh. The model depicts $1/8^{th}$ of the actual specimen and takes advantage of symmetry contraints during the analysis.

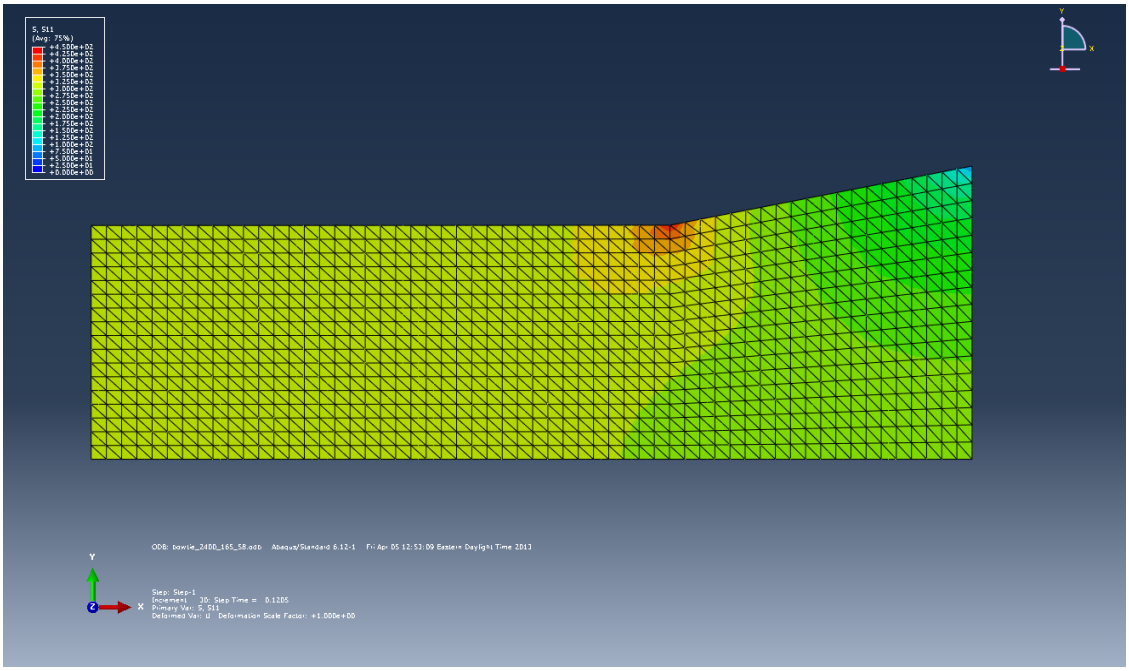

Fig. 64. Uniaxial stress from FEM simulation of single-crystal bowtie specimen showing uniform stress in most of gauge section, with a slight stress concentration at the transition point.

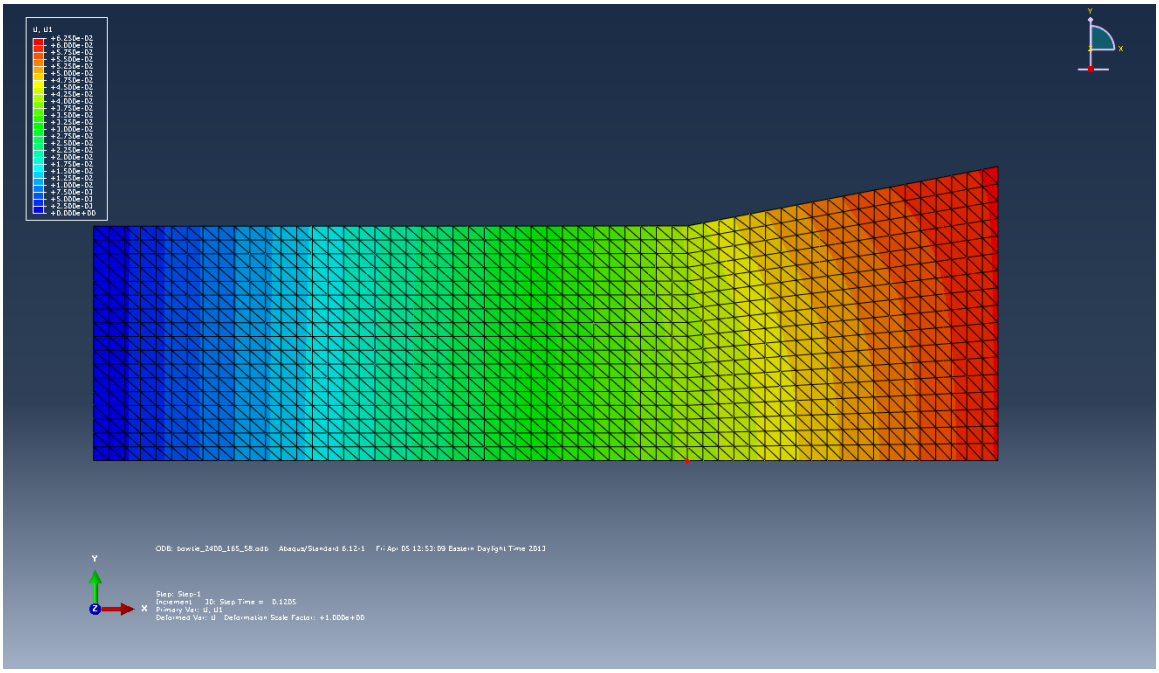

Fig. 65. Uniaxial displacement of single-crystal bowtie specimen showing 0 displacement at center of specimen (defined as fixed in model). Also shown is the node used for calculation of strain (identified by red dot on bottom edge of part).

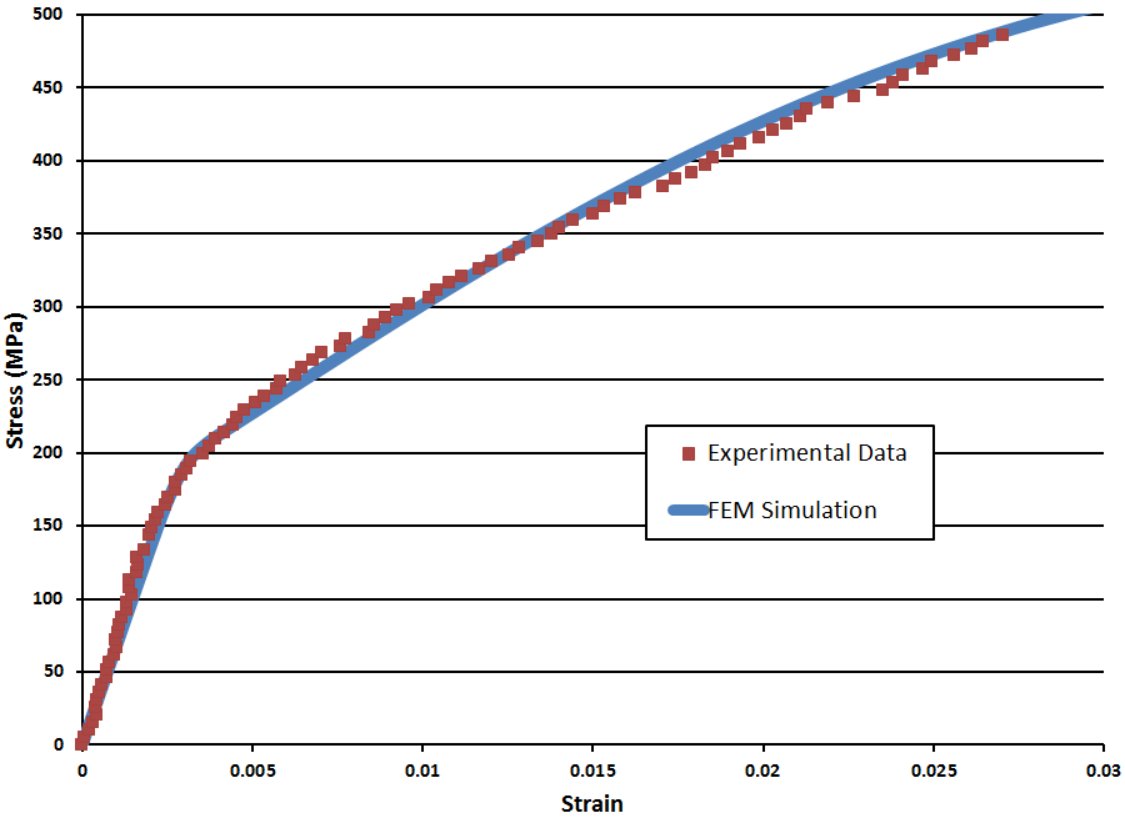

Fig. 66. Stress-strain curve showing good fit between FEM simulation and experimental data from single-crystal bowtie specimen. Simulation uses hardening parameters listed in Table 4.

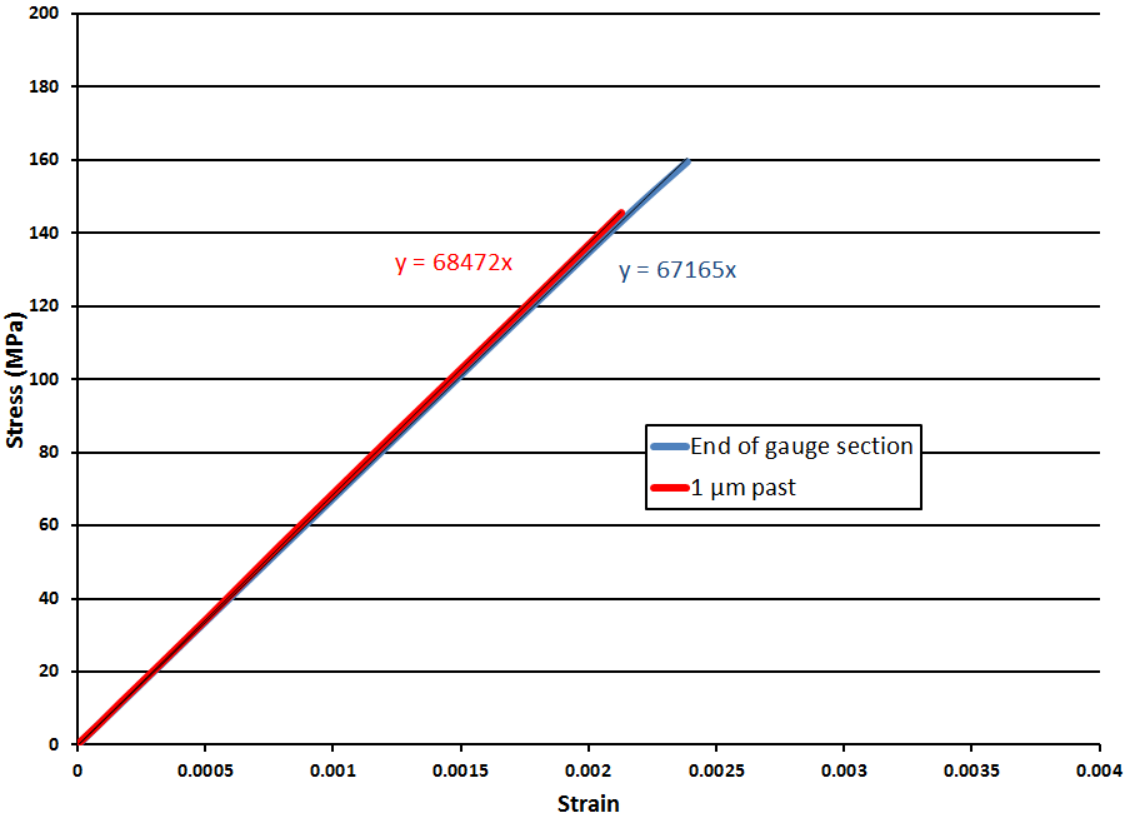

Fig. 67. Elastic portions of stress-strain curves generated from FEM simulations of single-crystal specimen using different nodes for strain calculation. Blue curve used the point described before at the end of the gauge section. The red curve used a node that was ~1 µm past the end of the gauge section. The very similar slopes of these curves suggests that the exact location of the Pt markers on the actual test specimens is not crucial.

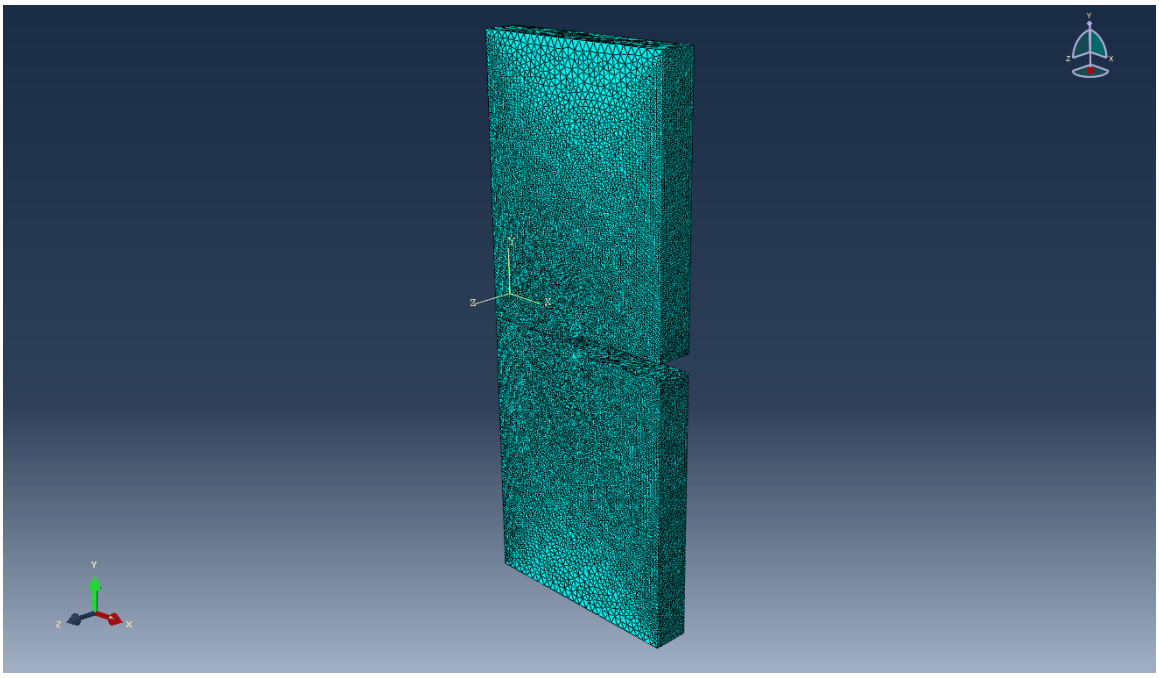

Fig. 68. FEM model of bicrystal DENT specimen utilizing quarter-symmetry (mirror planes in width and thickness dimensions). Note that the mesh is significantly finer in the vicinity of the notch.

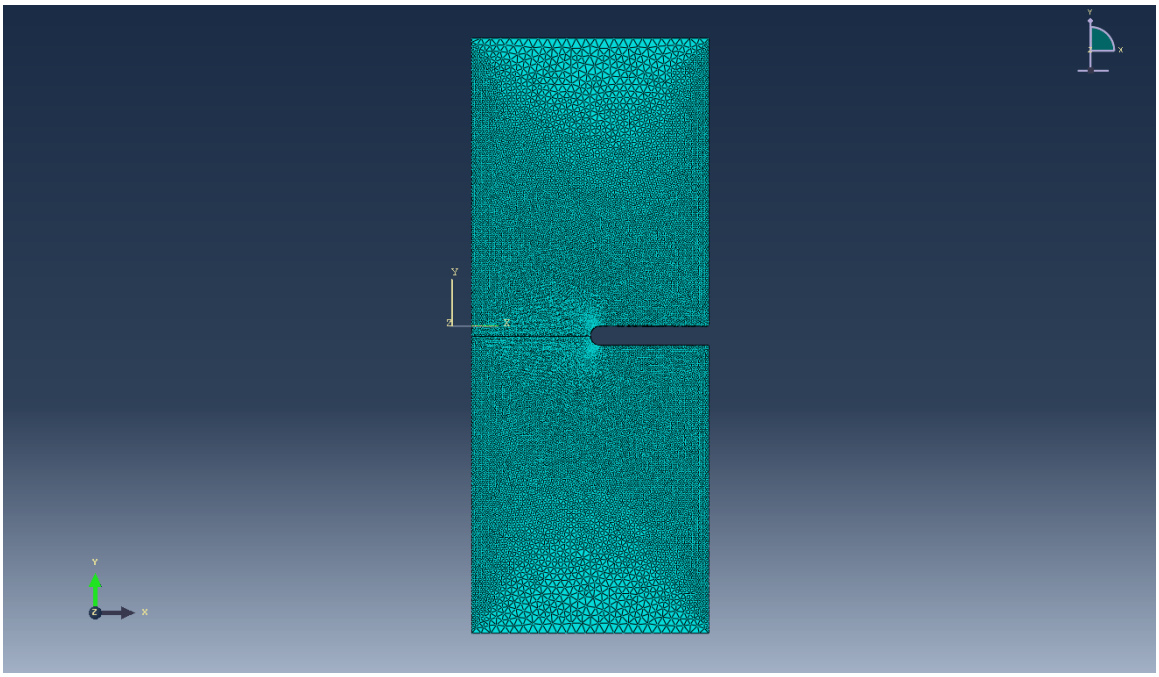

Fig. 69. 2-D image of bicrystal DENT FEM model showing finer mesh near notch.

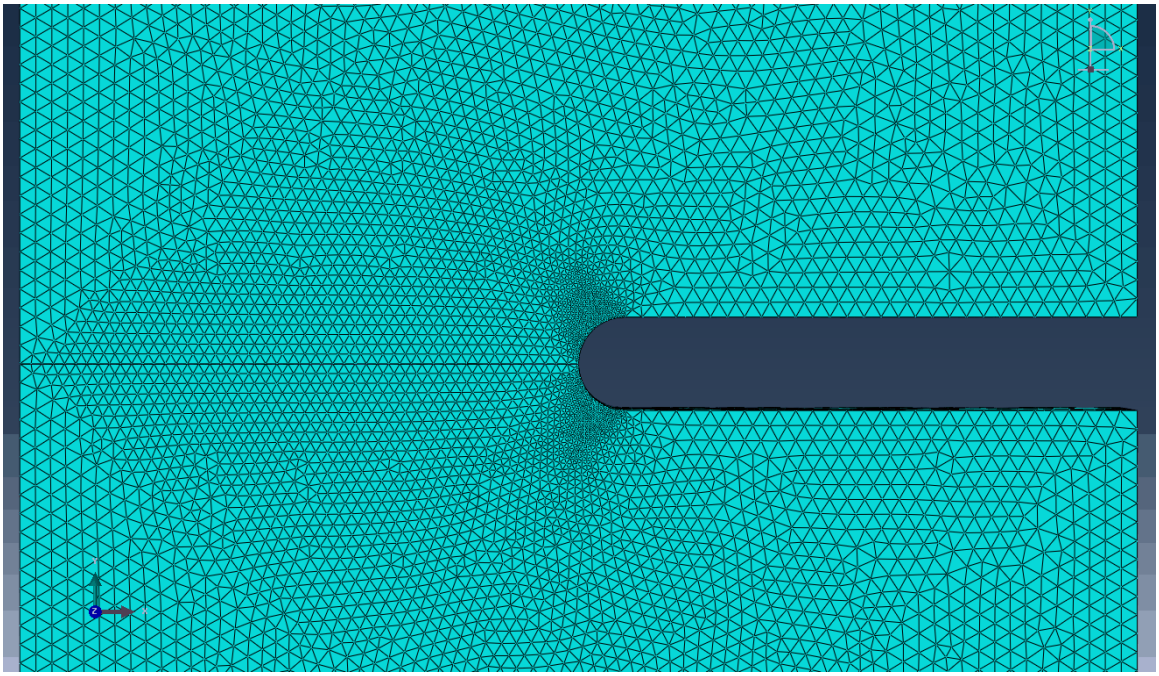

Fig. 70. Zoomed in view of mesh near the notch of bicrystal DENT FEM model.

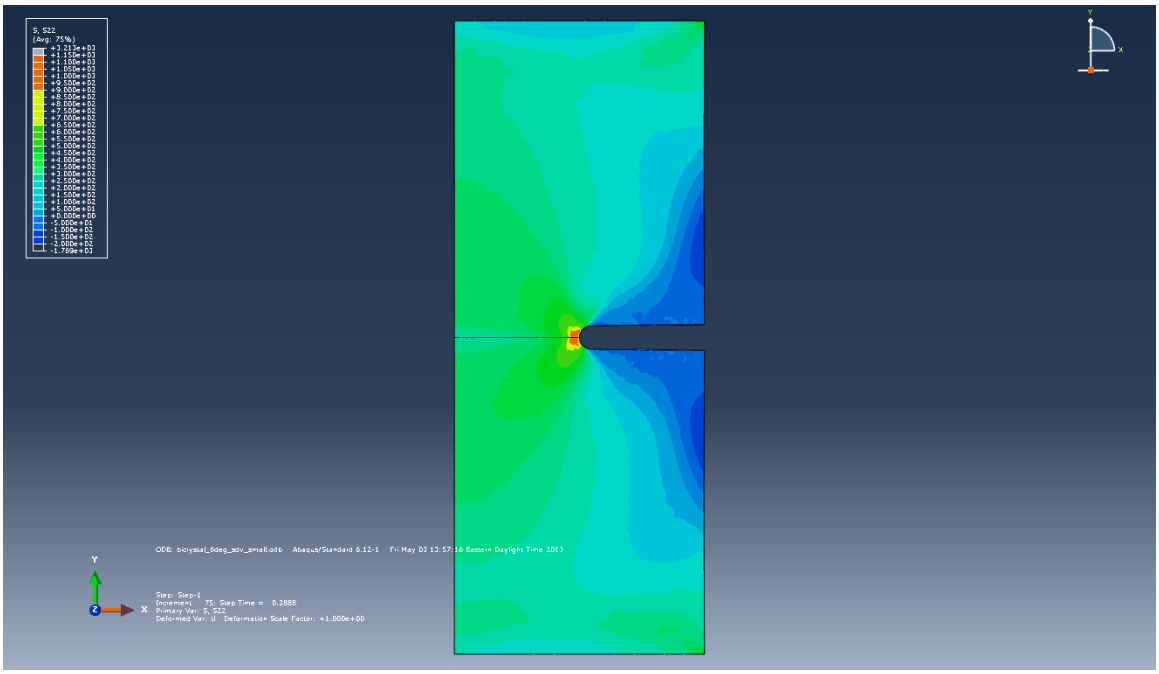

Fig. 71. Contour map of uniaxial stress for 6˚ bicrystal specimen. Note the very slight asymmetry in stress distribution across the boundary due to crystallographic misorientation.

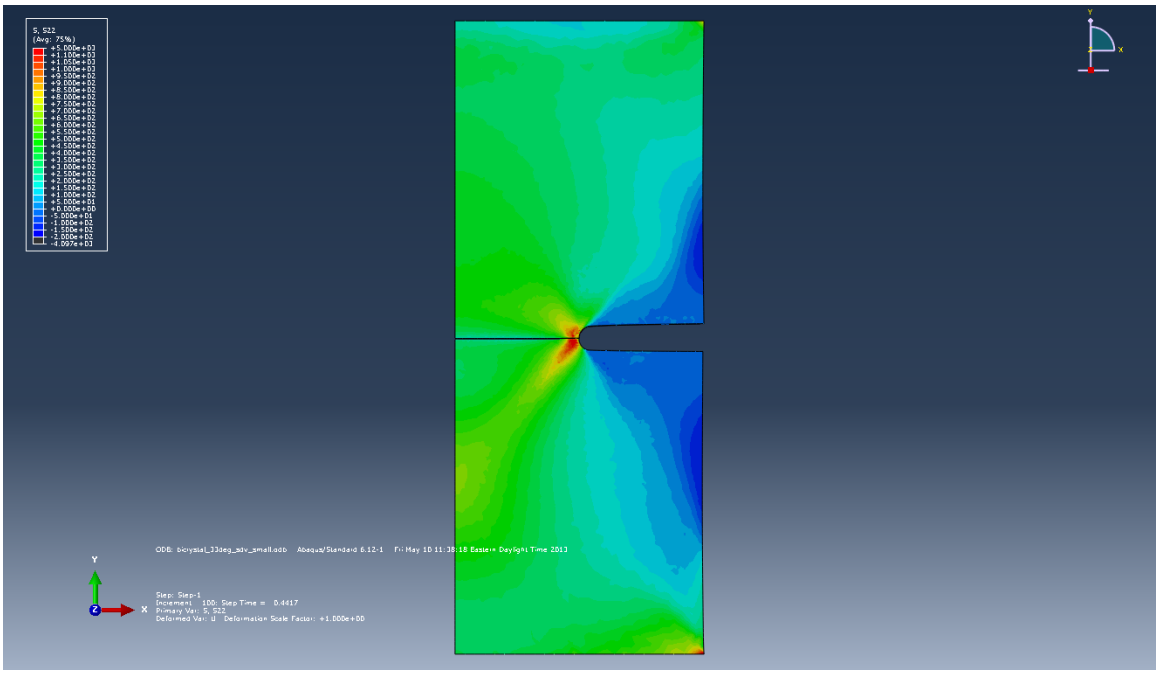

Fig. 72. Contour map of uniaxial stress for 33˚ bicrystal specimen. Note the much more pronounced asymmetry in stress distribution across the boundary due to larger misorientation angle than in the 6˚ case.

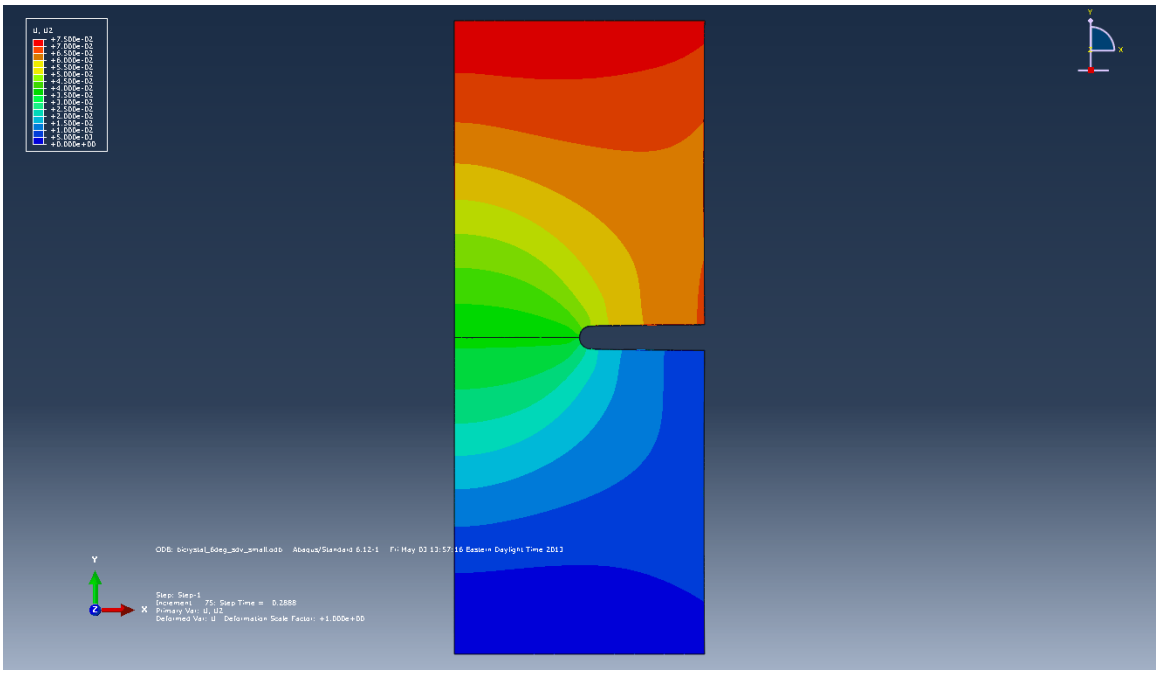

Fig. 73. Uniaxial displacement contour map for 6˚ bicrystal showing zero displacement at bottom surface (fixed).

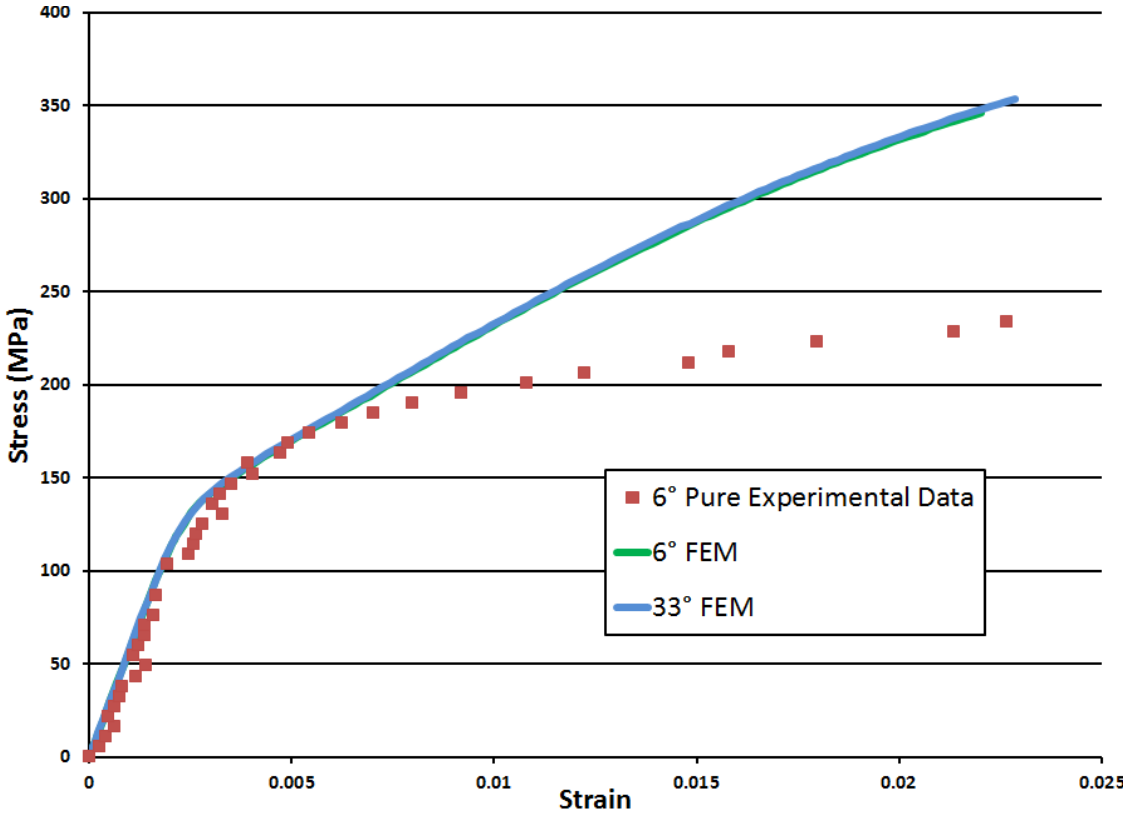

Fig. 74. Stress-strain curves generated from FEM modeling of DENT bicrystals. Note that the curves for both misorientation angles are identical and perfectly overlap. Also shown is the experimental data from a 6˚ pure specimen.

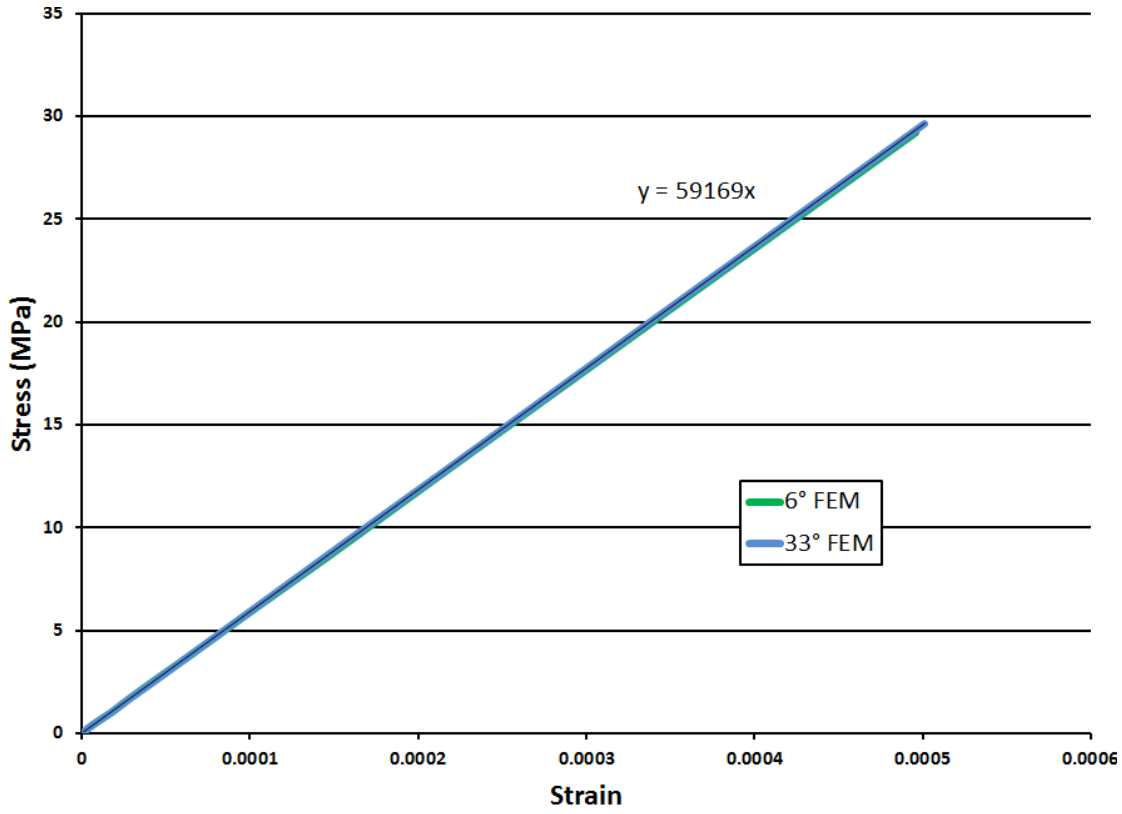

Fig. 75. Elastic portion of FEM curves shown in Fig. 74. Note that both curves are identical and have a slope of ~59 GPa.

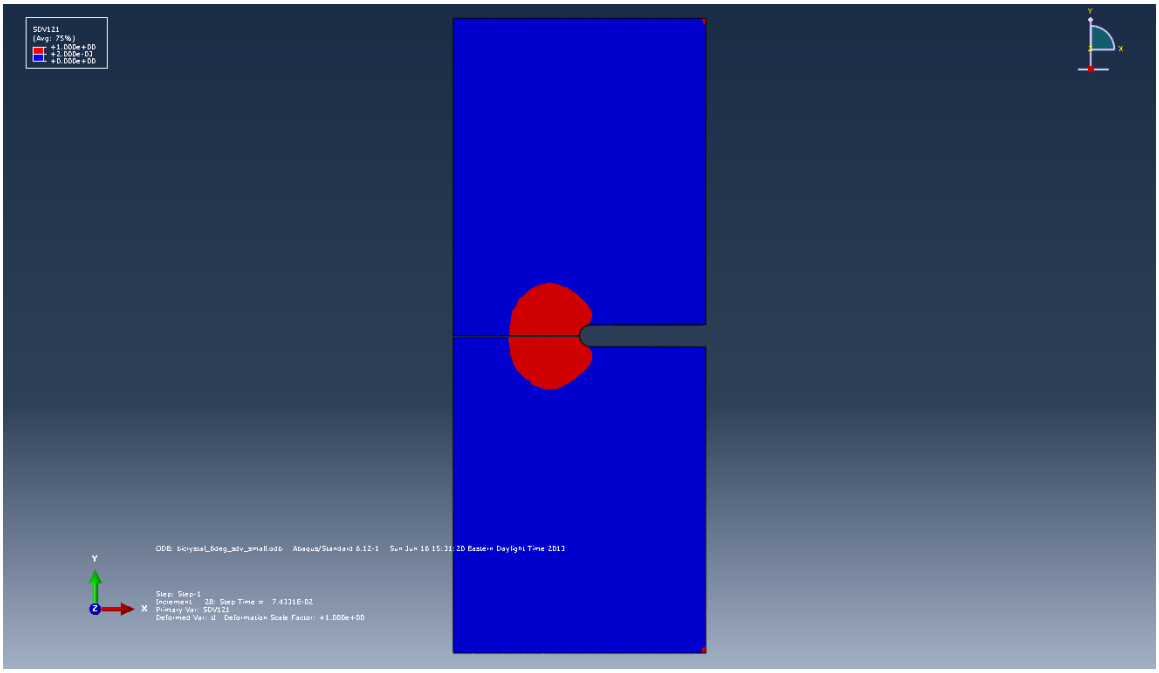

Fig. 76. Plastic zone (shown in red) for 6˚ FEM model prior to elastic limit of stress-strain curve. Image shows that the plastic zone is very symmetric with respect to the boundary, as is expected for a low angle boundary.

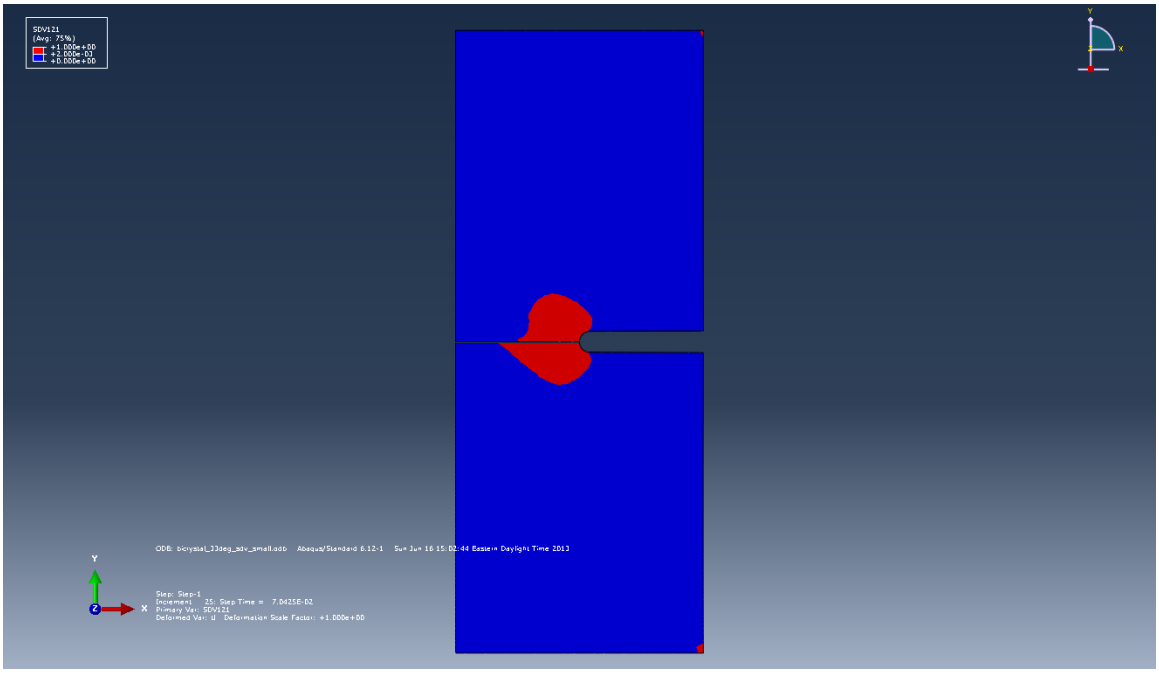

Fig. 77. Plastic zone (shown in red) for 33˚ FEM model prior to elastic limit of stress-strain curve. Image shows that the plastic zone is asymmetric with respect to the boundary, as is expected for a high angle boundary.

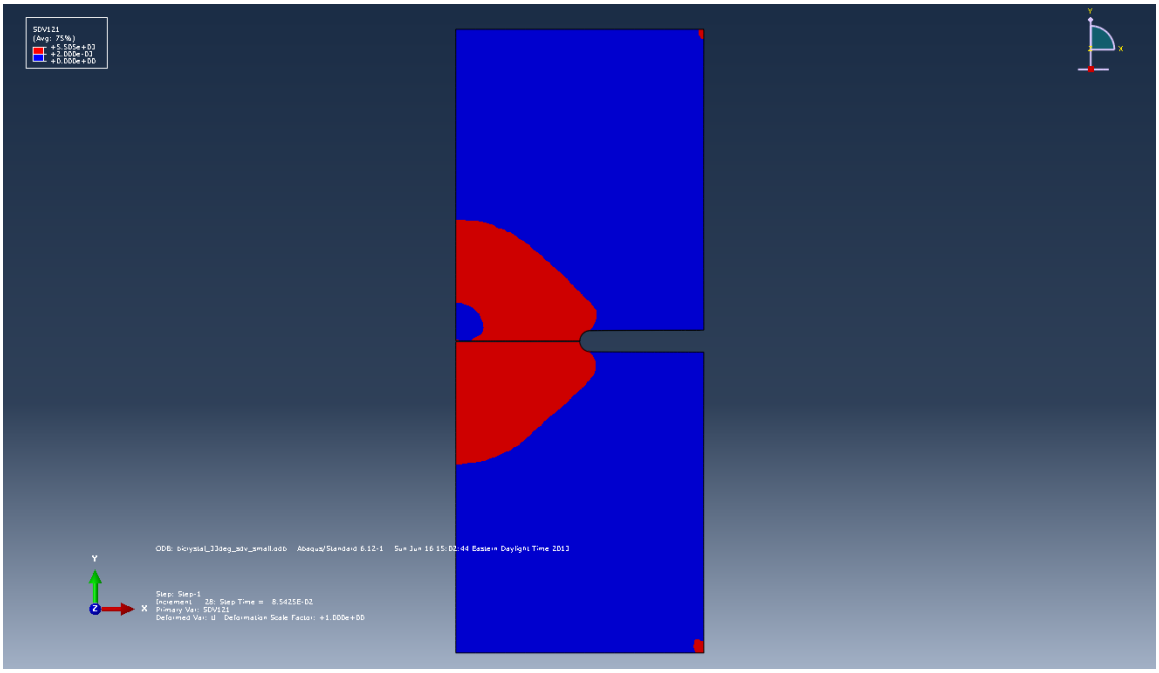

Fig. 78. Plastic zone in 33˚ FEM model at elastic limit of stress-strain curve. This image represents the first simulation step where the plastic zone encompassed the entire specimen width.

VITA

Mark McLean was born on April 7, 1985, to Joe and Wanda McLean in Plainfield, NJ. He later moved to Kingwood, TX where he graduated from Kingwood High School in 2003. He then enrolled in Lehigh University in the fall of 2003 where he majored in Materials Science & Engineering (MS&E). In May 2007, he earned a B.S. in MS&E, graduating with highest honors. During his undergrad years, he also earned the MS&E department's Bradley Stoughton Award and Ken Tarby Prize, both of which are awards for outstanding academic performance. He then began graduate work at Lehigh University in the fall of 2007, also in MS&E. In January 2010, he received his M.S. for his work on viscoelasticity in thin metal films. Mark then began working toward his Ph.D., which he will be receiving in September 2013. After graduation, he will begin a post-doctoral appointment at NIST in Gaithersburg, MD.